



Intense source of positron using channeling effect in crystals

Chenghai Xu

► To cite this version:

Chenghai Xu. Intense source of positron using channeling effect in crystals. Accelerator Physics [physics.acc-ph]. Université Paris Sud - Paris XI, 2012. English. NNT: . tel-00710353

HAL Id: tel-00710353

<https://theses.hal.science/tel-00710353>

Submitted on 20 Jun 2012

HAL is a multi-disciplinary open access archive for the deposit and dissemination of scientific research documents, whether they are published or not. The documents may come from teaching and research institutions in France or abroad, or from public or private research centers.

L'archive ouverte pluridisciplinaire **HAL**, est destinée au dépôt et à la diffusion de documents scientifiques de niveau recherche, publiés ou non, émanant des établissements d'enseignement et de recherche français ou étrangers, des laboratoires publics ou privés.

UNIVERSITE PARIS-SUD GRADUATE UNIVERSITY OF CAS

ÉCOLE DOCTORALE : Noyaux, Particules, Astrophysique, Cosmologie
Laboratoire de l'Accelérateur Lineaire et IHEP-Beijing

DISCIPLINE Physique

THÈSE DE DOCTORAT

soutenue 17/05/2012 a Beijing

par

Chenghai XU

Intense Source of Positron Using Channeling Effect in Crystals

Directeur de thèse:	Fabian ZOMER	Professeur à l'Université Paris-Sud
Co-directeur de thèse:	Guoxi PEI	Professeur à l'IHEP-Pekin
Composition du jury:		
Président du jury:	Jie GAO	Professeur à l'IHEP-Pekin
Rapporteurs:	Alessandro VARIOLA	Directeur du departement Accelérateur au LAL-Orsay
	Jie GAO	Professeur à l'IHEP-Pekin
Examineurs:	Robert CHEHAB	IPN-Lyon
	Chuangxiang TANG	Professeur à l'Universit Tsinghua
	Kexin LIU	Professeur à l'Universit Peking
Membres invités:	Peter SIEVERS	CERN
	Jingyu TANG	Professeur à l'IHEP-Pekin

Contents

Contents	3
1 Introduction	9
2 Physics	13
2.1 Electromagnetic interaction	13
2.2 Photon generation	15
2.2.1 Bremsstrahlung	15
2.2.2 Synchrotron radiation	20
2.2.3 Compton scattering	23
2.2.4 Channeling radiation	26
2.3 Schemes for polarized photons	28
2.3.1 Helical undulator scheme	28
2.3.2 Compton back-scattering scheme	29
2.3.3 Polarized bremsstrahlung scheme	30
2.4 Pair production	33
2.4.1 Pair production in amorphous medium	33
2.4.2 Pair production in crystals at very high energy	37
2.5 Ionization	38
2.6 Coulomb scattering on crystal nuclei	40
3 Simulation	41
3.1 Benchmark of Geant4 simulation	41
3.2 The target	49
3.2.1 The crystal target	49
3.2.2 The hybrid target	49
3.2.3 The choice of the amorphous converter	52
3.3 The capture	55
3.3.1 The AMD	55

3.3.2	The quarter-wave transformer (QWT)	60
3.3.3	The Lithium lens	65
4	Heating and Cooling	71
4.1	General acknowledgement	71
4.2	Total energy deposition	73
4.3	PEDD	76
5	An Application On ILC	85
5.1	Hybrid Source	85
5.2	Crystal Target	86
5.3	Pair Converter	89
5.4	Capture Device	93
6	Control of Emittance	95
6.1	Accelerator theory	95
6.1.1	Particle dynamics in electromagnetic fields	95
6.1.2	RF cavity	99
6.1.3	Phase stability	101
6.1.4	Emittance	102
6.2	Accelerator system	103
6.3	Configuration of Parmela	108
6.4	Simulation results	111
6.5	Matching system	119
7	Conclusion	123
A	Simulation code	125
	Acknowledgement	131
	Bibliography	135

Resume

Le travail développé dans cette thèse concerne un type particulier de sources de positrons utilisant le rayonnement de canalisation dans un cristal ainsi que d'autres effets cristallins observés le long des axes du cristal ; ces effets produisent un grand nombre de photons qui, à leur tour, génèrent un grand nombre de paires e^+e^- dans une cible amorphe. Les photons et les paires sont créés dans deux cibles différentes séparées par une certaine distance permettant l'installation d'un aimant pour dévier les particules chargées avant la cible amorphe. Une telle source est appelée source hybride de positrons ; elle a été choisie par le CERN pour le projet CLIC. Ce type de sources présente de réels avantages par rapport aux cibles conventionnelles qui ont une grande emittance ainsi qu'un niveau important de dépôt d'énergie dans la cible.

Après un rappel des phénomènes physiques qui concernent notre étude, des simulations détaillées utilisant d'une part le programme de V. Strakhovenko pour les effets cristallins et d'autre part le code GEANT4 pour la génération des positrons conduisent à une description complète pour les photons et les positrons avec, notamment, les espaces de phase longitudinal et transverse, le spectre en énergie, la distribution temporelle,.. Nous avons particulièrement insisté sur deux points : d'abord sur les dispositifs de capture des positrons après la cible qui sont essentiels pour avoir de bons rendements de positrons acceptés et ensuite sur la densité de l'énergie déposée dans la cible qui représente un paramètre important pour la survie des cibles. En ce qui concerne le premier point, trois dispositifs de capture ont été étudiés : le système adiabatique (AMD), le système quart d'onde (QWT) et la lentille de lithium. Pour le deuxième point qui concerne l'énergie déposée et l'échauffement de la cible, on a cherché à optimiser la densité d'énergie déposée en diminuant son maximum (PEDD) ; l'énergie moyenne déposée a aussi été optimisée en utilisant une solution spéciale pour le convertisseur : un convertisseur granulaire forme de petites sphères, comme cela avait été considéré précédemment pour les usines à neutrinos. Des résultats très prometteurs nous ont conduits à

envisager la source hybride de positrons avec un convertisseur granulaire comme une solution au difficile problème d'ILC. Cette solution est étudiée moyennant une transformation des impulsions du faisceau avant la cible, comme cela avait et envisage par l'équipe du KEK. Le transport du faisceau de positrons au-delà du solénoïde a été étudié avec la première partie de l'optique quadrupolaire.

Keywords: positron source, channeling effect, crystal, ILC, granular target

Abstract

The research work carried out for this PhD is concerning a special kind of positron source using channeling radiation and other crystal effects in an axially oriented crystal to generate a high number of photons which create, subsequently, a large number of pairs in an amorphous target. Photon generation and pair creation are developing in two targets separated by some distance allowing a sweeping magnet to get off the charged particles away from the amorphous converter. Such a scheme is called a hybrid positron source and has been adopted for the CLIC baseline. This kind of sources present big advantages with respect to the conventional sources where large emittance and important heat deposition are met.

After some recall on the physical phenomena of interest for our study, detailed simulations are worked out using a special program dealing with crystal effects from Prof. Strakhovenko and the GEANT4 code; these tools led to a complete description of the positron source concerning the photons from one side and the positrons, from the other side, for which the main characteristics have been determined: transverse and longitudinal phase space, energy spectrum, time distribution,...Emphasis has been put on two points: first the matching devices capturing the positrons after the target which are essential for good accepted yields and the energy deposition density which is an important question for the reliability of the targets. Concerning the former point, three matching devices have been studied and their features compared: the Adiabatic Matching Device (AMD) largely used or considered for the positron sources, the Quarter Wave Transformer (QWT) and also the Lithium lens. For the latter point, related to the energy deposition and heating of the targets, we have tried to optimize the energy deposition density lowering its maximum value (PEDD); the average heat deposition has also been optimized using special converter material in granular shape, as considered for the neutrino factories. Very promising results allowed us to consider the hybrid positron source as an alternative to the difficult case of ILC; a special scheme for the transformation of the ILC beam pulses has been used, after KEK proposition.

The positron beam transport has also been studied in the first part of the positron pre-accelerator including the solenoid and the first part of the quadrupole channel.

Keywords: positron source, channeling effect, crystal, ILC, granular target

Chapter 1

Introduction

In e^+e^- Colliders, positron source is a very important part. Usually electron beams are used to impinge on metals with high atomic number. The electron emits hard photons in the electric field of nuclei, then the photons undergo materialization which produces e^+e^- pairs. The positron beam coming out of the target has a small size, a large transverse emittance which is due to the multiple scattering, and a wide energy spectrum which is due to the wide energy spectrum of hard photons and the energy dispersion of positrons, so a matching system is needed to capture the e^+ .

In order to get high intense positron source, incident energy, intensity and target thickness need to be increased. Although this will result in a very serious problem, namely there are large amount of energy deposition in the target due to the ionization process, consequently the energy deposition may meltdown the target or provoke breakdown due to instantaneous heating as seen in the SLC target[1].

One alternative solution is based on the channeling effect of GeV electron beams impinging on axially oriented crystals[2, 3]. In channeling conditions: the incident direction is aligned with the crystal rows, the electrons emit a large number of photons which are more numerous than bremsstrahlung in an amorphous target of the same thickness. The photons then create a large amount of e^+e^- pairs. After a proof of principle experiment worked out at Orsay, this method was carried out twenty years ago by French teams of LAL-Orsay and IPN-Lyon, collaborating with Russian teams from the Budker Institute of Novosibirsk[4, 5]. The electron beam undergoing channeling effect in crystal target has been used in the WA 103 experiment at CERN and then at KEK with different experimental conditions[6, 7, 8]. Enhancement of positron yield was observed in both experiments. In the

KEKB linac the conventional target has been replaced by a crystal one[9].

In channeling conditions, the radiation length in a crystal is shorter than that in an amorphous metal, so for the same positron yield, the crystal has a shorter thickness than using the amorphous medium. The shortening of crystal thickness will lead to a decreasing of energy deposited in the medium which has been shown in simulations[10]. To strongly reduce the energy deposited in the target, a hybrid system was proposed in which we separate the photon radiator and e-e+ converter[11]. A 1 or 2mm thick tungsten crystal target can be considered as photon radiator, and a thick tungsten amorphous target could be selected as e-e+ converter. Photons coming from the crystal target will be sent to the amorphous target, and charged particles from the crystal target will be swept off. Simulations have been done and very good results have been got. The energy deposited in the target is strongly reduced. A single hybrid system is workable instead of using multi-target systems. This single hybrid system has been selected as the unpolarized scheme in baseline of the CLIC collider.

But for the ILC, the incident beam intensity is very high, and the amorphous target may still meltdown even using a hybrid system. Another technology should be taken to resolve this problem. Here a solution is proposed, in which a granular target is used to replace the compact amorphous target. The granular target, composed of a lot of small spheres, is held by a container. The cooling gas flows through the space between spheres and take off the energy deposited in the spheres. This is based on the energy dissipation rate which is in proportion to the ratio of Surface/Volume. For the small sphere the ratio is strongly larger than the compact target, so the energy dissipation rate of the small sphere is more efficient than the compact target and could be cooled very quickly. Some simulations and calculations have been done and promising results have been got. Such solution has been considered by P.Sievers for neutrino factory[12]

This thesis will cover a detailed study on the hybrid system using compact and granular amorphous targets. It mainly concerns the following parts, the theoretical description of physics processes in the crystal target and amorphous target, the simulations done on the targets, the control of transverse and longitudinal emittance, the heating problem and its solution for the amorphous target, the study of the coulomb scattering of the incident electron beams on the crystal nuclei.

Chapter 3 - Simulations on the target: For the simulation on amorphous target, we implement Geant4 code to simulate the propagation of particles in the target with considering a large number of physical processes. Two types of targets have been considered, compact and granular target. Two colliders cases are studied: CLIC and ILC. Lots of data about the positron properties at the exit of the target

are produced, for example, yield, energy spectrum, transverse dimension and momentum spectrum, emittance, etc. Comparisons between the two types of target are shown, the target thickness is optimized. For the simulation on crystal target concerns the channeling effect and coherent bremsstrahlung, two programs are used. The first is VMS[13] and the second is G4Fot[14]. A full comparison between results from G4Fot and VMS is made for different cases. Three types of matching system are introduced: Adiabatic Matching System, Quarter Wave Transformer and Lithium Lens. The calculation is made by introducing the magnetic field in Geant4. Full comparisons about the yield, energy spectrum, transverse dimension and momentum, transverse emittance, bunch length and acceptance are shown. The size of matching system, accelerator structure and their electromagnetic parameters are optimized to lower the emittance, energy dispersion and to enlarge the yield.

Chapter 4 - Heating and cooling of the target: Energy deposition in granular and compact target are studied. The total energy deposited in the amorphous target and energy distribution are retrieved from our simulations. PEDD (Peak Energy Deposited Density) has been calculated and compared with the maximum tolerated value from the analysis of the SLC target. The incident beam size, distance between crystal and amorphous target are optimized to reduce the PEDD. A comparison about energy dissipation between granular and compact target is done. The energy deposited in the container of granular target is also considered. The shock wave effects due to the thermal gradient are studied and the size of the spheres in the granular target is optimized. Finally a scheme of hybrid system using amorphous granular target for ILC is proposed.

Chapter 5 - An application on ILC: A hybrid target scheme for ILC unpolarized conventional positron source will be presented. This hybrid target is composed of a crystal target, an amorphous target and a $2m$ long bending magnet between the two targets which is used to sweep off the charged particles. The crystal target thickness is $1mm$ and it is optimized to $10.2mm$ for the amorphous target. Positron features will be discussed at the exit of the granular target. A cooling scheme is proposed for the granular target and crystal target. A container holds the crystal target and helium is used for cooling. For amorphous target, a holder is used to contain the amorphous spheres, where Be is chosen for upstream and downstream windows and Ti for upper and lower windows, helium is used to cool the spheres. The total energy deposition and PEDD in the crystal target, amorphous target and its windows are calculated and the cooling efficiency will be discussed. A $50cm$ long AMD and a $1m$ long accelerator are implemented after the granular target. The yield, emittance and energy spectrum are calculated and will be discussed.

Chapter 6 - Control of emittance: Geant4 has some ability to simulate the

propagation of particles in the electromagnetic field, but it is less appropriate to work in a long length structure with electromagnetic field, so other program such as Parmela is needed to simulate the transport of positron beam in the matching system and accelerator. In this chapter an accelerator system will be shown which can accelerate positrons to 300MeV . To capture more positrons the 1.3GHz L-Band standing wave π mode cavity is used, where there are 8 cells per cavity. The averaged electric gradient is $15\text{MV}/\text{m}$. The phase of accelerator is optimized. In order to control the positron beam, the accelerator is immersed in a solenoid, whose magnetic field is 0.5Tesla . The yield, emittance and energy spectrum along the accelerator system are presented and discussed.

Chapter 2

Physics

2.1 Electromagnetic interaction

High energy particles impinging on a target with a high atomic number can develop a cascade shower. If an electron goes through the target, it will emit photon and lose energy by collision. The incident trajectory will be deflected by scattering. The secondary photons will participate in Compton scattering or pair production and lose energy simultaneously. The charged secondary particles will repeat the same process, etc... The process continues until all the energy is dissipated in the target or the secondaries coming out of the target. The interactions in the cascade are complex so we will only introduce the main processes concerning the positron source.

According to the quantum electro-dynamics, all the electromagnetic interactions should be described as processes of photon emission and absorption. However, it is hard to calculate in terms of more general electromagnetic field than the relatively simple Coulomb forces acting between their charges. Usually one proceeds by first computing the mechanical behavior of the particles concerned without reference to emission or absorption of photons, and later introducing radiation phenomena as a perturbation.

When charged particles traverse a medium, the interaction with matter can be classified as three types according to the impact parameter to the nuclei: interaction with atom as a whole, interaction with an atomic electron and interaction with the nucleus[15].

1. If the impact parameter is larger compared with the radius of the atoms, the

results is an excitation or an ionization.

2. If the impact parameter is of the order of the atomic dimensions, the interaction will involve the incident particle and one of the atomic e^- . This will result in an ejection of e^- with considerable energy. We can neglect the radiation but must consider the magnetic moments or spins of the interacting particles. Usually this phenomena is called "collision process."
3. If the impact parameter is smaller than the atomic radius. The passing particles will be deflected and emit photons with a continuous frequency. This is called Radiation or Bremsstrahlung.

Correspondingly, there are three types of interaction between photons and matter.

1. A photon interacting with an atom, which is the photo-electric effect.
2. A photon interacting with an atomic electron, which is the Compton effect.
3. A high energy photon interacting with the nucleus, which is the pair production process.

Both the Compton effect and the pair production are quantum phenomena without classical counterpart, and the quantum electrodynamics mechanic is needed to explain these phenomena. According to the energy conservation the photon's energy must be larger than the sum of its secondary particle mass when it takes part in pair production.

2.2 Photon generation

2.2.1 Bremsstrahlung

Incident electrons with high energy mainly lose energy by bremsstrahlung because of its small mass. In this process the incident electrons are accelerated and then the photons are emitted in the electric field of nuclei. The emitted photons have a continuous spectrum.

To describe the bremsstrahlung, we shall use the method of virtual photons developed, independently, by E.Fermi (1924) and C.Weiszacker, E.Williams (1934)[16]. In each collision, we define an incident particle and a target-system. Here, we consider a nucleus accompanied by its cloud of virtual photons, corresponding to its Coulomb field, incident on the electron-fixed target. We expect, then, Compton scattering between the photons cloud and the electron. The sketch of the interaction is presented on Fig. 2.1. This description follows closely that of E.Fermi.

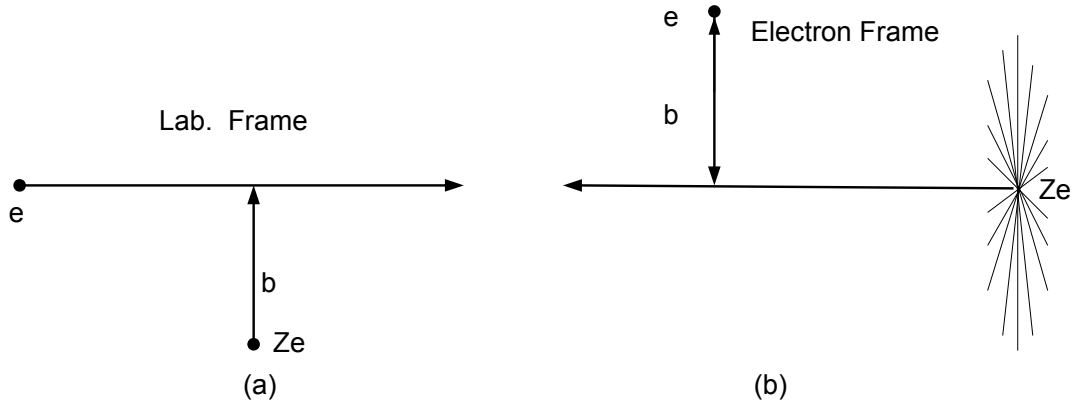


Figure 2.1: Bremsstrahlung: sketch of the interaction

Consider an electron with velocity of $v \sim c$ passing a nucleus. From the rest frame of incident electron, the nucleus moves towards the electron with velocity of v . The peak electric field E of nucleus is contracted in the direction of motion, the associated magnetic field B is perpendicular to E and has the same magnitude as E because of Lorentz transform. It looks like a plane electromagnetic wave which represent the virtual photons and moving toward the electron. The virtual photons suffer Compton scattering by the incident e-. The scattered quanta appears as bremsstrahlung emitted by the incident electron when viewed from the laboratory frame.

Assuming that the distance between the primary particle and the nuclei is larger than the nuclear radius, the nucleus can be treated as a point charge. Symbol with asterisk indicates it is a quantity in electron frame.

The electric field of the nuclei in the laboratory frame is

$$E_{\perp} = \frac{Ze}{b^2} \quad (2.1)$$

where b is the impact parameter, Z is the atomic number and symbol \perp means the quantity is perpendicular to v . Transfer to electron frame:

$$E_{\perp}^* = E_{\perp}\gamma, \quad H_{\varphi}^* = E_{\perp}\beta\gamma \quad (2.2)$$

H_{φ}^* is the magnetic field in the direction perpendicular to v and E^* . In the relativistic condition, $\beta \sim 1$, so $E_{\perp}^* = H_{\varphi}^*$, we have a plane wave. The electromagnetic field in electron frame is concentrated in the time interval: $t_{eff} = b/\gamma c$. The dependence of E and H on time can be approximated by Gaussian distribution with a width $b/\gamma c$.

$$E^* = H^* = \frac{\gamma Ze}{b^2} e^{-c^2\gamma^2 t^2/2b^2} \quad (2.3)$$

The Fourier transform is also a Gaussian with a width $\gamma c/b$, we can also approximate it by a rectangle with a width $\gamma c/b$.

The electromagnetic energy per unit volume is given by

$$\frac{E^{*2} + H^{*2}}{8\pi} \simeq \frac{Z^2 e^2 \gamma^2}{b^4} \quad (2.4)$$

The photon cloud pancake has a time width of $b/\gamma c$ which corresponds to a length of b/γ , so the energy per unit area is

$$\frac{Z^2 e^2 \gamma^2}{b^4} \frac{b}{\gamma} \simeq \frac{Z^2 e^2 \gamma}{b^3} \quad (2.5)$$

As said before, the Fourier transform is a Gaussian with a width $\gamma c/b$, can be approximated by a rectangle of width $\gamma c/b$ and has an upper limit frequency $\nu_{max}^* = \gamma c/b$. Under such an assumption the energy per unit area given by Eq. (2.5) is distributed over the rectangle frequency spectrum. So the total number of photons corresponding to the energy per unit area at a distance b can be given by

$$\frac{Z^2 e^2 \gamma}{b^3} \frac{1}{h\nu_{max}^*} = \frac{Z^2 e^2 \gamma}{b^3} \frac{b}{h\gamma c} \quad (2.6)$$

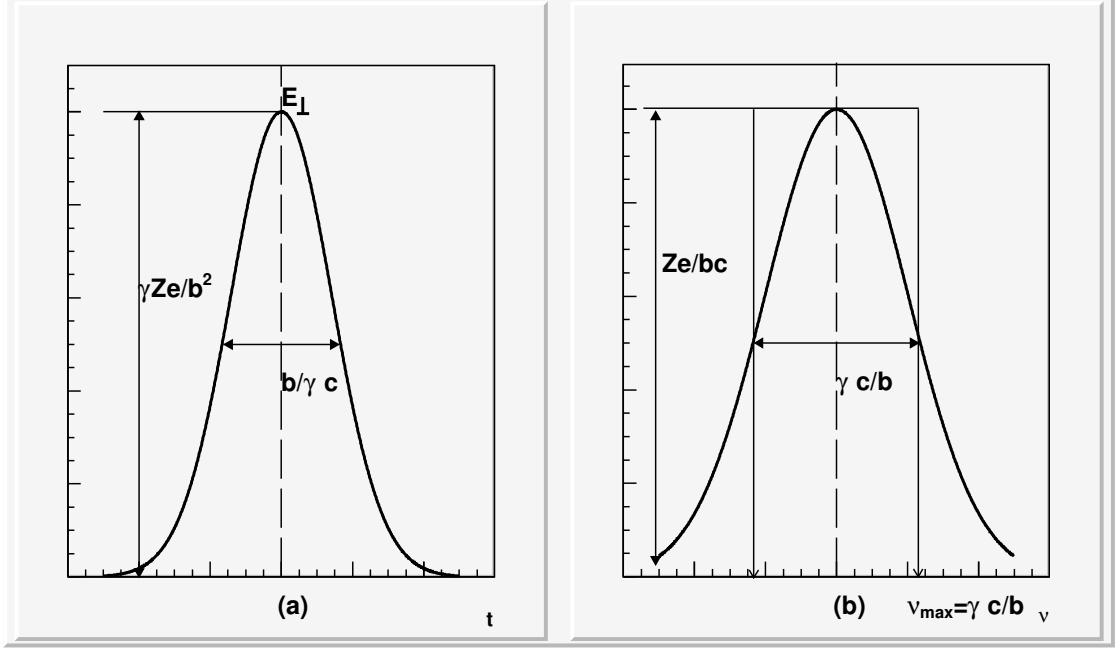


Figure 2.2: Electromagnetic pulse in the electron frame and its Fourier transform: (a) pulse, (b) spectrum

So the number of photons with a frequency ν^* in the interval $\Delta\nu^*$ and at a distance b is proportional to $\Delta\nu^*/\nu^*$

$$\frac{Z^2 e^2 \gamma}{b^3} \frac{b}{\gamma c} \frac{\Delta\nu^*}{h\nu^*} \quad (2.7)$$

This equation is valid only when $\Delta\nu^* < \gamma c/b$. The mean number of scattered photons of frequency ν at a distance b is

$$\sigma_T \times (\text{photon density per area with frequency } \nu^*) = \frac{Z^2 e^2}{b^2 h c} \frac{\Delta\nu^*}{\nu^*} \sigma_T \quad (2.8)$$

where σ_T is the cross section of Compton scattering.

The total cross section per nucleus be $\sum(\nu^*)\Delta\nu^*$ which equal to the integral of Eq. (2.8) over the area of the photon cloud.

$$\sum(\nu^*)\Delta\nu^* = \frac{\Delta\nu^*}{\nu^*} \sigma_T \frac{Z^2 e^2}{h c} \int \frac{2\pi b db}{b^2} \quad (2.9)$$

$$= \sigma_T \frac{Z^2 e^2}{h c} \frac{\Delta\nu^*}{\nu^*} \ln \frac{b_{max}}{b_{min}} \quad (2.10)$$

The integration range $b_{max} = a_0/Z^{1/3}$ (a_0 is the Bohr radius), $b_{min} = \lambda_e$ (Compton electron wavelength) and $\sigma_T = 8\pi/3r_e^2$. Finally the following result can be given

when return to laboratory frame and take into account the neglected numeric factors

$$\sum(\nu)\Delta\nu = \frac{4}{137}Z^2\frac{\Delta\nu}{\nu}r_e^2\ln\frac{183}{Z^{1/3}} \quad (2.11)$$

where r_e is the electron radius.

The total energy lost to photons of frequency ν per path length dx is

$$(\text{photon energy}) \times (\text{nuclei density}) \times (\sum(\nu)\Delta\nu) \times dx \quad (2.12)$$

The integration of the frequency ν gives the total average energy loss per path length dx by incident electron

$$-\left(\frac{dE}{dx}\right)_{rad} = E4Z^2\frac{N}{137}r_e^2\ln\frac{183}{Z^{1/3}} \quad (2.13)$$

where $E = h\nu_{max}$, which is electron energy, N is nuclei density. From Eq. (2.13) it can be seen the radiation loss is proportional to the incident energy and the square of atomic number. So in order to get more photons it needs to increase the incident energy and use high atomic number material.

Define radiation length X_0

$$\frac{1}{X_0} = 4\frac{N}{137}Z^2r_e^2\ln(183Z^{-1/3}) \quad (2.14)$$

So the radiation loss evolution is

$$E = E_0e^{-t} \quad (2.15)$$

where $t = x/X_0$. The Eq. (2.15) means the radiation loss is the same for all material if in terms of radiation length.

However, the above calculation does not consider the effect of atomic electrons on the nuclei, screen effect. Screen effect is an important factor in bremsstrahlung where the nuclei electric field is screened by atomic electrons, which can reduce the interaction force and is not negligible in high energy region. The screen effect can be described as below[15, 17]:

$$\xi = 100\frac{m_e c^2}{U}\frac{\mu}{1-\mu}Z^{-1/3} \quad (2.16)$$

where $U = E + m_e c^2$ is the total energy of incident electron, $\mu = E'/U$, E' is energy of emitted photon. The smaller ξ , the greater screening effect. For high incident energy where $\xi \sim 0$ we can treat it as complete screening.

In the complete screening case, the differential radiation probability per path length dx is given by[15]
for $m_e c^2 \ll U \ll 137 m_e c^2 Z^{-1/3}$:

$$-\left(\frac{dE}{dx}\right)_{rad} = 4Z^2 \frac{N}{137A} r_e^2 E \ln \left[\frac{2E}{m_e c^2} - \frac{1}{3} \right] \quad (2.17)$$

for $U \gg 137 m_e c^2 Z^{-1/3}$:

$$-\left(\frac{dE}{dx}\right)_{rad} = 4Z^2 \frac{N}{137A} r_e^2 E \left[\ln(183Z^{-1/3}) + \frac{1}{18} \right] \quad (2.18)$$

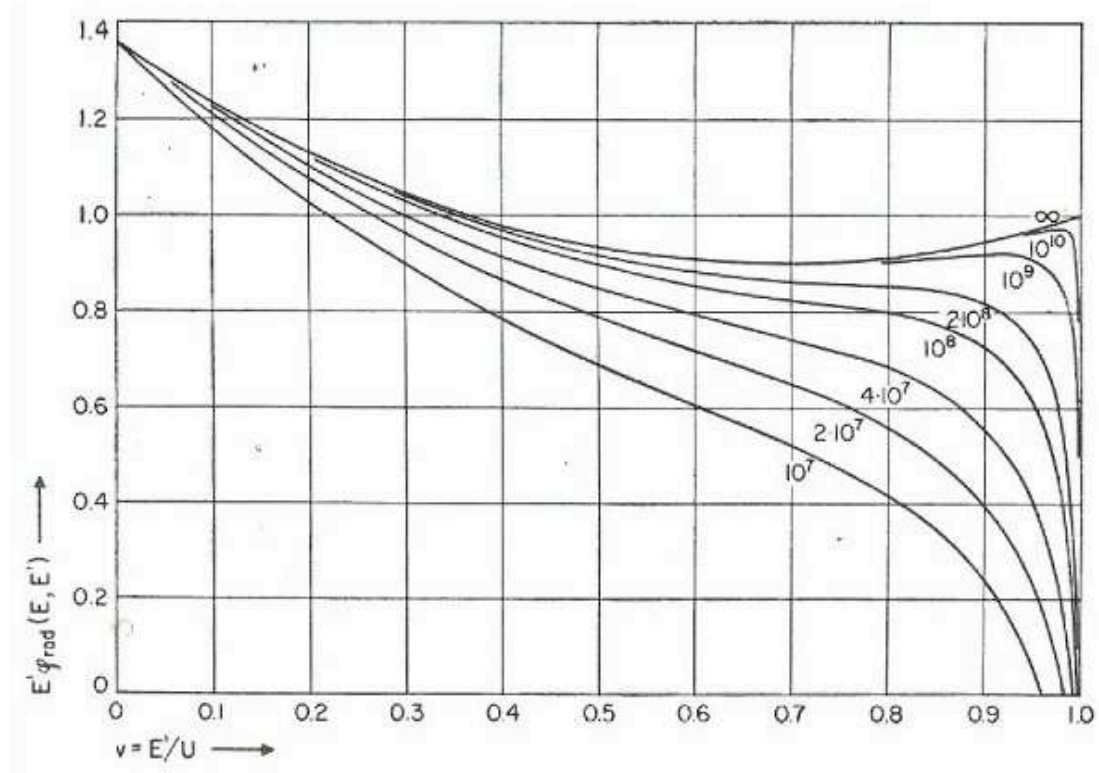


Figure 2.3: Differential radiation probability per radiation length of lead for electrons of various energy[15].

Comparing Eq. (2.18) and Eq. (2.13), there is a difference of one factor. Introduce the average fractional energy loss per radiation length.

$$-\frac{1}{U} \frac{dE}{dt} = -\left(\frac{dE}{dx}\right)_{rad} \frac{X_0}{U} \quad (2.19)$$

where $t = x/X_0$.

In complete screening case, the the average fractional energy loss has the following value:

$$-\frac{1}{U} \frac{dE}{dt} = 1 + b \quad (2.20)$$

where $b = 1/[18 \ln(183Z^{-1/3})]$. b slightly depends on Z , atomic number. From Fig. 2.4 it shows that the fractional energy loss by collision decreases as the incident energy increases, but increases by radiation loss as the incident energy increases. For Lead with an incident energy of about $10MeV$ the fractional energy loss by the collision is equal to the radiation. This defines a quantity, critical energy.

2.2.2 Synchrotron radiation

High intensity positron sources with polarization are needed in future colliders. One solution is to use circularly polarized photons produced in a helical undulator by high energy non-polarized electrons. This system can produce large amount of photons and has a lower thermal deposition in the e-e+ converter because the electrons do not impinge on the converter.

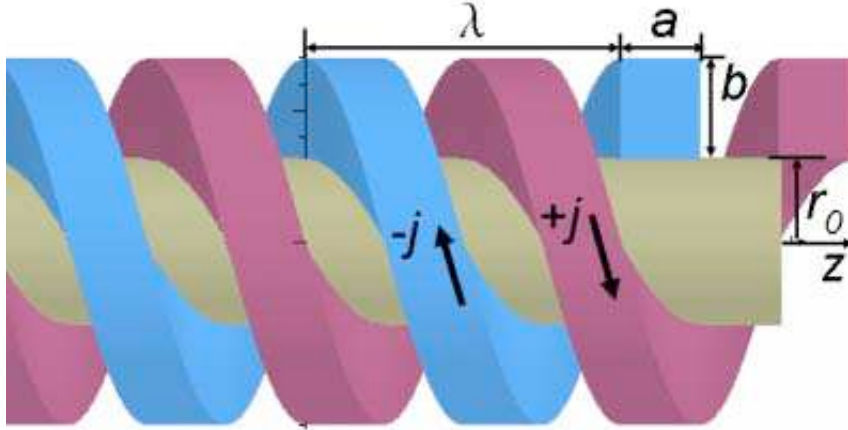


Figure 2.5: A model helical undulator, where λ is the period length, r_0 the inner radius of the coil, a and b the coil dimension, and j the coil current density. The empty "air space" between the coils may be replaced with high-permeability steel poles.[18]

Undulator is an insertion device which consists of a periodic structure of dipole magnets. The static magnetic field is alternating along the length of the undulator with a period λ_w . Helical undulators are made of a double-helix-wound bifilar

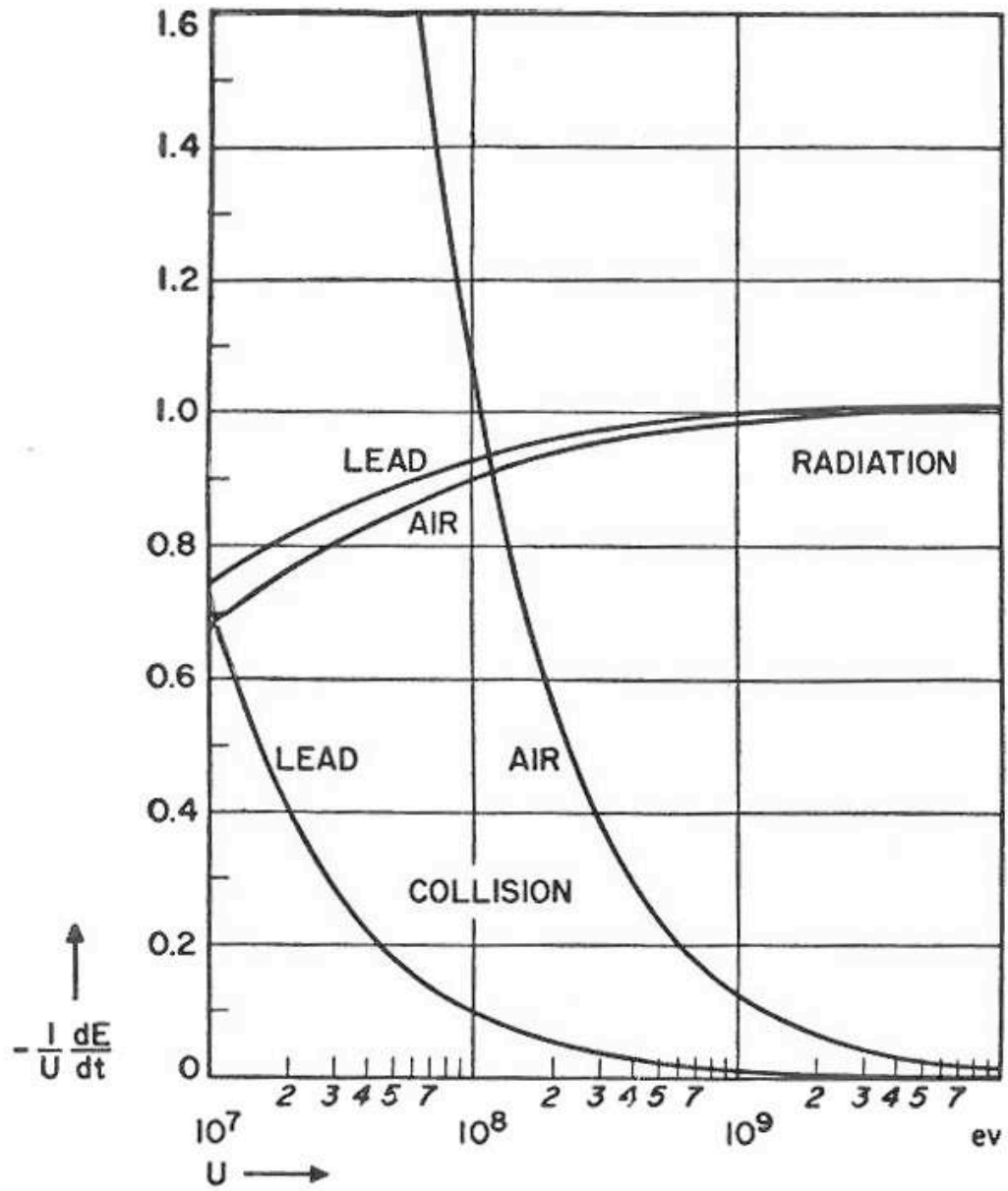


Figure 2.4: Fractional energy loss by collision and radiation for electrons in air and lead[15].

currents with opposite direction around a tube[19]. The currents produce transverse periodic helical magnetic field of constant magnitude. Electrons traversing the periodic magnet will undergo oscillation and emit photons. The orbit of the electrons in the helical magnetic field B is a helix having the same period λ_w as the field. The radius is:

$$b = \left(\frac{\lambda_w}{2\pi\rho} \right)^2 \rho \left[1 - \left(\frac{\lambda_w}{2\pi\rho} \right)^2 \right]^{-1/2} \quad (2.21)$$

where $\rho = \gamma\beta mc^2/eB$, β and γ are the normalized velocity and energy.

Synchrotron radiation with circular polarization is emitted in a conical angle $\theta \sim 1/\gamma$ around the electron motion direction. Electrons with very high energy and large number of periods in the undulator will produce photons with a narrow spectrum. The wavelength is

$$\lambda = \frac{\lambda_w}{2\gamma^2} (1 + K^2) \quad (2.22)$$

and

$$K = \frac{\lambda_w e B}{2\pi m c} \quad (2.23)$$

For $K \ll 1$, the oscillation amplitude of the motion is small and the interference pattern occurs, which leads to a narrow energy bands. If $K \gg 1$, the oscillation amplitude is larger and the radiation from different period is non-correlated, which leads to a broad energy spectrum. In the second case it is a wiggler.

The energy bandwidth for the photons is $\sim 1/N$ and depends on the angular divergence of the electron beam which must be less than:

$$\theta_{max} = \left[\gamma \sqrt{N} \right]^{-1} \quad (2.24)$$

From Eq. (2.22) we can calculate the peak energy of the photons:

$$E_\gamma = \frac{4\pi\hbar c\gamma^2}{\lambda_w (1 + K^2)} \quad (2.25)$$

and the peak energy is obtained when $K = 1$

$$E_\gamma = \frac{2\pi\hbar c\gamma^2}{\lambda_w} \quad (2.26)$$

The rate of energy loss by radiation is

$$P_\gamma = \frac{2}{3} \frac{r_e c}{(mc^2)^3} E^2 F_\perp^2 \quad (2.27)$$

where $F_\perp = ecB$ and E is the energy of electron. So the total radiated energy of an electron is

$$\Delta W = \frac{8}{3} \pi^2 r_e mc^2 \frac{\gamma^2 K^2 N}{\lambda_w} \quad (2.28)$$

The number of radiated photons is:

$$N_\gamma = \frac{2}{3} \pi \alpha K^2 (1 + K^2) N \quad (2.29)$$

where $\alpha = 1/137$ is the fine structure number. Here we can see the yield of photon depends on K and N . An electron of $100 GeV$ going through a $100m$ long undulator with a period of $1cm$ will produce 250 photons with energy of $5.3 MeV$

2.2.3 Compton scattering

Compton effect process occurs when the photon collides with rest electron and transfers some energy to electron. If the electron motion is in relativistic region, the photon will gain energy and the electron will loose energy. This is called Compton back-scattering or inverse-Compton scattering. A scheme based on this phenomenon was proposed as a solution for ILC polarized positron source[20]. A 1 to 2 GeV electron beam collides with a laser beam in visible or infrared light. The laser is circularly polarized, then the produced photons by Compton scattering are also circularly polarized. Photons have tens of MeV energy. Then photons are sent to thin e-e+ pair converter. Finally lots of longitudinally polarized e-e+ pairs are obtained.

It's convenient to calculate in the electron rest frame. In this frame, the laser photon energy has an increase by γ . According to the conservation of energy and momenta, we have

$$E_e = E_{photon} - E'_{photon} + E_o \quad (2.30)$$

$$P_e = P_{photon} - P'_{photon} \quad (2.31)$$

where E_e and E_o correspond to final and initial energies of electron. E_{photon} and E'_{photon} are the initial and final photon energies. P_e is final electron momentum. P_{photon} and P'_{photon} are initial and final photon momentum.

Add the conservation of relativistic invariant:

$$(E/c)^2 - P^2 = m_0^2 c^2 \quad (2.32)$$

We get the wavelength shift:

$$\Delta\lambda = \lambda_e [1 - \cos\theta] \quad (2.33)$$

where λ_e is the Compton wavelength of electron and θ is the angle of the scattered photon with respect to the initial direction.

Coming back to the laboratory frame, the photon frequency will be significantly increased because of Doppler shift. The angular distribution will be concentrated in a small angle, $\sim 1/\gamma$. The energy of the Compton photon produced in laser and electron interaction is:

$$\omega_2 = \frac{(1 - \beta \cos\theta_1)\omega_1}{1 - \beta \cos\theta + [1 - \cos(\theta - \theta_1)]\omega_1/E} \quad (2.34)$$

where ω_1 and ω_2 are energies for laser and Compton photon. E is electron energy.

For high E taking the first approximation we have $\beta = 1 - 1/2\gamma^2$. For small θ , $\cos\theta = 1 - \theta^2/2$. Considering head-on collision, complete back scattering, where $\theta_1 = \pi$, insert above approximation we have

$$\omega_2 = \frac{\left(2 - \frac{1}{2\gamma^2}\right)\omega_1}{\frac{1}{2\gamma^2} + \frac{\theta^2}{2} + [2 - \frac{\theta^2}{2}]\omega_1/E} \quad (2.35)$$

Neglect small quantities,

$$\omega_2 = \frac{4\gamma^2\omega_1}{1 + \gamma^2\theta^2 + 4\gamma^2\omega_1/E} \quad (2.36)$$

We can see that the Compton photon energy is depending on the scattered angle and electron energy. For smaller scattered angle we have larger energy of the Compton photon.

Figure 2.6 shows the energy spectrum of scattered photons from simulation by CAIN. The laser wavelength is $1064nm$, which means photon energy $1.164eV$. Energy of electron beam is $1.28GeV$. Consider different incident angle $0^\circ, 12^\circ$ and 90° . We can see that small incident angle can produce more photons with large energy[21].

Figure 2.7 is the energy spectrum of produced photons. Where the incident laser is totally right circular polarized. Laser wavelength is $1064nm$ and incident electron energy is $1.28GeV$.

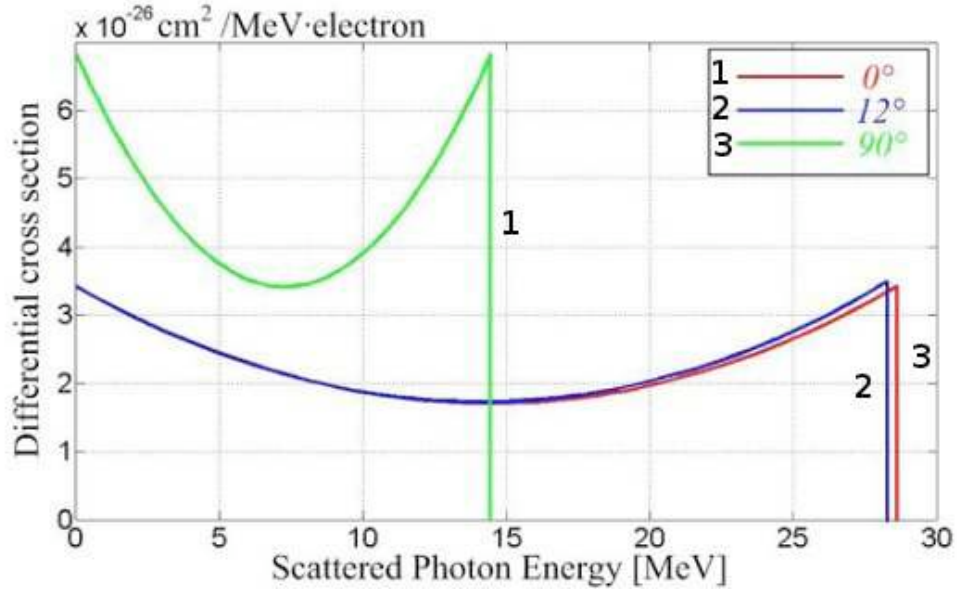


Figure 2.6: Spectrum for produced γ in Compton back-scattering. Incident laser wavelength: 1064 nm . Incident electron energy: 1.28 GeV . [21]

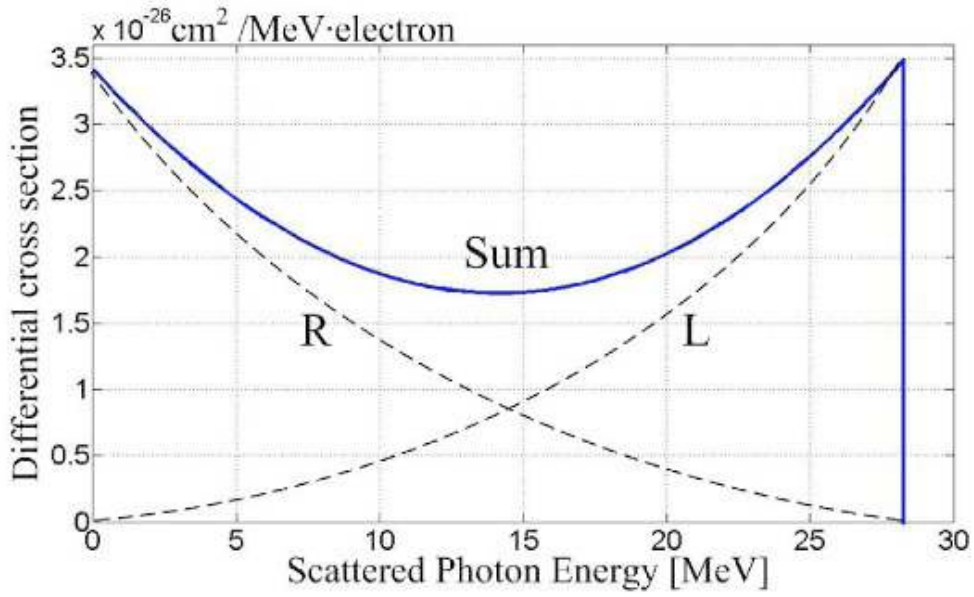


Figure 2.7: Spectrum for produced γ in Compton back-scattering with right polarized laser. Incident laser wavelength: 1064 nm . Incident electron energy: 1.28 GeV . R means right polarization, L means left polarization. [21]

2.2.4 Channeling radiation

In crystals, regular arrangement of atoms constitute a lattice which behaves roughly like a wiggler[22]. When charged particles are incident on a crystal oriented to low-index crystallographic direction, that is, close to low-index axes and planes, collective and coherent effects are expected with respect to amorphous target. In the interaction with crystal the charged particles which are completely governed by many correlated collisions with lattice atoms are channeled.

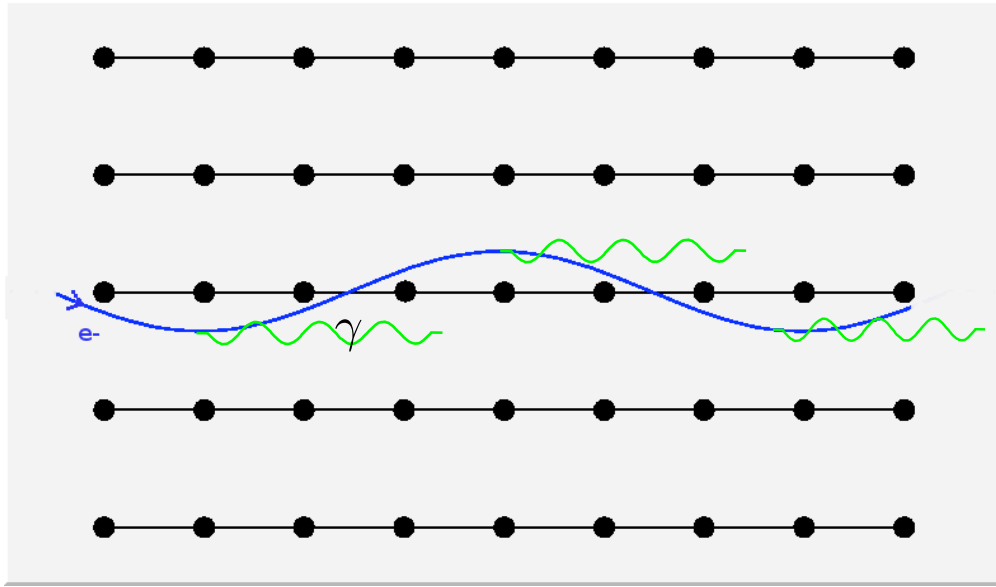


Figure 2.8: Axial channeling demonstration

In axial channeling, the particles will develop a quasi periodic trajectory around the atomic strings what is so called "rosette motion", in which the particles are running nearly parallel to the atomic string in z direction under the first approximation[23]. It can be approximated by distributing the atomic charges uniformly along the string direction. The interaction with atomic string can be treated as the movement in an averaged potential.

Let $\bar{V}(\vec{r}_\perp)$ be the averaged transverse potential

$$\bar{V}(\vec{r}_\perp) = \frac{1}{d} \int_{-\infty}^{\infty} dz V(\vec{r}_\perp, z). \quad (2.37)$$

where d is the space between atoms on the string. The transverse energy,

$$E_T = \frac{1}{2} E v_T^2 + U(\vec{r}_\perp) \quad (2.38)$$

where $U(\vec{r}_\perp) = e\vec{V}(\vec{r}_\perp)$; \vec{r}_\perp is a radius-vector; $v_T = P_\perp/E$ is the angle of the trajectory with the propagation axis.

If $E_T > 0$ the atomic string can not capture the charged particles[23]. This determines the channeling condition $E_T < 0$, which gives the critical angle

$$\psi_c = \sqrt{\frac{2U_0}{E}} \quad (2.39)$$

where U_0 is the depth of the potential well.

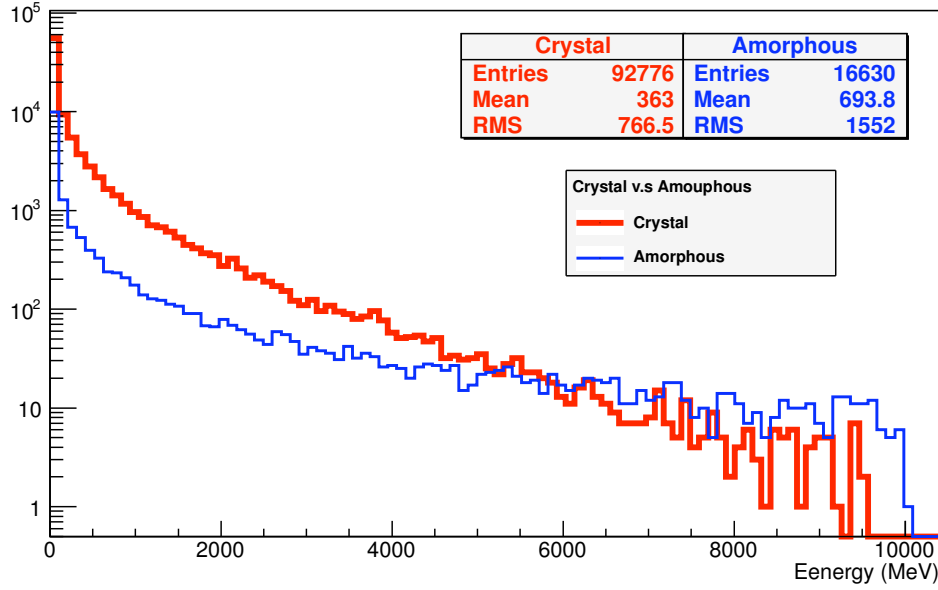


Figure 2.9: Photon spectrum from e- beam impinging on tungsten crystal(with $\langle 111 \rangle$ direction) and amorphous target. Incident energy: 10GeV . Incident number: 5000. Target thickness: 1mm

In the rosette motion of charged particles, the electrons will radiate. The collective and coherent effects will appear because of the regular structure of the target, more photons will be emitted compared with amorphous target. Because of the very strong fields and very short periods of channeling which present a few thousand inter-atomic distance, the emitted photon has a frequency much higher than a normal magnetic wiggler with the same incident electrons. The frequency can be written as

$$\omega = 2\gamma^2 \Delta E_T \quad (2.40)$$

where γ is the Lorentz factor, ΔE_T is a few eV which is the transverse energy loss between channeled states. As the charged particles energy increase, the potential

well is deeper, in the electron frame, by the factor γ because of relativistic effect which increase the frequency of emitted photon[22].

Figure 2.9 shows a spectrum comparison of radiated photons between amorphous and crystal target under the same thickness. It can be seen that the yield for the crystal is higher than amorphous with a high amount of soft photons. This is because in channeling effect, the electron encounters a sequence of soft collisions with atomic string in which large amount of soft photon are radiated. It can be illustrated by saying that the average radius of curvature of the electron trajectory near an individual atom has a small curvature radius, whereas with channeling condition in a crystal the electron trajectory influenced by N nuclei has much larger curvature radius and as in synchrotron radiation, large radius leads to softer photons. While in the amorphous target the random arrangement of atoms make the electrons have a high possibility of encountering individual atoms with a small impact parameter. So the photons in amorphous are more harder than in crystal.

As the collective effect, the number of radiated photons is considerably N times higher with respect to an amorphous target, where N represents the number of atoms within "coherent length":

$$l_{coh} = \frac{E(E - \omega)}{m^2\omega^2} \quad (2.41)$$

When the incident angle is much higher than critical angle, another phenomena may happen: coherent bremsstrahlung, in which the incident particles cross regularly planes or strings of atoms. Because of the regular structure of crystal, oscillations with interference effects occur(see Fig. 2.10).

2.3 Schemes for polarized photons

2.3.1 Helical undulator scheme

Figure 2.11 is the layout for the helical undulator. The 150 GeV electron main linac beams passes through a long helical undulator to generate a multi-MeV photon beam. The photon beam impinging on a thin metal target to generate positrons in an electromagnetic shower. The positrons are captured, accelerated and transported to the Damping Ring[24].

The helical undulator for ILC must be superconducting to achieve the required parameters of high field. The Undulator period is $11.5mm$. Two interleaved helical

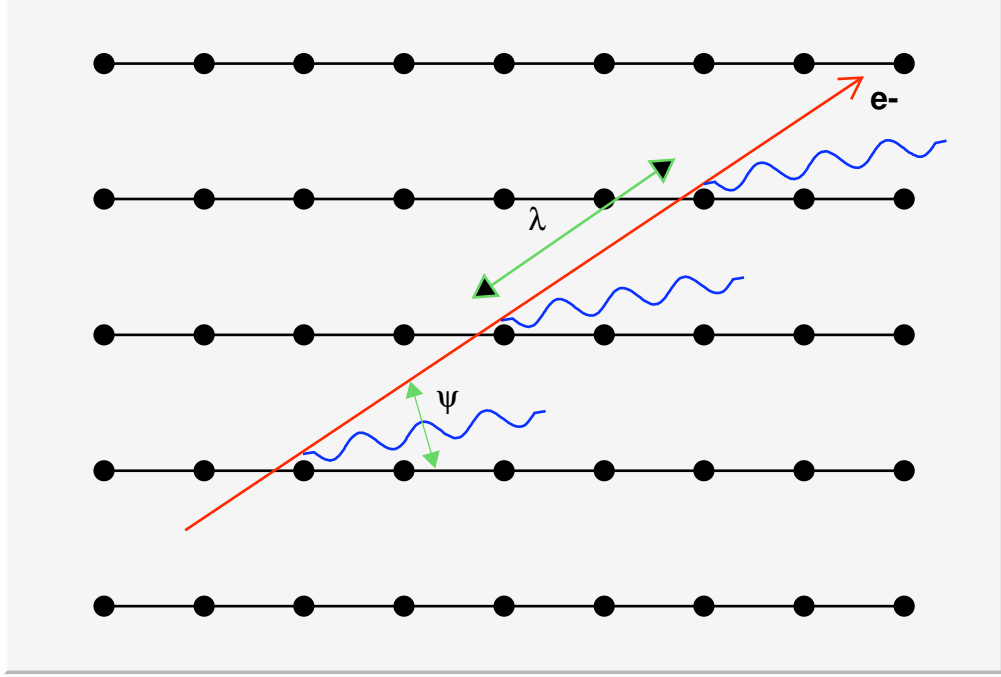


Figure 2.10: Coherent bremsstrahlung in crystal medium.

windings of NbTi spaced half a period apart generate the transverse helical field what is $0.86T$. The active undulator length is $147m$ long which is constituted by forty-two $4m$ long cryomodule, each cryomodule has an active length of $3.5m$. Injecting an electron beam with energy of $150GeV$ will produce photon beam with circular polarization. The first harmonic of the photon spectrum is $10MeV$ and the photon beam power is $131kW$.

The undulator vacuum chamber has a nominal inner diameter of $5.85mm$ and is made of copper. The supper conductivity of copper at cryogenic temperatures will mitigate resistive wall effects. The material between the superconducting windings is soft magnetic iron which can increase the field. Each cryomodule contains a liquid helium bath. In-situ cryocoolers are used to achieve zero liquid boil off.

2.3.2 Compton back-scattering scheme

GeV electron collides with circularly polarized laser beam can produce MeV photons. This is based on Inverse Compton scattering. Fig. 2.12 shows the KEK-ATF demonstration. It is consisted by the injection linac and equipped with a photocathode RF gun, a damping ring and an extraction line[25]. The energy of electron

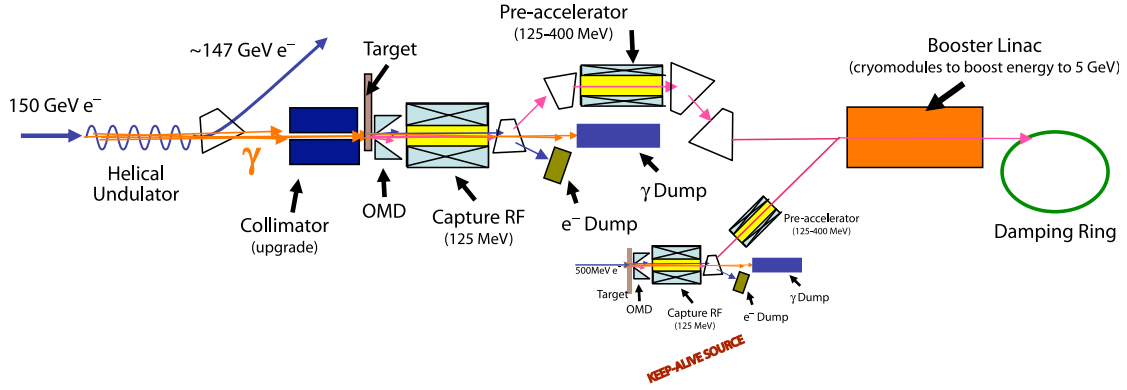


Figure 2.11: Overall layout of the Positron Source using undulator[24]

beam is 1.28GeV . The circumference of the damping ring is about 140 m.

In order to increase the laser power, a laser pulse stacking system with the optical resonant cavity is needed. The laser oscillator produces laser pulses of 28 nJ/pulse with a repetition rate of 375 MHz . The wavelength is 1064 nm and pulse width is 4 ps . The optical resonant cavity is a Fabry-Perot cavity with spherical mirrors of 99.6% reflectivity and 210.5 mm curvature at both ends.

The optical resonant cavity is designed to stack power by about thousand times and to focus the laser pulses by the spherical mirrors. The waist size of the laser at the focus point inside the cavity is about $30\text{ }\mu\text{m}$. The optical resonant cavity for laser-Compton scattering is installed on movable table to make sure that the laser position can be moved with respect to the electron beam. The accuracies are 0.8 and $4\text{ }\mu\text{m}$ in vertical and horizontal directions.

The electron beam and laser pulses will be synchronized to collide with an angle of 8 degree. MeV photons with circular polarization will be produced because of Compton back scattering.

2.3.3 Polarized bremsstrahlung scheme

Future high energy e^-e^+ colliders need high luminosity and physics capability. High luminosity requires low beam emittance and using polarized beam can expand the physics capabilities.

The production of polarized electrons is well understood. A photo-emission in a semiconductor photocathode like AsGa can produce an electron beam with a degree of 75 – 80% for longitudinally polarization. However the production of

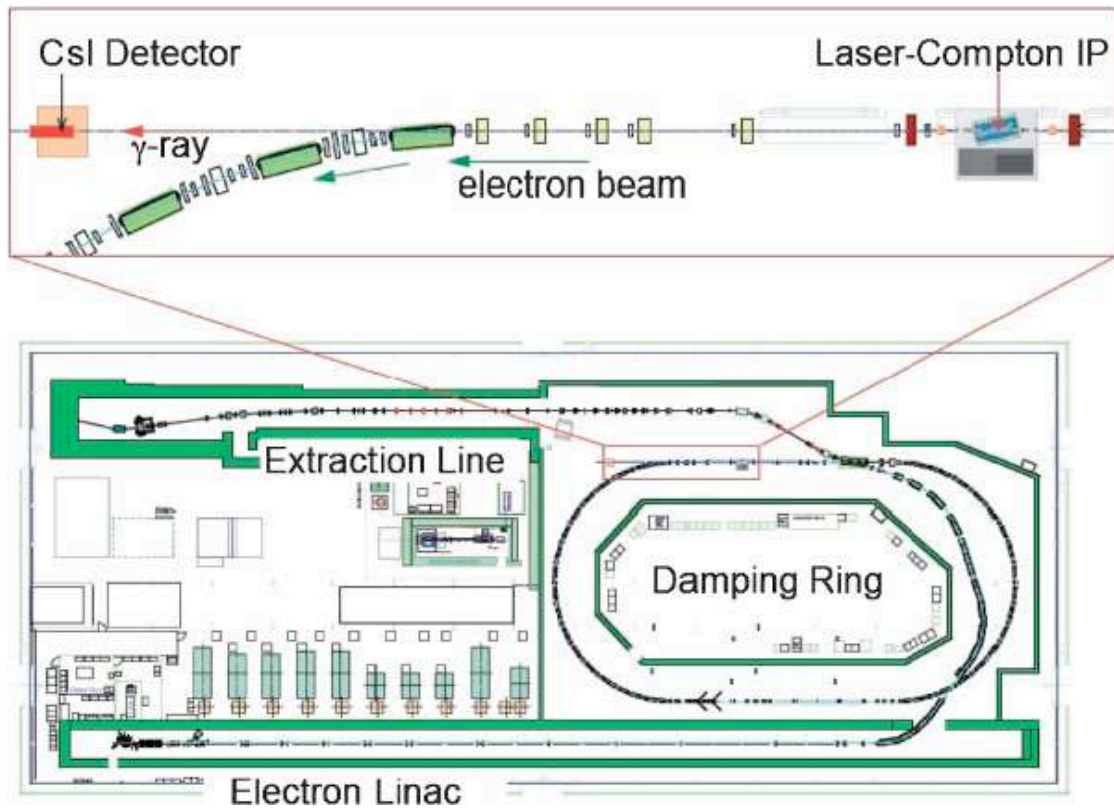


Figure 2.12: KEK-ATF accelerator complex (lower figure). The upper figure shows a magnified view of position in the optical resonant cavity and photon detector[25].

intense polarized positron beam need more significant R&D yet.

Another scheme for the polarized photon is using low energy polarized electron beam to strike a thin metal target[26]. As V.M.Straknovenko mentioned, when circularly polarized photon passing through the converter, the produced positrons may depolarize mainly due to three effects:

1. Bremsstrahlung effect;
2. Bhabha scattering on the target electrons;
3. Multiple scattering in the Coulomb field of nuclei.

To limit the depolarization, a low energy($\sim 50MeV$) electron beam with longitudinal polarization is used to impinge on thin target $\sim 0.2X_0$. The low energy of incident particles and thin target thickness can limit the depolarization of positrons.

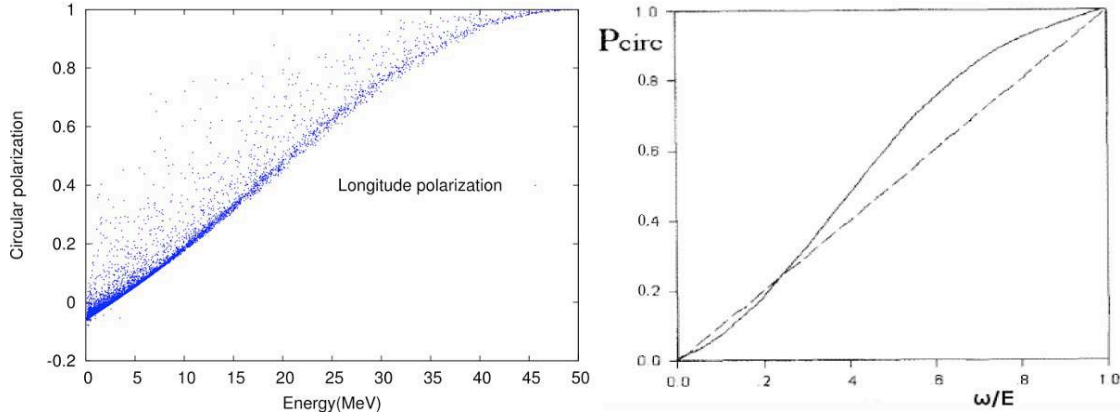


Figure 2.13: Circular polarization for the produced photons. Incidence: electron. Incident energy: $50MeV$. Incident number: 1 million. Converter: tungsten. Target thickness: $0.2X_0$. Left: Monte-carlo results. Right: numeric result from Potylitsin[26].

Here we give some simulation results about this scheme (see Figs. 2.13 and 2.14). An electron beam with totally longitudinal polarization impinging on a $0.2X_0$ thickness tungsten amorphous target. The incident energy is $50MeV$ which will reduce the depolarization from bremsstrahlung. The thin target thickness can control the scattering times also. The Fig. 2.13 and 2.14 show the circular polarization for produced photons and longitudinal polarization for positrons.

For produced positrons, the total yield is $0.95(N^{e+}/N^{e-})$, which means longitudinal polarization is 0.28. For photons, the mean circular polarization is 0.15. Our results agree well with numeric calculation from A.P Potylitsin.

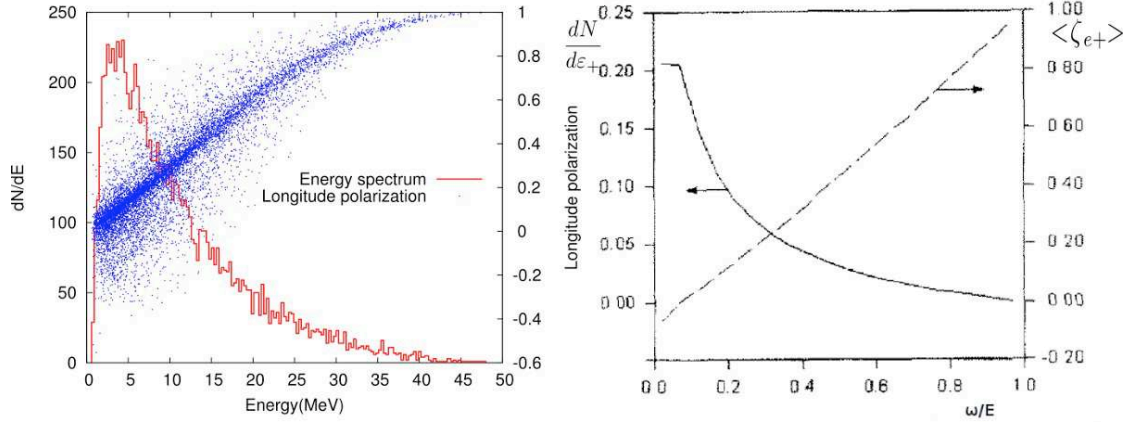


Figure 2.14: longitudinal polarization for the produced positrons. Incidence: electron. Incident energy: 50MeV . Incident number: 1 million. Converter: tungsten. Target thickness: $0.2X_0$. Left: Monte-carlo results. Right: numeric result from Potylitsin[26].

2.4 Pair production

2.4.1 Pair production in amorphous medium

When a photon with enough high energy passes by nuclei, this photon may materialise into an e^-e^+ pair. This process is called pair production, which is a quantum phenomenon and does not have a classical description.

In order to describe the dynamics of relativistic electron, Dirac developed a theory. According to his theory a free electron has energy $\pm\sqrt{(mc^2)^2 + p^2c^2}$. If the electron is at rest, we have $\pm mc^2$. This solution permits negative values. It looks strange, but Dirac predicted that there exists a type of particle with the same properties as electron except inverse charge. The observation of positron (By C. Anderson) proved Dirac's prediction.

As pointed out by many authors, we can remark that if negative electrons states exist, the Pauli Exclusion Principle requires that all the negative states be filled. It would be, then, possible to imagine an infinite sea of negative energy electrons. This sea is referred as the Dirac sea. If an impinging photon is giving enough energy to an element of this negative energy sea, it would be allowed to rise into the positive energy state (Fig. 2.15). It results a hole in the negative energy sea. This hole corresponds to an absence of negative charge, henceforth, it appears as positively charged. This hole has the same mass as the electron but with positive charge.

Because of energy and momentum conservation, pair production can only take place when a photon passing the electric field of the nuclei. The electron and positron has rest energy of $m_e c^2$. So according to the energy conservation, the photon must have energy more than the sum of e-e+ pair: $1MeV$.

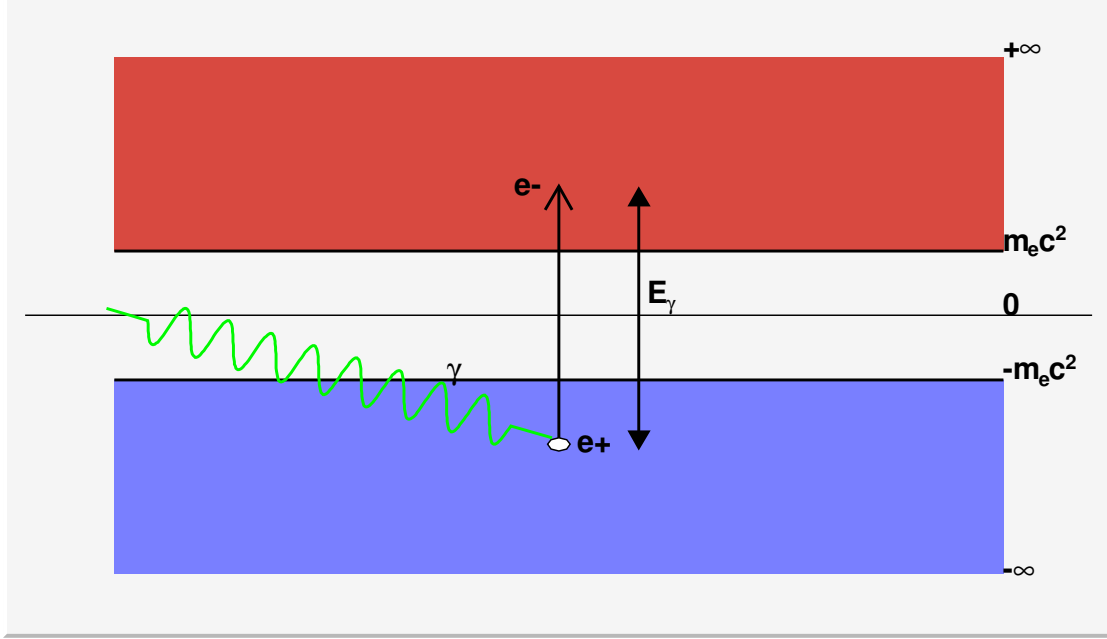


Figure 2.15: Excitation of electron from negative-energy state to positive-state by high energy photon

Bethe-Heitler developed the cross section for pair production by a very high energy photon passing a nucleus and taking into account the screening effect[17, 27]:
for $m_e c^2 \ll E \ll 137m_e c^2 Z^{-1/3}$:

$$\sigma_{pair} = \frac{Z^2}{137} r_e^2 \left(\frac{28}{9} \ln \frac{2E}{m_e c^2} - \frac{218}{27} \right) \quad (2.42)$$

for $E \gg 137m_e c^2 Z^{-1/3}$:

$$\sigma_{pair} = \frac{Z^2}{137} r_e^2 \left(\frac{28}{9} \ln \frac{183}{Z^{1/3}} - \frac{2}{27} \right) \quad (2.43)$$

Eqs. (2.43) and (2.18) show that at very high energy region the cross section of pair production is similar to bremsstrahlung.

The pair production can be simply processed by Fermi's treatment to the bremsstrahlung (see §2.2.1) in which a fast electron scatter the virtual photons of nuclei. Consider a very high energy photon passes near a nucleus. Transform to a new frame where the nuclei move toward photon with a velocity very near c , where the nuclei looks like a wave of photons. The incident photon in this frame will reduce its frequency. The process can be simply treated as a collision between incidence with virtual photons: $(h\nu + h\nu \rightarrow e^- + e^+)$.

For very high energy photons, the cross section can be approximated as

$$\sigma_{pair} \sim \frac{Z^2}{137} r_e^2 \frac{28}{9} \ln \frac{183}{Z^{1/3}} \quad (2.44)$$

For pair production the mean free path can be defined:

$$l_p = \frac{1}{N\sigma_{pair}} \quad (2.45)$$

where N represents the nuclei density. The decrease of photon beam density is:

$$\frac{dn}{n} = -\frac{dx}{l_p} \quad (2.46)$$

Which give the solution

$$n = n_0 e^{-x/l_p} \quad (2.47)$$

Comparing with radiation length Eq. (2.14), we find that

$$l_p = \frac{7}{9} X_0 \quad (2.48)$$

The bremsstrahlung and pair production are the main processes for a shower phenomenon. The shower can be initiated by an electron or a photon. By a photon for example, the photon disappears and an e-e+ pair will be created when the photon pass by a nucleus. The high energy electron or positron emits photons, then the photons creat e-e+ pair... As the process continue, the incident energy soon dissipates among the secondaries, and the number of secondary particles increase quickly. As the emitted photons have not enough energy to create e-e+ pair, the number of electron, positron and high energy photon decrease and all the energy will dissipate in excitation and ionization of the atoms[15].

The exact process is very complex. Here are some results from Monte Carlo simulation. The Fig. 2.16 is the total yield (Number of particles per incident electron) of electrons and positrons in a shower initiated by 1000 electrons. The material is tungsten, and the incident energy is $1GeV$ for the left figure and $10GeV$

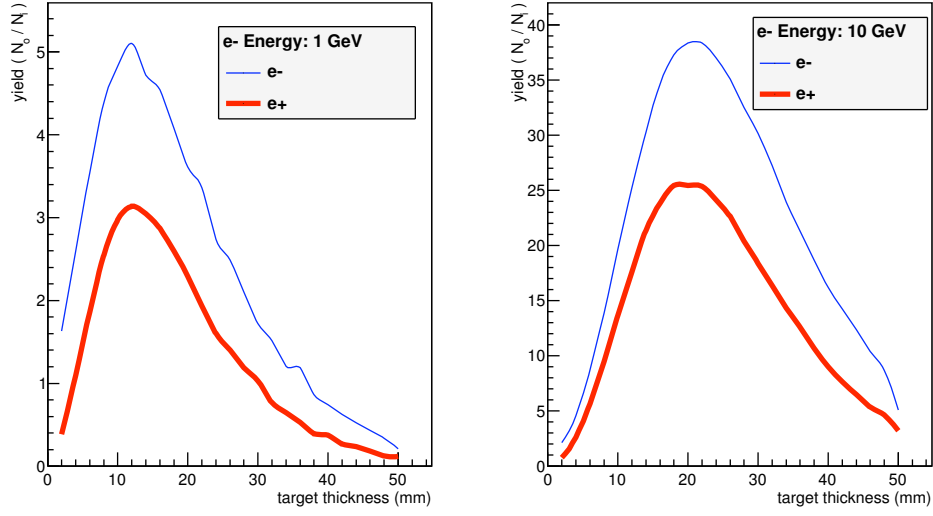


Figure 2.16: The total yield of electrons and positrons in a shower initiated by 1000 electrons of energy E_0 , substance tungsten. Abscissa: target thickness. Ordinate: yield. Left $E_0 = 1\text{GeV}$. Right $E_0 = 10\text{GeV}$ [Geant4]

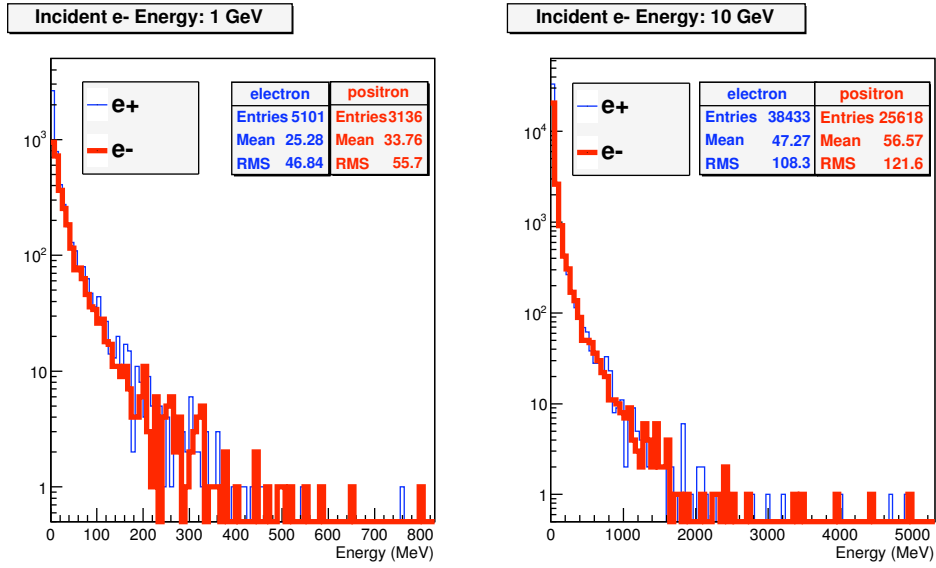


Figure 2.17: The spectrum of electrons and positrons at optimum thickness. Abscissa: Energy. Left: $E_0 = 1\text{GeV}$. Right $E_0 = 10\text{GeV}$

for right. It shows that the electron yield is larger than the positron yield with the same condition. At beginning the yield increases as the thickness increases, then after a maximum it decreases. The optimum thickness is $12mm$ for left figure and $19mm$ for the right figure.

The shower optimum position can be calculated theoretically with some approximation, in which the Compton effect and the collision loss are neglected, the asymptotic formulas for radiation and pair production are used. The results are: Primary electron of energy E_0 [15]

$$T_{II}^{(\pi)}(E_0, 0) = 1.01 \left[\ln \frac{E_0}{\varepsilon_0} - 1 \right] \quad (2.49)$$

Primary photon of energy E_0

$$T_{II}^{(\gamma)}(E_0, 0) = 1.01 \left[\ln \frac{E_0}{\varepsilon_0} - \frac{1}{2} \right] \quad (2.50)$$

ε_0 is the critical energy, which is defined as the particle energy for which radiation loss equals to the ionization loss.

2.4.2 Pair production in crystals at very high energy

Another pair production process occurs at very high photon energies with a very small incidence angle on the crystal axis, which is different from the classical one described by Bethe-Heitler. Such a process becomes important enough at multi-GeV energies and high crystal fields. The threshold of the pair production becomes more important than the Bethe-Heitler previsions, which is defined by:

$$\omega = \frac{m^3 c^4 \rho d}{\hbar^2 Z \alpha} \quad (2.51)$$

where ω is the incident photon frequency; ρ is the thermal vibration amplitude; d is the interatomic distance; $\hbar = h/2\pi$; h is the Planck constant; Z is the atomic number and α is the fine structure constant.

This threshold depends on the crystal structure and makes materials with large Z and small ρ (cooled materials) becomes more interesting. As an example, the tungsten crystal has a threshold of 13 GeV at $100^\circ C$ and 20 GeV at room temperature; whereas the Germanium crystal has a threshold of 50 GeV at $100^\circ C$ and 100 GeV at room temperature [28]. An experiment made at CERN with a germanium crystal aligned on its $\langle 110 \rangle$ axis and cooled at $100^\circ K$ confirmed

the threshold value and the enhancement on pair production. That enhancement represented about one order of magnitude with respect to Bethe-Heitler value with a photon beam of 150 GeV[29].

2.5 Ionization

Charged particles moving through matter lose energy by interactions with atomic electrons, in which the atomic electrons will acquire some energy and be raised to high level states. If the final state is a continuum level it is an ionization process, Otherwise it is an excitation process. Here "ionization" refers to both of the processes. Ionization loss in target is harmful, and it will heat the target and induces the shock wave which may destroy the target. It's a key problem in high intensity positron source.

To calculate the ionization loss by a heavier particle of charge ze propagating through a medium, first assume the incident particles do not change its movement direction. Consider the atomic electrons as free and at rest, the collision as lasting such a short time that the electron acquires an impulse without changing its position during the collision[30]. By this hypothesis the energy loss per path length is:

$$-\frac{dE}{dx} = 4\pi N \frac{z^2 e^4}{mv^2} \ln \frac{b_{max}}{b_{min}} \quad (2.52)$$

where N is the electron density, b_{max} is the maximum impact parameter and b_{min} is the minimum impact parameter, m and v correspond to the incident mass and velocity.

If the incident particles are electrons, the situation is complicated and the previous assumption is invalid. There are mainly two reasons. The first one is the trajectory change of the incident electron is not negligible when collides with atomic electrons. Because the incident electron will acquire a transverse momentum which is equal to the ejected electron. The second one is for the collision between identical particles the exchange phenomena will occur and should be taken into account. Bethe and Ashkin derived the equations of collision loss by electrons, which gives[30]:

For non-relativistic electron the energy loss per path length dx is:

$$-\frac{dE}{dx} = \frac{4\pi e^4 N}{mv^2} \left(\ln \frac{mv^2}{2I} - \frac{1}{2} \ln 2 + \frac{1}{2} \right) \quad (2.53)$$

For high relativistic velocities the energy loss of electrons is

$$-\frac{dE}{dx} = \frac{4\pi e^4 N}{mc^2} \left(\ln \frac{mc^2}{2I} - \frac{3}{2} \ln(1 - \beta^2)^{1/2} - \frac{1}{2} \ln 8 + \frac{1}{16} \right) \quad (2.54)$$

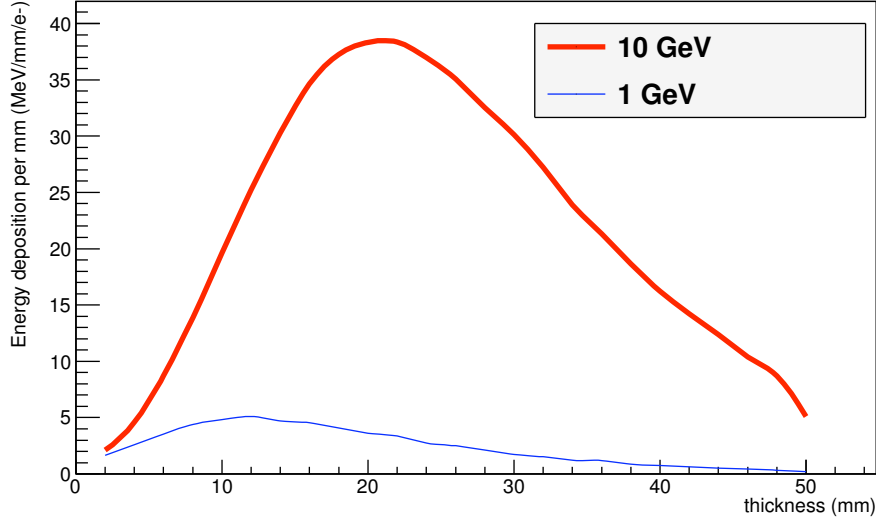


Figure 2.18: Energy deposition per mm for electrons impinging on amorphous tungsten, two kinds of energy are used: 1GeV and 10GeV . Abscissa: target thickness (mm). Ordinate: Energy deposition per incident e- per mm.

From the above two formulas, in the non-relativistic region the ionization loss decreases quickly as the incident energy increases. Because it is approximately proportional to $1/mv^2$. In relativistic condition the energy loss increases slowly as the incident energy increases. There are two aspects: The increase of b_{max} and decrease of b_{min} . The first is, in quantum theory, the perturbation must be small during the periods $b/v < \tau = 1/\nu$ which determines $b_{max} = v/\bar{\nu}$. Where $\bar{\nu}$ is an appropriate average of the frequencies of the atom. When incident electron energy increases, the maximum impact parameter increases as $b_{max} = v/\bar{\nu}(1 - \beta^2)^{1/2}$. The second point, in quantum mechanics the minimum impact parameter should be less than de Broglie wavelength of particles. As energy increases, the de Broglie wavelength of incident particle decreases, so the minimum impact parameter decreases.

Figure 2.18 shows the energy deposition per incidence per mm with 1000 electrons impinging on a tungsten target. The incident energy of 1GeV and 10GeV are considered. Figure shows that, at first the radiation loss is dominant as particles' average energy is high. Then with thickness increases, the average energy

decreases so the collision loss become dominant gradually. Here we can define the critical energy ε_0 [15]: particles with the energy ε_0 that the radiation loss per radiation length is equal to the collision loss per radiation length. ε_0 is the solution of the following equation. For tungsten, ε_0 has a value of $\sim 8MeV$.

$$-\left(\frac{dE}{dt}\right)_{col} = -\left(\frac{dE}{dt}\right)_{rad} \quad (2.55)$$

where $t = x/X_0$, is in terms of radiation length X_0 .

2.6 Coulomb scattering on crystal nuclei

The reliability of the crystal sources is based on their long-term resistance to radiation damages. The main source of damage is Coulomb scattering of the beam on the nuclei of the crystal, where fast charged particles may have elastic collisions with the nuclei of the crystal. For the nucleus with certain levels of the recoil energy, the latter may be dislodged from its lattice site or can initiate a cascade of displacements among the neighbouring atoms.

The recoil energy transfered to the nucleus is written as:

$$T = \frac{Q^2}{2M} \quad (2.56)$$

where Q is the transfer momentum, M is the mass of the nucleus. Take tungsten as an example, if the recoil energy T is above some threshold E_d , about 25 eV, the nucleus will be dislodged from its lattice site[31]. If $T > 2E_d$, the dislodged nucleus can initiate a cascade of displacements among the neighbouring atoms. The primary displacement cross section is given by[3]:

$$\sigma_d = \frac{Z^2}{AE_d} 1.431 \times 10^{-22} cm^2 \quad (2.57)$$

where A and Z are the atomic mass and number. The average number of dislodged atoms per primary displaced ones is defined as[3, 31]:

$$\bar{n} = 1 + 0.5 \ln(L_c/2E_d) \quad (2.58)$$

where $L_c = A \times 1keV$, A is the atomic mass of the nucleus.

Degradation of channeling properties of the crystal has been estimated for a fraction of dislodged atoms ($\sim 1\%$). This corresponds to the probability of nuclear interaction in our crystal. In that case the critical fluence scales from 10^{19} to $10^{21} cm^{-2}$ depending on the crystal, and the most interesting crystal is diamond.

Chapter 3

Simulation

This chapter will discuss two subjects. One is a benchmark for the Geant4 Simulation, where different incidence, incident energy and target material are considered; Yield, polarization of produced e^+ , total energy deposition and PEDD will be presented. The other is the simulation of the positron source, where a hybrid target system is to be presented. The choice of two amorphous target, compact target and granular target, is discussed. Three types of capture will be talked: AMD, QWT and Lithium lens. Some comparison are made. Average heating and PEDD are also discussed. Granular target cooling, examples about ILC case and CLIC case are presented.

3.1 Benchmark of Geant4 simulation

The program used in simulation of positron source is written in C++ and Geant4 Toolkit[32]. In order to have a common basis for the simulation and check the program, lots of simulations have been made. The Geant4 simulation tests agree well with EGS code[33]. In these tests, electron and γ are considered as incident beam with or without polarization. RMS of 1 mm and 2.5 mm are considered as transverse incident dimension. The incidences are mono-energetic and the following values are used: 100 MeV, 200 MeV, 300 MeV, 1 GeV, 5 GeV and 10 GeV. Two metals are chosen as the target material: tungsten and titanium. Target thickness is from 0.4 to $4 X_0$, eight values are used. The transverse sizes of the target in x and y are 2 cm. The cell volume for counting energy deposition density is $1mm^3$ for titanium and $0.7mm^3$ for tungsten. The cut-off energy is same for electron, positron and photon: $1mm$ which is about $2MeV$ following Geant4 specification. The incident particle number is 1000 for all the cases.

Figure 3.1 shows the total positron yield from electron or photon incident on a tungsten or titanium target. It shows that the yield increases with the target thickness. For the same material and incident energy the difference of positron yield between incident electron and photon is rather small. The total yield from tungsten target is larger than the titanium target for the same incident energy and incident particle.

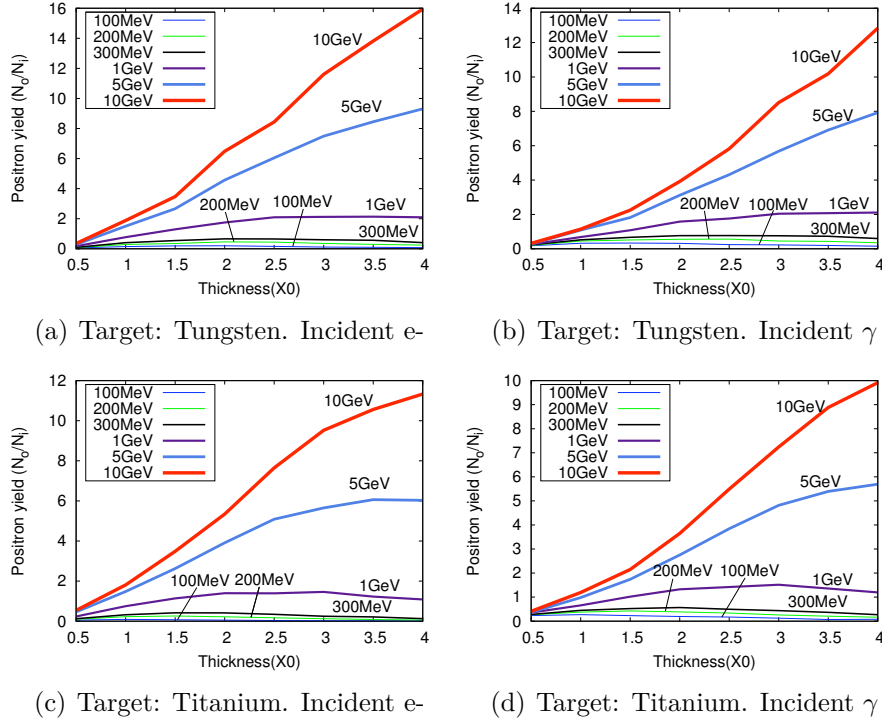
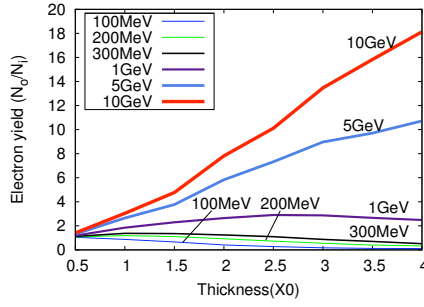


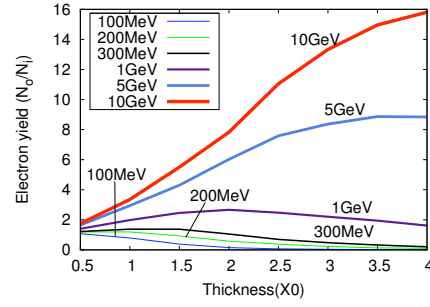
Figure 3.1: Total yield of positron

Figure 3.2 shows the total yield for electron and γ . The incident particles are electrons. The tungsten and titanium target are compared. The yields of electron are similar but a little larger than the positron. With the same conditions the γ yields for tungsten are larger than titanium target.

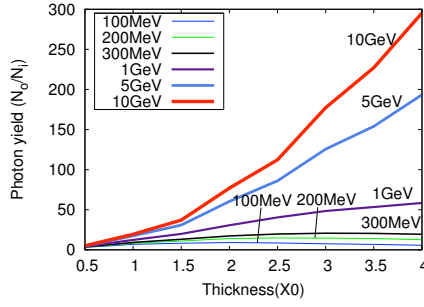
As the target thickness increases, the mean and rms values of the energy of produced particles decrease. This is because as the thickness increases the charged particles radiate and lose energy. The smaller energy of charged particle, the smaller energy the radiated γ . This results in smaller energy for produced $e-e^+$ pair. For the same material and incident energy, the incident photon produces higher energy positron than incident electron. This is because energy of γ radiated by incident electron is sure smaller than incident γ if the incident elec-



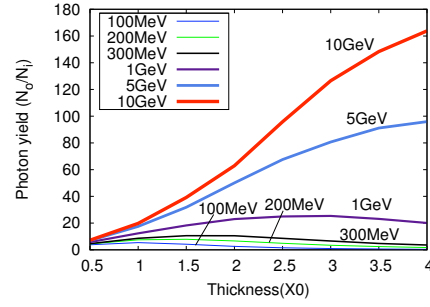
(a) Target: Tungsten. Produced particles: e^-



(b) Target: Titanium. Produced particles: e^-



(c) Target: Tungsten. Produced particles: γ



(d) Target: Titanium. Produced particles: γ

Figure 3.2: Total yield of electron and γ . Incident particles: electron

tron and γ have the same energy. So the secondaries of e-e+ pairs produced by the incident electron have a smaller energy than incident γ case. Tabs.3.1-3.4 list the mean and rms values for produced positrons. Two types of incident particle(electron and photon) are used to impinge on a tungsten target.

Table 3.1: Mean Energy for produced positrons. Target material: Tungsten. Incidence: e-. Incident size: 2.5 mm. Energy unit: MeV. Target thickness unit: X_0

Thickness(X_0)	100MeV	200MeV	300MeV	1GeV	5GeV	10GeV
0.4	20.15	29.81	41.17	118.04	384.29	752.67
1.0	18.04	30.83	42.21	85.14	237.83	420.62
1.4	15.13	27.29	34.55	73.38	198.03	330.42
2.0	16.47	21.34	29.11	61.41	159.46	225.08
2.4	15.66	21.66	26.69	53.59	123.76	185.11
3.0	14.06	24.01	24.81	47.17	95.62	133.42
3.4	12.87	19.54	22.84	44.57	83.13	116.04
4.0	12.66	19.36	22.76	37.38	70.57	94.83

Table 3.2: RMS of Energy for produced positrons. Target material: Tungsten. Incidence: e-. Incident size: 2.5 mm. Energy unit: MeV. Target thickness unit: X_0

Thickness(X_0)	100MeV	200MeV	300MeV	1GeV	5GeV	10GeV
0.4	17.29	30.73	41.94	162.95	688.01	1441.28
1.0	13.89	27.84	41.72	120.05	442.73	856.98
1.4	11.95	26.02	35.61	101.57	387.57	697.39
2.0	14.13	19.76	29.62	89.24	330.99	531.57
2.4	11.99	18.38	28.29	77.36	249.56	454.42
3.0	13.32	23.83	24.97	63.21	203.3	317.21
3.4	10.12	18.41	24.05	65.21	173.76	293.88
4.0	9.81	21.36	24.84	60.81	162.14	234.46

The polarization of the incidences are set to be totally longitudinal(parallel) for the electrons and totally circular(right) for the photons. Fig. 3.3 shows the polarization for produced particles, where the target material is tungsten and

Table 3.3: Mean Energy for produced positrons. Target material: Tungsten. Incidence: γ . Incident size: 2.5 mm. Energy unit: MeV. Target thickness unit: X_0

Thickness(X_0)	100MeV	200MeV	300MeV	1GeV	5GeV	10GeV
0.4	44.46	87.72	132.22	360.98	1690.05	3542.4
1.0	35.01	67.47	93.73	233.57	836.67	1478.32
1.4	30.21	57.83	74.66	181.45	555.04	871.95
2.0	28.76	45.85	58.95	112.15	302.78	498.02
2.4	27.07	39.65	48.88	93.33	229.68	355.73
3.0	24.45	33.07	41.44	71.94	162.35	231.55
3.4	24.99	33.91	38.58	67.15	125.29	191.31
4.0	24.58	29.22	35.73	51.65	102.08	135.07

Table 3.4: RMS of Energy for produced positrons. Target material: Tungsten. Incidence: γ . Incident size: 2.5 mm. Energy unit: MeV. Target thickness unit: X_0

Thickness(X_0)	100MeV	200MeV	300MeV	1GeV	5GeV	10GeV
1.0	23.04	49.19	76.45	243.48	1170.18	2263.37
1.4	21.87	46.06	69.34	214.37	939.24	1664.27
2.0	21.95	42.14	59.51	162.41	634.05	1157.79
2.4	22.09	37.16	52.4	144.62	503.65	938.28
3.0	19.18	34.54	49.18	116.43	397.07	641.84
3.4	20.28	35.08	47.18	111.92	325.95	611.12
4.0	21.12	31.01	46.14	85.98	246.04	403.35

incidences are electron or photon. It shows that as the target thickness increases the mean polarization decreases if other conditions are fixed. This is because as the thickness increases the bremsstrahlung and multiple scattering processes will lead to depolarization. With the incident energy increases, the average polarization of the produced particles decreases. This is due to the fact that high energy particle has a higher possibility to encounter bremsstrahlung. To control the polarization of produced particles, we should limit the target thickness and use low energy incidences.

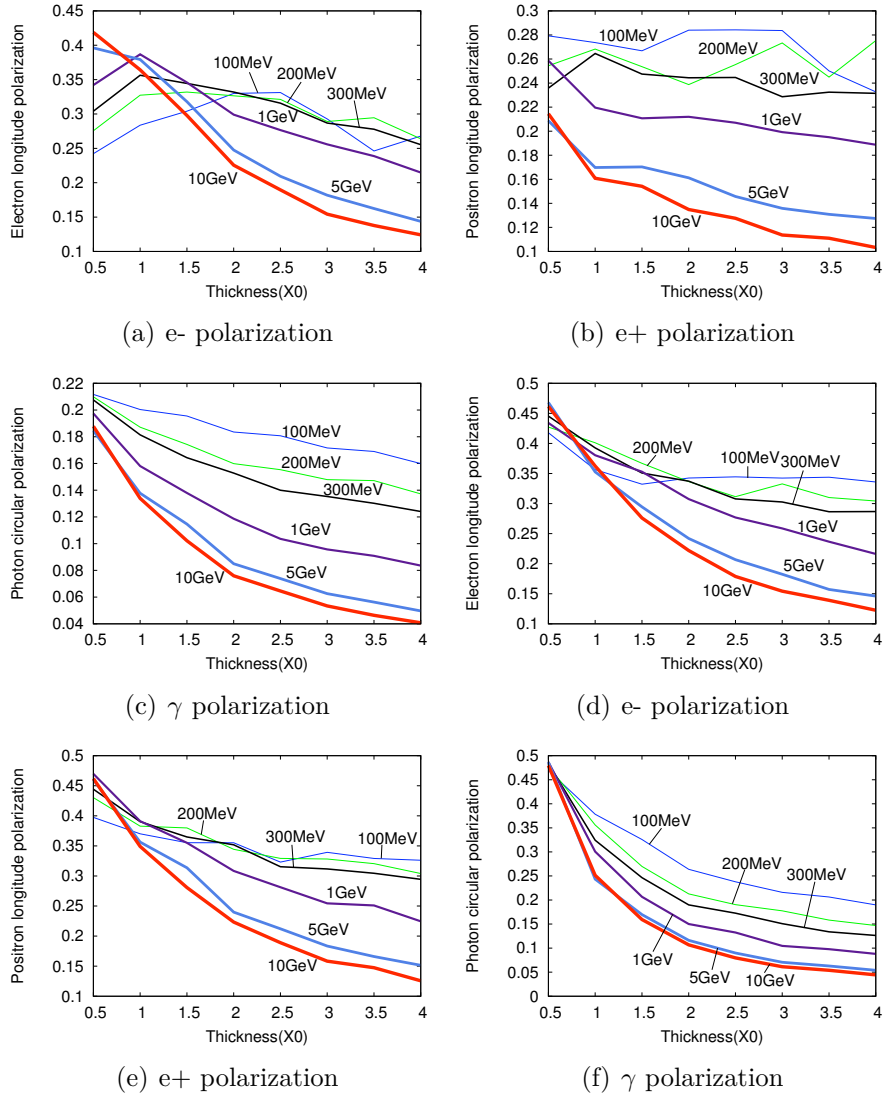


Figure 3.3: Polarization for produced particles. Target material: Tungsten. (a)-(c): Incident e-. (d)-(f): incident γ

Figure 3.4 shows the total energy deposition in different targets using different incidences and incident energies. If other conditions are the same, the energy deposition in the tungsten target is less than that in the titanium target. This is because the critical energy of titanium($\sim 26\text{MeV}$) is larger than tungsten($\sim 8\text{MeV}$). The charged particles with energy between the critical energy of titanium and the critical energy of tungsten will tend to radiate photon in tungsten target but encounter more ionization in titanium target. This will lead to a higher energy deposition in titanium target than in tungsten target. For the same target and incident energy, the energy deposition for incident electrons is more than for incident photons.

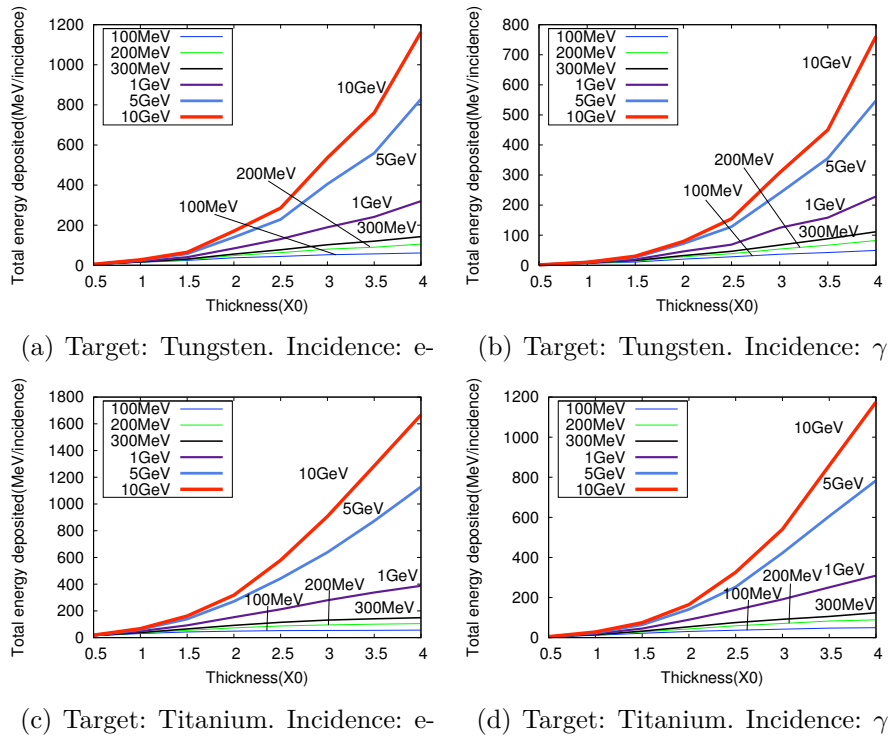
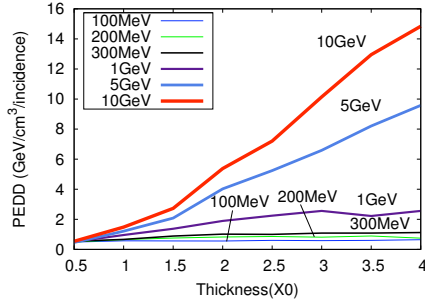
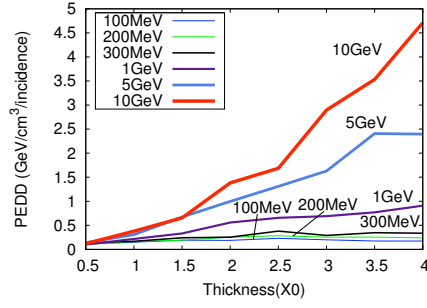


Figure 3.4: Total energy deposition in the target. incident beam size: rms=2.5 mm

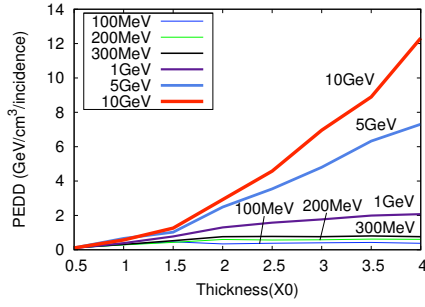
PEDD strongly depends on the incident dimension. Fig. 3.5 shows the PEDD versus the thickness with different incident dimension and target material. Larger beam size leads to a smaller PEDD for the same material and incident particle. With the same material and same size, electron beam causes a larger PEDD than photon beam. If incidence and beam size are the same, the PEDD in tungsten targets is much more than in titanium target.



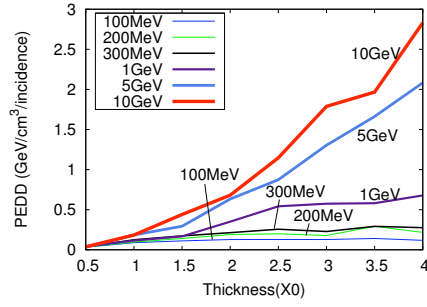
(a) Incidence: e^- . Beam size: 1 mm



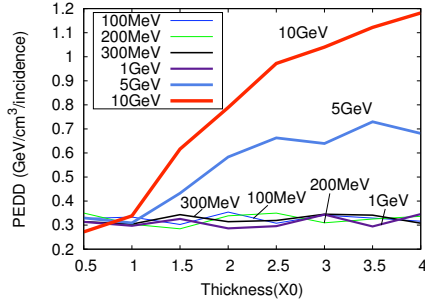
(b) Incidence: e^- . Beam size: 2.5 mm



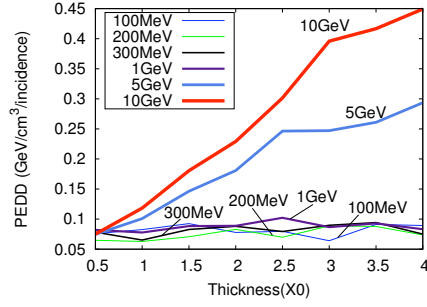
(c) Incidence: γ . Beam size: 1 mm



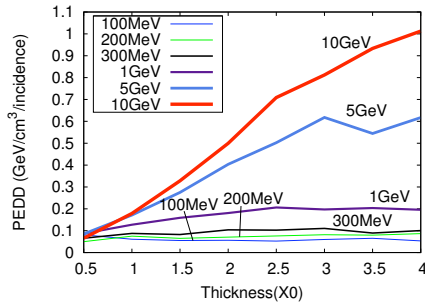
(d) Incidence: γ . Beam size: 2.5 mm



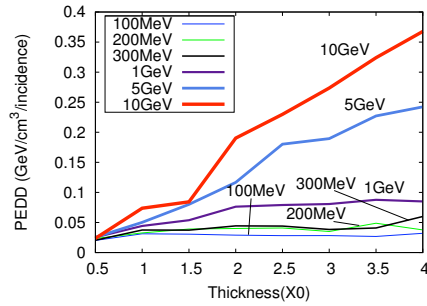
(e) Incidence: e^- . Beam size: 1 mm



(f) Incidence: e^- . Beam size: 2.5 mm



(g) Incidence: γ . Beam size: 1 mm



(h) Incidence: γ . Beam size: 2.5 mm

Figure 3.5: PEDD in target. (a)-(d): Tungsten target. (e)-(h): Titanium target. Abscissa: Target thickness(X_0). Ordinate: PEDD($GeV/cm^3/e^-$)

3.2 The target

3.2.1 The crystal target

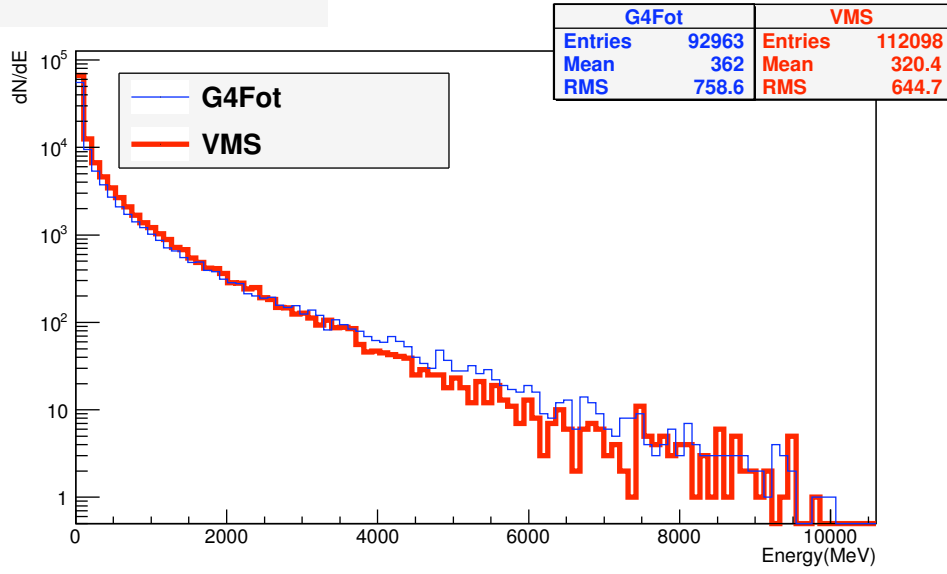
Theoretical studies[34] and simulations[3, 4, 10] of channeling effect in the crystal target have been verified at CERN and KEK[6, 35, 7, 36, 9]. Two programs are developed to simulate the Channeling effect in the crystal target. One is VMS[13] and the other is G4Fot[14] code in Geant4 frame. A good agreement is got between the experiments and the two programs[6, 7]. Fig. 3.6 shows a comparison of photons between G4Fot code and VMS which use 10GeV electron incident on a 1 mm thick tungsten crystal. The crystal axis is $\langle 111 \rangle$. It can be seen that the energy spectrum fits well. Photon yield of VMS is a little larger than G4Fot, 22.4 for VMS and 19.6 for G4Fot. The G4Fot has a larger mean and rms values of energy than VMS. G4Fot produces photons with a little larger angle than VMS, though all of them have an angle less than 1.5 deg. In the simulation both VMS and G4Fot are using point source injection. The beam size will be added before the amorphous target. In this thesis we mainly use VMS output data as the source of photons.

3.2.2 The hybrid target

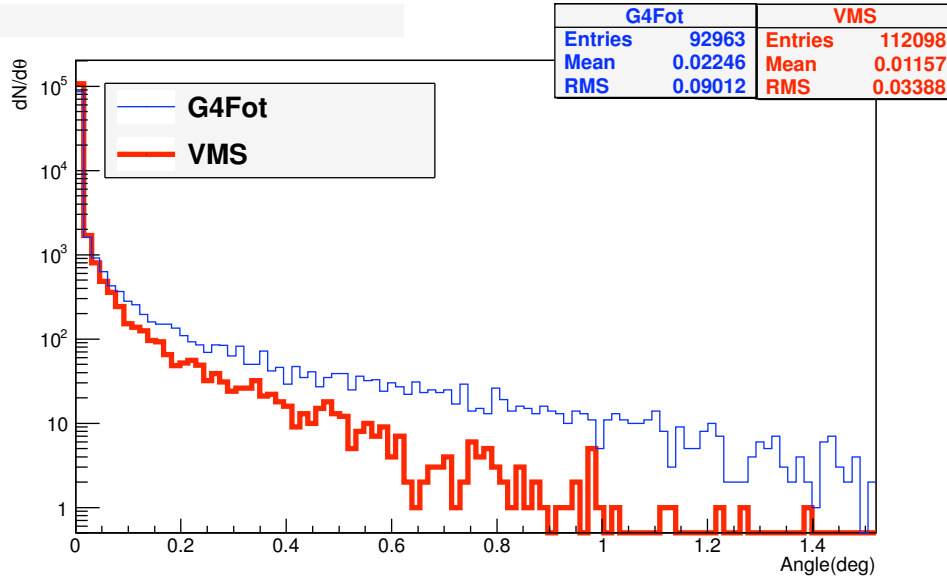
In intense positron source, energy deposition is a key problem. The Ionization process deposit large amount of energy in the e-e+ converter. Generally, there are two aspects: average heating and instantaneous energy deposition. The instantaneous energy deposition will cause temperature gradients and shock waves, consequently mechanical stresses. Moreover, the instantaneous energy deposition may induce shock wave which appears as destruction as in the SLC case. In order to address this issue, a hybrid source is studied.

A hybrid target scheme (see Fig. 3.7)[11] is composed of a crystal target and an amorphous converter. The space between the crystal and amorphous target is used to install a dipole magnet. GeV electron beams oriented to the main axis of the crystal will radiate large number of soft photon(tens of MeV, typically) in crystal target. This is more larger than in amorphous target with the same material and thickness. In order to reduce the total energy deposition and PEDD in the amorphous target, a dipole magnet is used to sweep off the charged particles. Photons mostly impinge on the amorphous target and produce e-e+ pairs.

The space between crystal target and amorphous target will hold a magnet to sweep off the charged particles. Short distance may lead to a high PEDD in the



(a) Energy spectrum



(b) Angle distribution

Figure 3.6: γ spectrum and angle distribution produced by channeling effect carried out by VMS and G4Fot. Incidence: e-. Energy: 10 GeV. Incident number: 5000. Target material: Tungsten. Crystal axis: $\langle 111 \rangle$

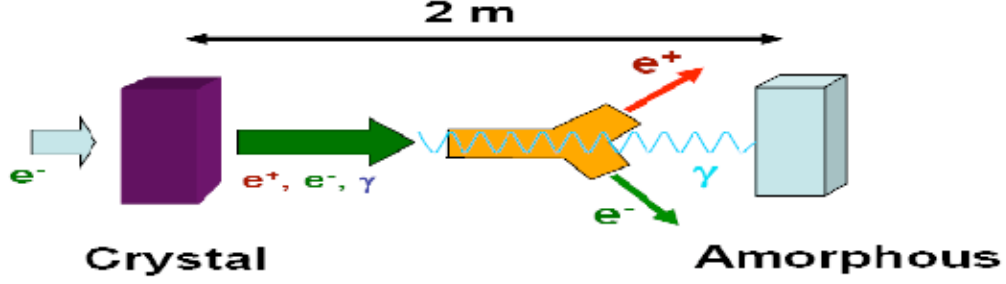


Figure 3.7: Hybrid target scheme

amorphous target. However a long distance will result in loss of some photons which will reduce the positron yield consequently. Table 3.5 shows the influence of distance between the two targets on total positron yield, PEDD and total energy deposited in the amorphous target. We can see that as the distance increases from 0.5 to 4m the total positron yield decreases from 13.33 to 12.82, and the PEDD decreases from 2.38 GeV/cm^3 to 1.63 GeV/cm^3 . In this thesis a 2m long distance will be taken.

Table 3.5: The distance between crystal and amorphous target v.s total e^+ yield, total energy deposition and PEDD. Photon data is from VMS. Incident electron energy: 10GeV. Incident electron lateral size: 2.5mm. Amorphous target material: Tungsten. Thickness: 8mm, transverse size: $2.5 \times 2.5 \text{ cm}^2$

distance (m)	e^+ yield (N^{e^+}/N^{e^-})	Total E deposition (MeV/ e^-)	PEDD ($\text{GeV/cm}^3/e^-$)
0.5	13.33	536.4	2.38
1.0	13.24	526.8	2.26
1.5	13.25	529.0	2.19
2.0	13.17	522.1	1.95
2.5	12.99	519.0	1.89
3.0	12.99	516.6	1.77
3.5	12.96	515.2	1.69
4.0	12.82	510.6	1.63

3.2.3 The choice of the amorphous converter

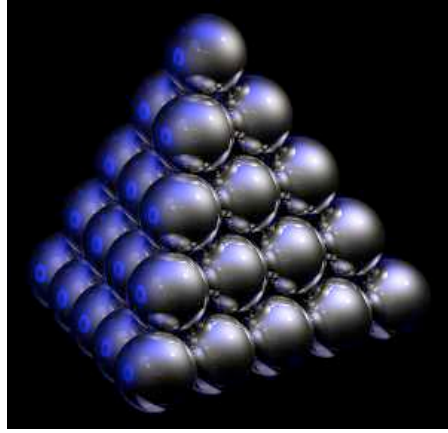
As mentioned before, energy deposition in the target is a key problem which may cause average heating and shock wave. To solve this problem, a granular target is proposed. It was already considered for targets submitted to high intensity proton beams and dedicated to neutrino factories[12]; Where the amorphous target is composed of lots of small spheres held by a container. High speed helium gas flows in the space between the spheres. The smaller sphere radius, the larger ratio of $Surface/Volume = 3/R$, finally the more easily the energy dissipates. Moreover, the smaller radius of spheres can also lead to a smaller characteristic time of the thermal shock waves. For example, for a tungsten sphere with diameter of 2mm we get $0.2\mu s$ of characteristic time if the average sound velocity is 5km/s.

In order to hold spheres in the granular target as much as possible, certain structure of arrangement of spheres in the granular is implemented in Geant4. The hexagonal close packing structure is used because this type of structure has the most efficient way to fill space with spheres(74% of space is occupied). A cell of hexagonal close packing structure contains 8 spheres. A granular target is composed of thousands of cells. Fig. 3.8 shows the structure of hexagonal close packing. (b) - (d) figures are implemented in the Geant4 code as granular target.

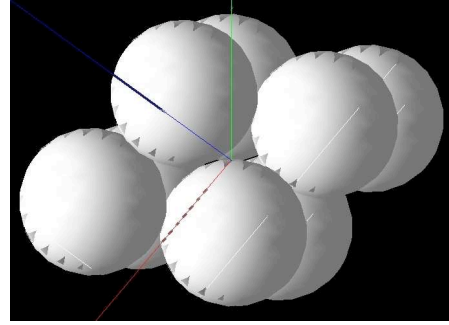
Because the granular target is composed of small spheres, its thickness is discontinuous. We should choose an available thickness to make sure that it produces the similar yield as the compact target. Fig. 3.9 shows a comparison between the compact target and granular target. The markers of granular curves mean where there are available thicknesses.

The breaking target analyze[1] shows that the PEDD tolerant value is $35J/g$, this corresponds to $2.1GeV/cm^3/e^-$ according to time structure proposed by KEK(See chapter 4). According to Fig. 3.9c, the available thickness of compact target is less than 8mm. The available thickness of granular target for sphere radius of 1mm is less than $13.41mm$. The possible thickness is $10.19mm$. The target with this thickness produces a positron yield of 12.45 which is almost the same of the yield of 13.2 produced by a 8mm thick compact target. The total energy deposition in the 10.19mm thick granular target is 446 MeV/e-, less than a 8mm thick compact target case which is 534 MeV/e-. This is good for cooling. In the following simulations, for granular target the sphere radius is 1mm and the granular target thickness is set to be $10.19mm$.

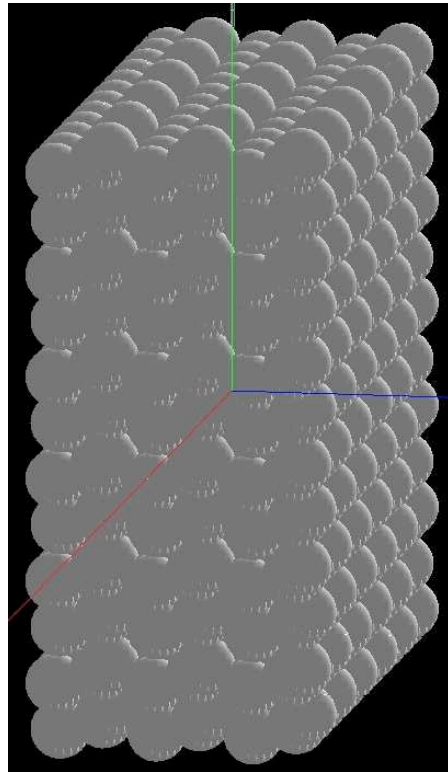
The ILC-VMS condition is defined as following: The incident electron energy is 10GeV. Incident transverse size is 2.5mm. Bunch width is 10ps. Crystal target thickness is 1mm.



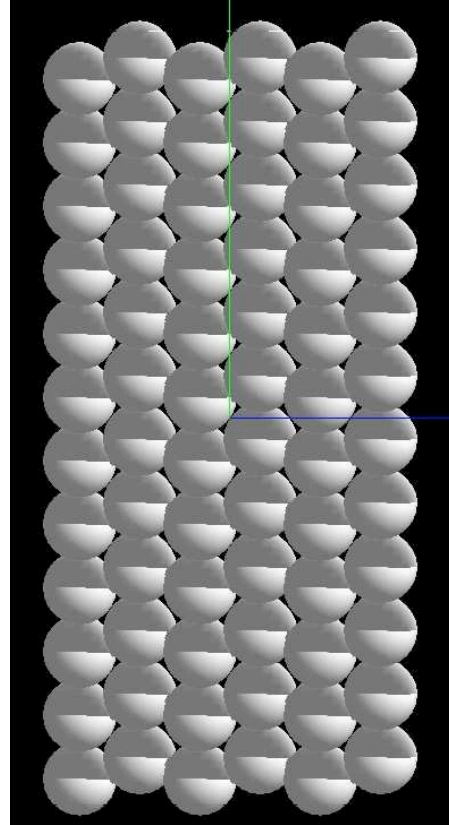
(a) Hexagonal close packed canonball[37]



(b) One cell in Geant4: 3D view

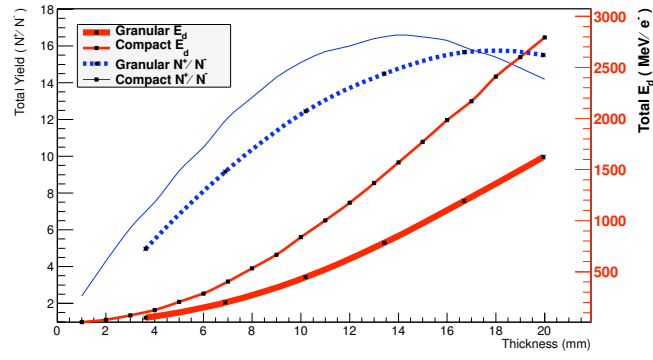


(c) 3 layers in Geant4: 3D view

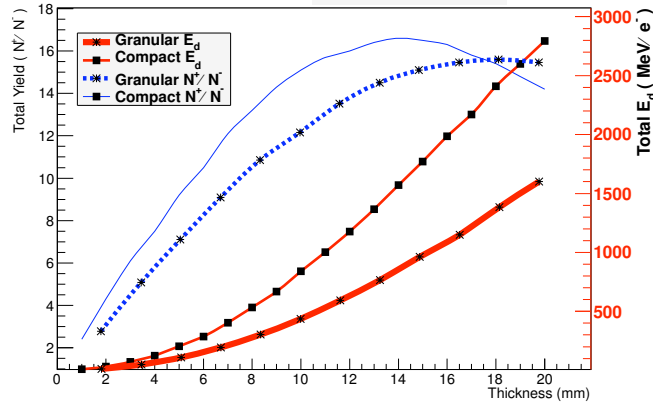


(d) 3 layers in Geant4: X-Z plane view

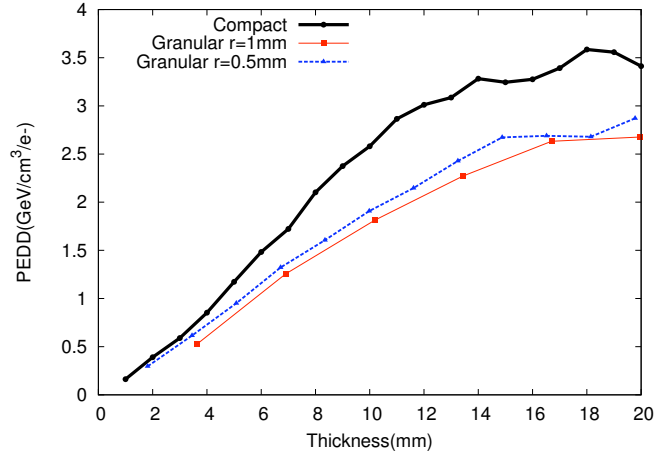
Figure 3.8: Granular target structure



(a) Sphere radius: 1mm



(b) Sphere radius: 0.5mm



(c) PEDD

Figure 3.9: Compact v.s Granular target. Abscissa: Target thickness. For (a) and (b), left Ordinate: Total positron yield; Right Ordinate: Total energy deposition.

3.3 The capture

The positron beam emittance coming out from the converter has small lateral dimensions but large angles. In order to fit the accelerator acceptance, it is needed to transform it into small angles and large lateral dimensions. This section will discuss three types of capture schemes: AMD(Adiabatic Matching Device), QWT(Quarter-Wave Transformer) and Lithium Lens. Some simulations results and features for each kind of capture schemes will be presented.

3.3.1 The AMD

AMD use a solenoid magnet. This system is used at SLAC[38]. The Magnetic field along the Z direction is[39]:

$$B_z = \frac{B_0}{1 + \alpha z} \quad (3.1)$$

where B_0 is the field at the beginning of the AMD. At the exit of the AMD it has $B_z = B_s$, where $z = L$ and L is the length of the AMD. Usually $B_0 = 6Tesla$ and $B_s = 0.5Tesla$ are taken. Fig. 3.10b is the magnetic field evolution. The volume in the hyper-ellipsoid phase space is constant(see Fig. 3.10a). AMD is used to transform the beam from small lateral dimension and large angle into large lateral dimension and small angle.

AMD has a transverse momentum acceptance: $P_{max} = e(B_0 B_s)^{1/2} a$, a large geometrical acceptance: $R_{max} = a(B_s/B_0)^{1/2}$ and a large energy acceptance, where a is the radius of the accelerator section. Another important feature is AMD can cause bunch lengthening due to long enough solenoid(adiabatic tapering). One is low energy particles have a low speed, they need a long time to arrive at the exit of the AMD. The other is large transverse momentum particles move spirally, their trajectories are large and more time are needed to arrive at the exit of AMD.

Figure 3.11 shows the positron beam features before and after crossing the AMD. The simulation program for the crystal is VMS. Incident electron energy is 10 GeV and incident electron number is 5000. The e-e+ pair converter is a 8 mm thick compact tungsten target. Lateral distribution of photon beam is gaussian, $rms = 2.5mm$. Bunch length is also Gaussian distribution and $rms = 10ps$. The length of AMD is 50 cm, with radius=2cm, $B_0 = 6Tesla$, $B_s = 0.5Tesla$. 34.1% of the positrons coming out from the target are captured by AMD. The total yield of positron before and after crossing the AMD is $13.3(N^{e+}/N^{e-})$ and $4.5(N^{e+}/N^{e-})$. The figure shows the beam transverse distribution, transverse momentum distribution, longitudinally distribution, energy spectrum and emittance

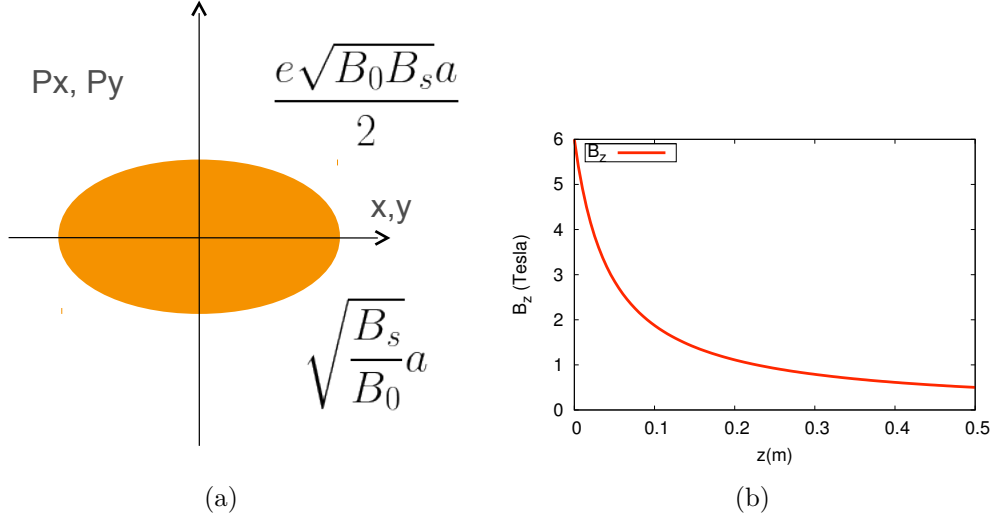


Figure 3.10: Phase hyperellipsoid and Field in AMD. (a): Transverse acceptance. Momenta are canonical: $\mathbf{P} = e\mathbf{A} + m\mathbf{v}$. (b): Magnetic field defined by Eq. (3.1).

before and after the AMD. As mentioned before, after the AMD the lateral dimension of x increases from 3.1 to 8.5 mm, transverse momentum p_x decreases from 7.7 to 3.5 MeV/c, and bunch length increases from 10.6 to 43.4(ps).

Figure 3.13 shows the acceptance of the AMD. Symbol "Target" means total features of positrons at upstream of AMD(Downstream of compact amorphous target). Symbol "AMD" means features of positrons for these captured by the AMD, it shows that the x acceptance range is $[-5mm, 5mm]$, for p_x it is $[-10MeV/c, 10MeV/c]$. Fig. 3.13c shows the emittance for captured positrons and total positrons.

Table 3.6 shows a comparison between different length of AMD: 20cm and 50cm. Two lengths of AMD has the same B_0 and B_s , 6Telsa and 0.5Tesla. From this table we can see that the 20cm long AMD has a larger acceptance than 50cm long AMD. Beam transverse size, transverse momentum, mean energy and yield for the 20cm case are larger than the 50cm case. The bunch lengthening of 20cm long AMD is smaller than 50cm long case.

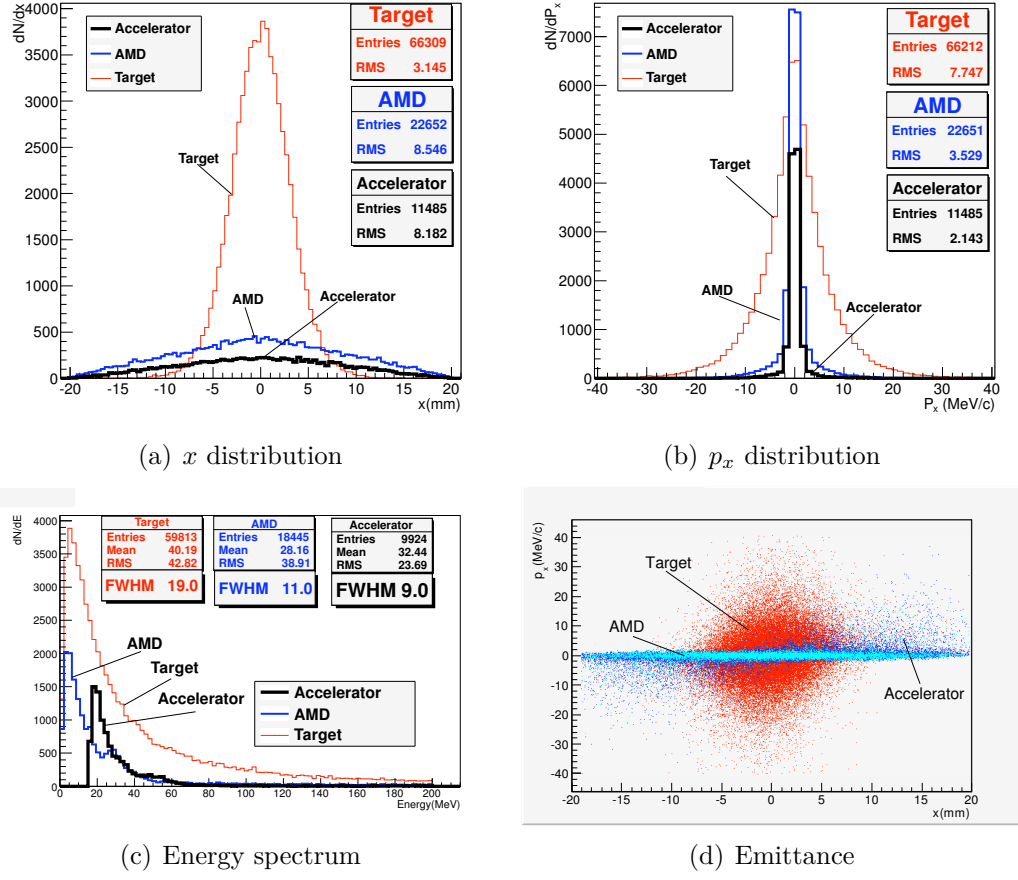
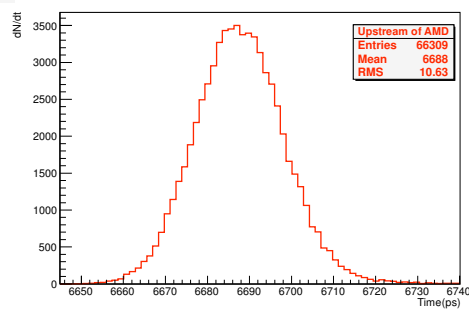


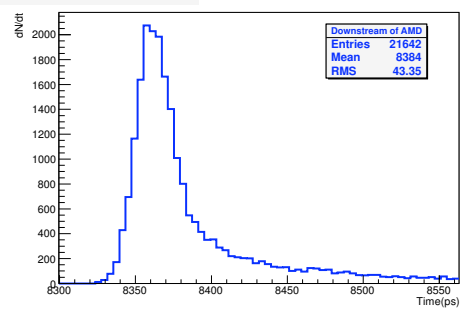
Figure 3.11: Positron beam features.

Table 3.6: Positron beam features after target and different AMD. Incident electron energy: 10GeV. Simulation program for crystal: VMS. Amorphous compact target material: tungsten. Target thickness: 8mm

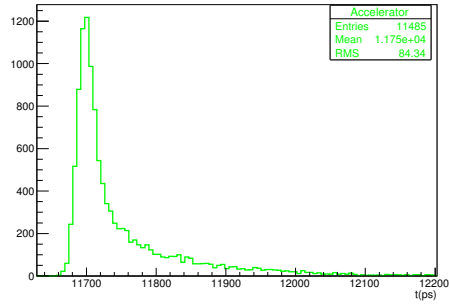
Pos.	rms				mean	fwhm	yield
	x (mm)	p_x (MeV)	t (ps)	E. (MeV)	E. (MeV)	E. (MeV)	$\frac{N^{e+}}{N^{e-}}$
Target	2.97	6.44	10.02	23.97	27.68	20	13.2
AMD 20cm	8.25	4.44	32.45	25.06	21.76	13	5.9
AMD 50cm	8.56	3.11	43.14	17.83	17.62	11	4.6



(a)

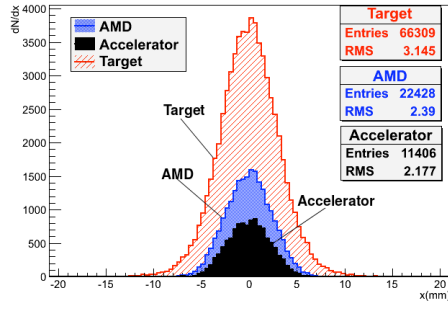


(b)

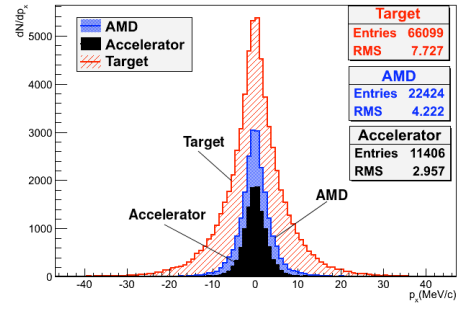


(c)

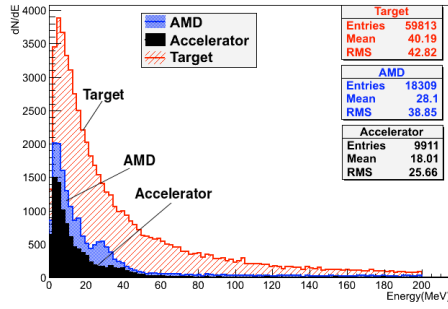
Figure 3.12: Time structure. (a): Exit of the target. (b): Exit of the AMD. (c): Exit of the 1m long accelerator.



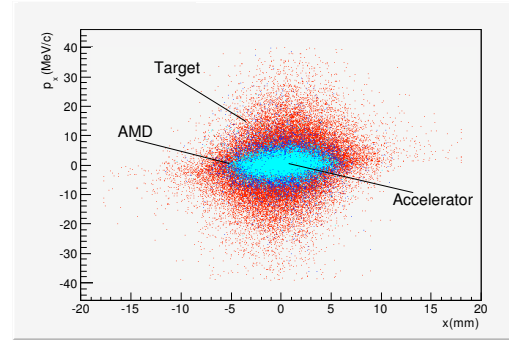
(a) Acceptance of x distribution



(b) Acceptance of p_x distribution



(c) Acceptance of energy spectrum



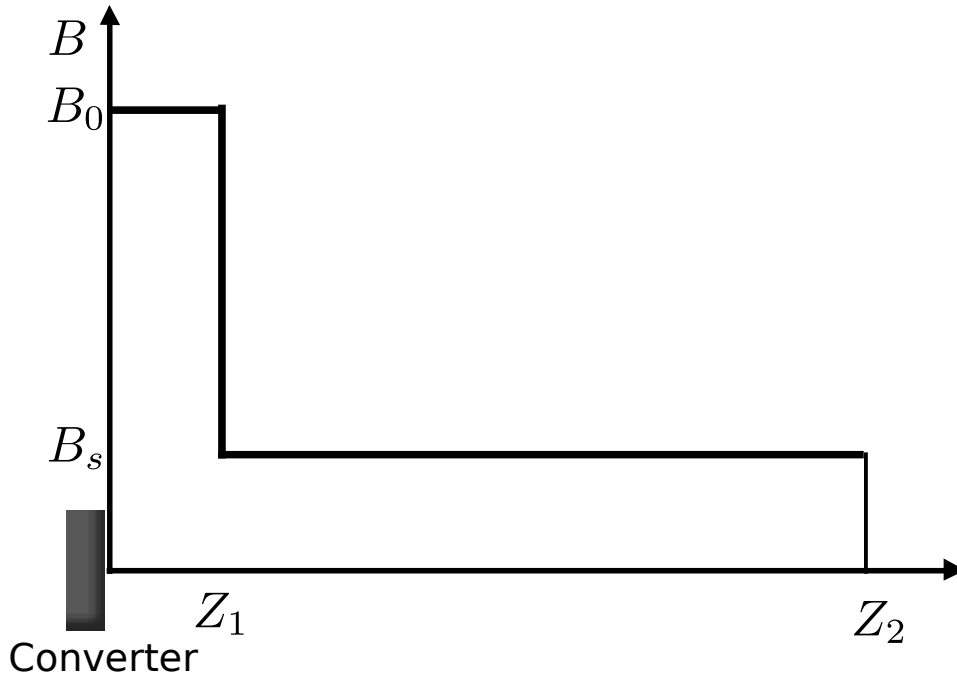
(d) Acceptance of $p_x - x$ phase space

Figure 3.13: Acceptance of AMD and 1m accelerator. Symbol "Target": Exit of the target. Symbol "AMD": Captured positrons by AMD. Symbol "Accelerator": Captured positrons by AMD and Accelerator.

3.3.2 The quarter-wave transformer (QWT)

Quarter-wave transformer is made of a short solenoid with a high magnetic field and a long solenoid with lower magnetic field extending over several accelerator sections[40]. The field profile of QWT is presented in Fig. 3.14.

QWT has a momentum acceptance: $(eB_0a/2)(1+B_s/B_0)$, larger compared with AMD with the same field parameters. It has a geometrical acceptance: $a(B_s/B_0)$. The energy acceptance of QWT is narrow. Due to short solenoid length, the bunch lengthening is restricted.



(a)

Figure 3.14: Field profile of the quarter-wave transformer.

Figure 3.15 shows the phase acceptance and captured energy spectrum. Fig. 3.15b shows the energy acceptance profile calculated by theoretical and Monte-Carlo simulation. It is ILC case, where the hybrid target is composed of a 1mm tungsten crystal and a 8mm amorphous compact tungsten target. The crystal target delivers an incident photon beam to the amorphous tungsten target(see Sec. 3.2 for the description of the hybrid target). The incident electron beam energy is 10 GeV and the lateral size is 2.5 mm. The photon source is from VMS

data. The QWT length is 8cm, $B_0 = 6\text{Tesla}$, $B_s = 0.5\text{Tesla}$. The length of accelerator is 1m, electric field is 15MV/m and magnetic field is 0.5Tesla . The results fit well.

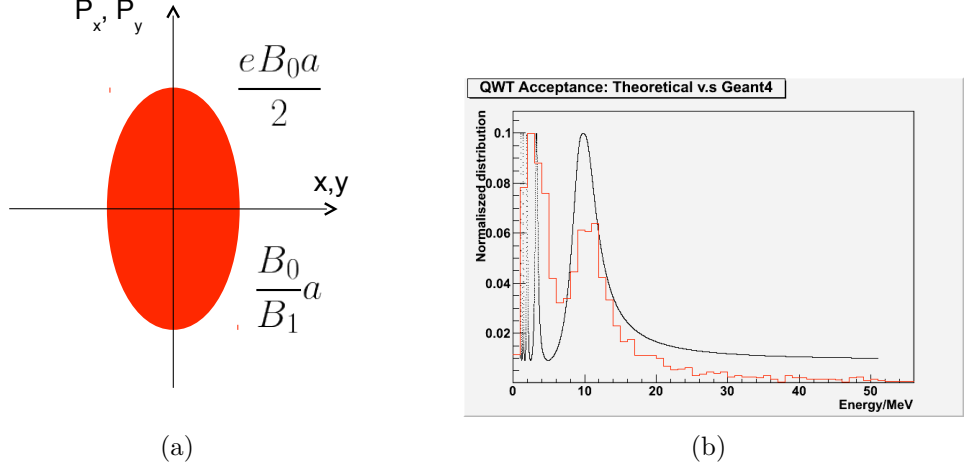
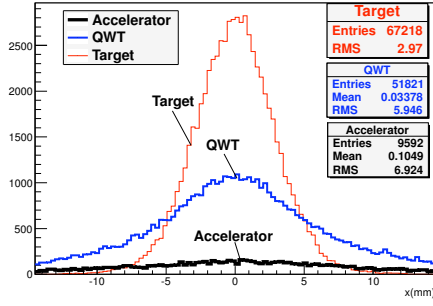


Figure 3.15: QWT acceptance phase and energy acceptance spectrum. (a): Transverse acceptance. Momenta are canonical: $\mathbf{P} = e\mathbf{A} + m\mathbf{v}$. (b): Accepted energy spectrum. ILC case. QWT length 8cm, $B_0 = 6T$, $B_s = 0.5T$. Accelerator length: 1m, magnetic field: 0.5T, electric field: 15MV/m .

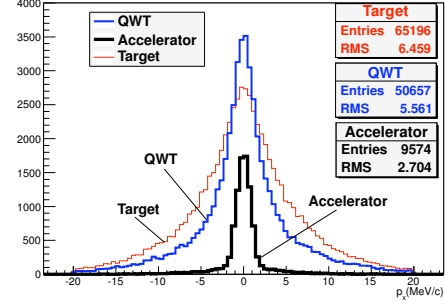
Figure 3.16 shows some features of QWT. The conditions for the hybrid target are the same as above. For QWT the length is 8 cm and the magnetic field is 2Tesla . The accelerator length is 1m, magnetic field is 0.5Tesla and the electric field is 15MV/m . It shows that from the exit of the target to the exit of the accelerator, the lateral size increases from 2.97mm to 6.92mm , the transverse momentum decreases from $6.46\text{MeV}/c$ to $2.70\text{MeV}/c$. The yield is 10.36 at the exit of the QWT and 1.92 at the exit of the accelerator which is smaller than with the 50cm long AMD where $B_0 = 6\text{Tesla}$.

Figure 3.17 shows the time structures of positron beam at the exit of the target, QWT and accelerator. The conditions are the same as above. Initial bunch length of electron is set to be 10ps. It shows that the bunch lengthening due to the magnetic field is restricted compared with the 50cm long AMD where $B_0 = 6\text{Tesla}$.

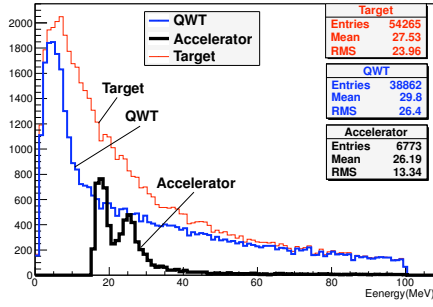
Figure 3.18 shows the acceptance features of the QWT and the accelerator. The conditions are the same as above. Symbol "Target" means the features of all positrons at the exit of the target, which are used as a comparison. Symbol



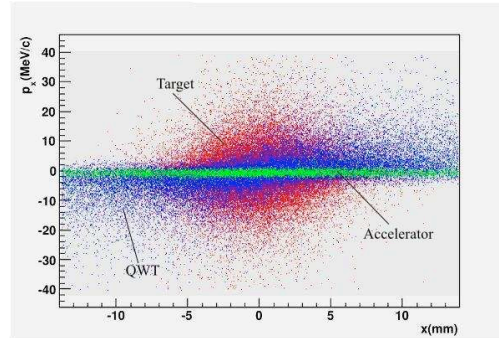
(a) x distribution



(b) p_x distribution

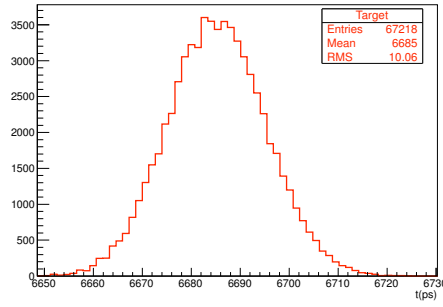


(c) Energy spectrum

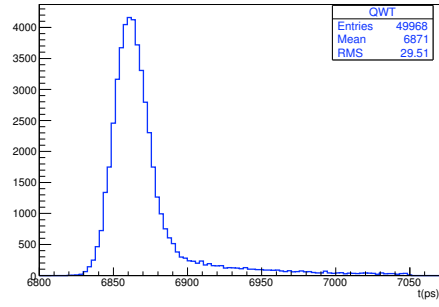


(d) Emittance

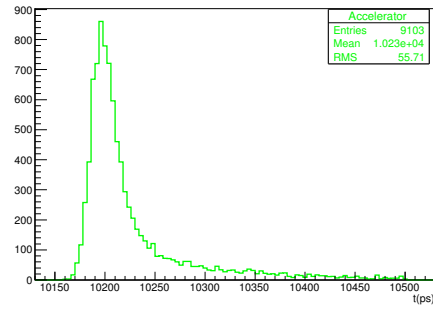
Figure 3.16: Positron beam features.



(a)



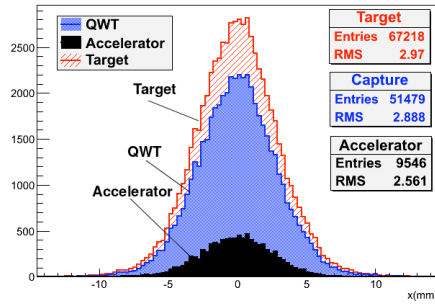
(b)



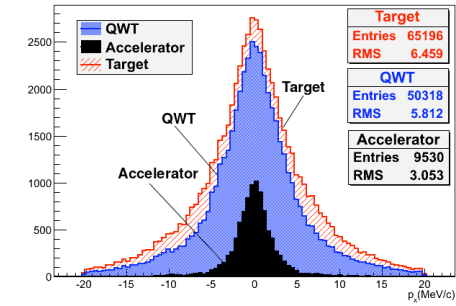
(c)

Figure 3.17: Time structure. (a): Exit of the target. (b): Exit of the QWT. (c): Exit of the accelerator.

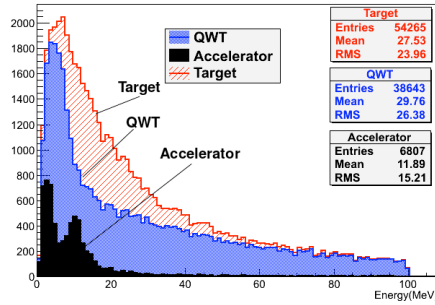
”QWT” means features of positron captured by QWT and symbol ”Accelerator” means positrons captured by both the QWT and the accelerator. It shows for the geometric acceptance x the QWT is very large however decreases to range $[-5\text{mm}, 5\text{mm}]$ at the exit of the accelerator. For momentum component p_x the acceptance is very large at the exit of the QWT though decreases to range $[-5\text{MeV}/c, 5\text{MeV}/c]$ at the exit of the accelerator. The energy acceptance at the exit of the accelerator is less than about 20 MeV and has two peaks. They correspond to different turns of positrons in the phase space. The $p_x \sim x$ phase space of the acceptance for the QWT and accelerator is a hyperellipsoid, see green area in Fig. 3.18d. The range of x and p_x are $[-5\text{mm}, 5\text{mm}]$ and $[-5\text{MeV}/c, 5\text{MeV}/c]$.



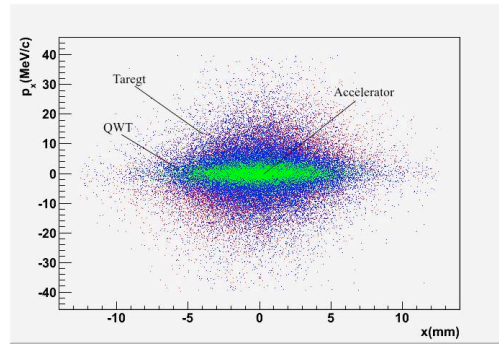
(a) Acceptance of x distribution



(b) Acceptance of p_x distribution



(c) Acceptance of energy spectrum



(d) Acceptance of $p_x - x$ phase space

Figure 3.18: Acceptance of QWT and 1m accelerator. Symbol ”Target”: Exit of the target and used as a comparison(is not acceptance parameters). Symbol ”QWT”: Captured positrons by QWT. Symbol ”Accelerator”: Captured positrons by QWT and Accelerator.

3.3.3 The Lithium lens

Lithium lens[41] is made of metal lithium, and the azimuthal magnetic field is created by a longitudinal current circulating with the same direction of the particles. It can provide a strong focusing for one type of charged particle and defocusing for its anti-particle. This can make beam control easier in the following part of the accelerator. The magnetic field can be written as:

$$B = \begin{cases} \frac{\mu_0 I}{2\pi R_0^2} r & \text{if } r < R_0 \\ \frac{\mu_0 I}{2\pi r} & \text{if } r > R_0 \end{cases}$$

where R_0 is the radius of the lithium wire and I is the circulating current. A sketch of the magnetic field is given in Fig. 3.19b.

Two kinds of devices have been elaborated by using this principle: lithium and plasma lens. Here we mainly talk about lithium lens. Fig. 3.19a shows a sketch of Lithium lens. The lens is made of a cylindrical lithium conductor fed with an unipolar current pulse. The pulsed current is up to $100kA$ to induce magnetic field of several Tesla. A distance between lens and target is used as focus length.

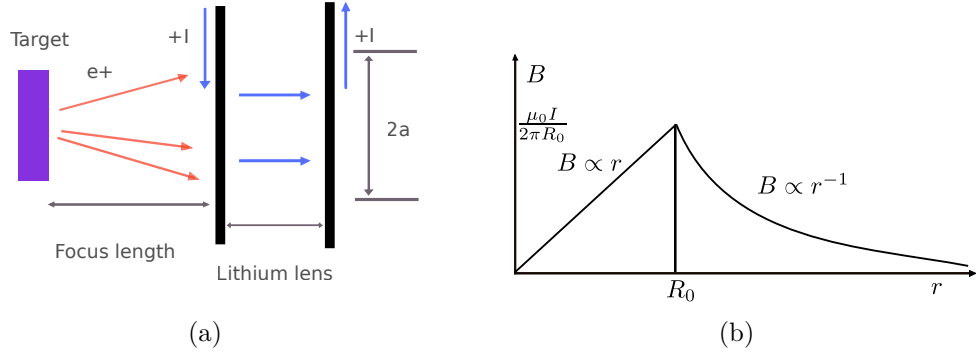


Figure 3.19: Lithium lens structure and field.

Figure 3.20 shows the Mont-Carlo results of the Lithium lens under the ILC case. The simulations were made without windows. The electron beam energy is 10 GeV and the lateral size is 2.5mm. The target thickness is 8mm and material is tungsten. For the Lithium lens the focus length is 1cm, length of lithium is 2cm and radius of lithium is 1cm. The current in the lithium is $82.5kA$. The lithium lens is followed by an accelerator, whose magnetic field is 0.5 Tesla and the electric field is 15MV/m. From the figures it shows that the lateral x size increases from $2.94mm$ at the exit of the target to $7.03mm$, at the exit of the accelerator. The

p_x decreases from $6.4\text{MeV}/c$ to $3.5\text{MeV}/c$. The rms of energy decreases from 24.2MeV to 14.5 . The total yield of positrons at the exit of the accelerator is 1.38, less than the AMD and the QWT. Figure 3.21 shows the time structure of positron

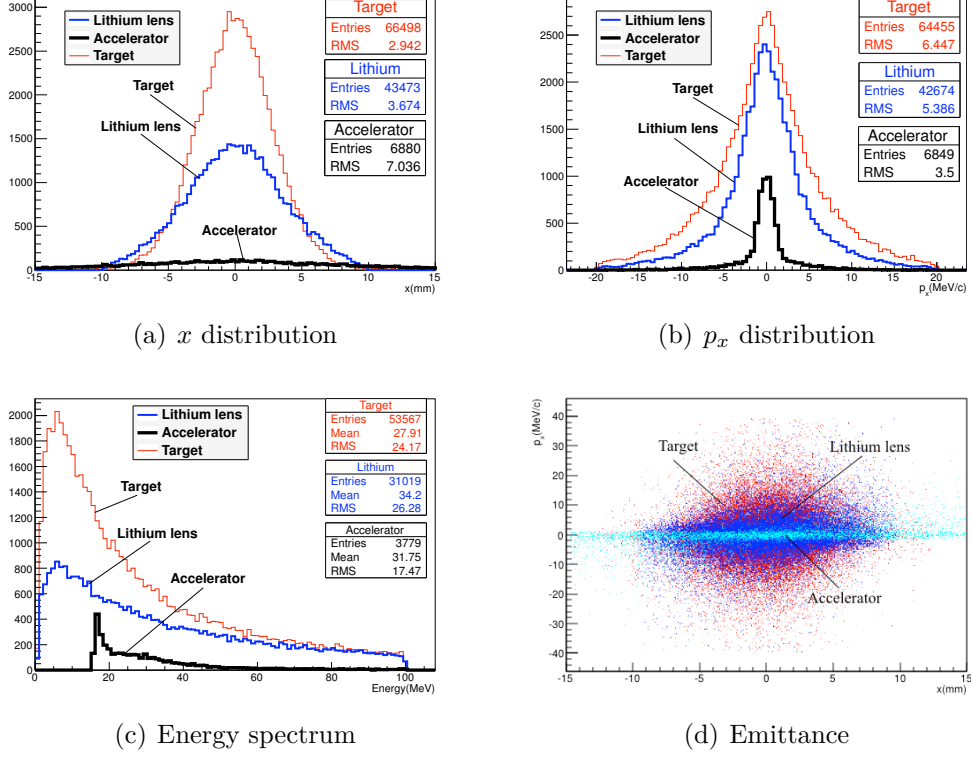


Figure 3.20: Positron beam features.

beam at the exit of the target, lithium lens and accelerator. The conditions are the same as above. The initial time structure of the electron beam is gaussian and rms is 10ps. Compared with the AMD and the QWT, the lithium lens has a good time structure and the rms at the exit of the accelerator is 28.5ps.

Figure 3.23 shows the trajectories of positrons and electrons in the Lithium lens and 1m long accelerator. It clearly shows that the Lithium lens focuses positrons and defocuses electrons.

The acceptance of the Lithium lens is smaller than the AMD and the QWT. Fig. 3.22 shows the acceptance parameters. The conditions are the same as above. Symbol "Target" means parameters at the exit of the target and the features are used as comparison. Symbol "Lithium lens" means positrons that captured by lithium lens and symbol "Accelerator" means captured by lithium lens and accelerator. Energy acceptance is narrow, also for lateral dimension and momentum

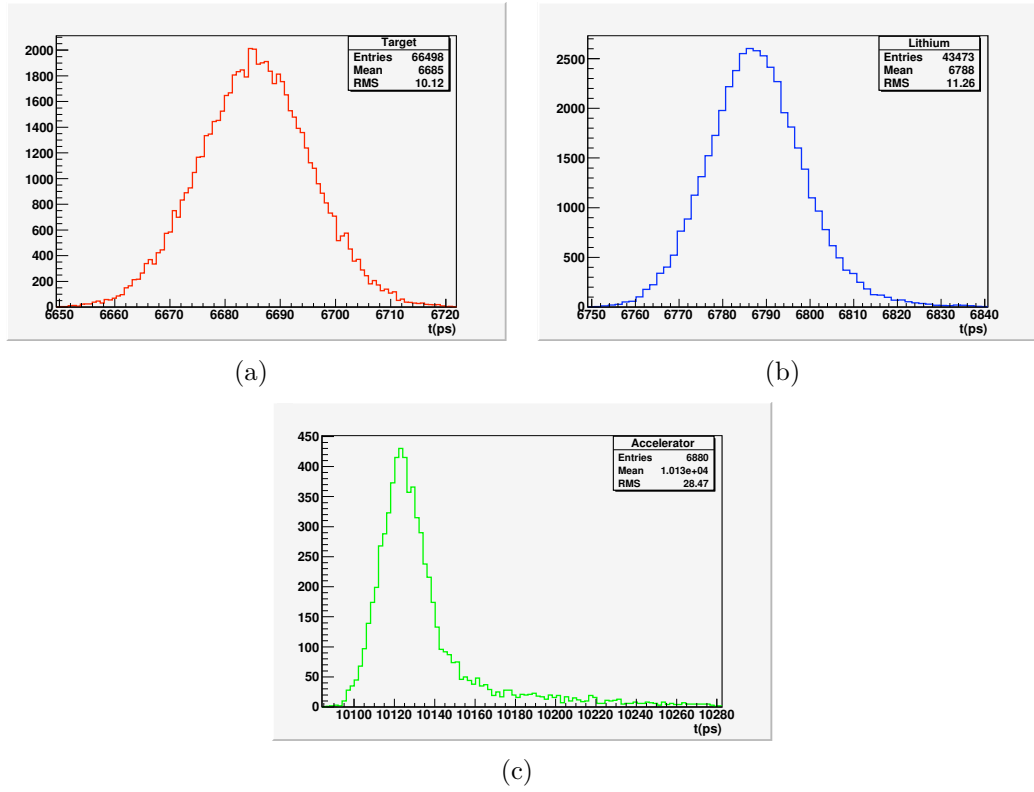


Figure 3.21: Time structure. (a): Exit of the target. (b): Exit of the Lithium lens. (c): Exit of the 1m long accelerator.

acceptance. Acceptance hyperellipsoid in phase space is small and only 10% of positrons are captured by Lithium lens and accelerator.

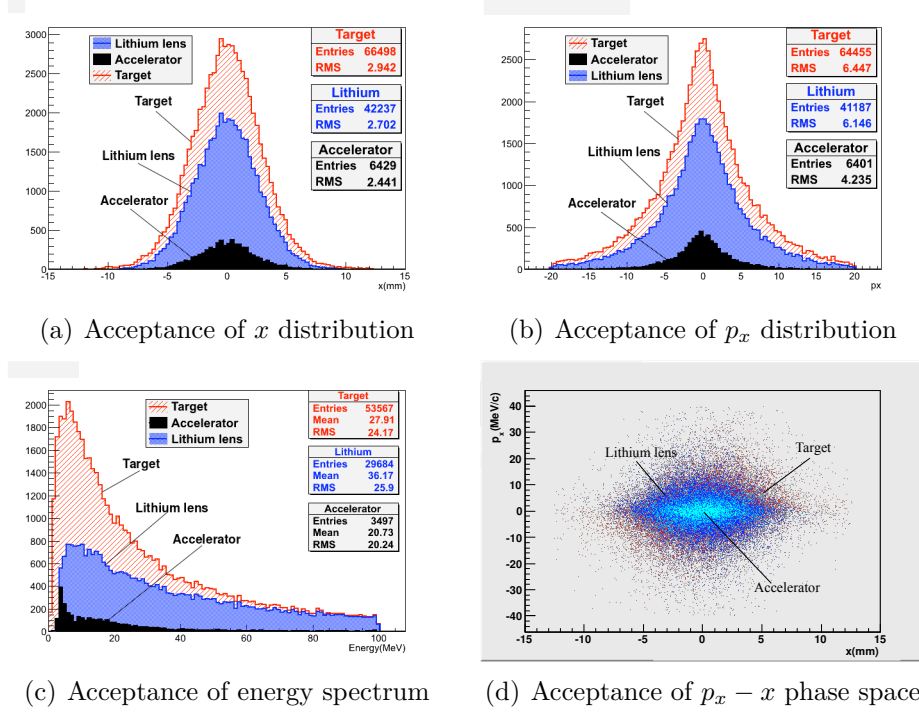


Figure 3.22: Acceptance of Lithium lens and 1m accelerator. Symbol "Target": Exit of the target and used as comparison(is not acceptance). Symbol "Lithium lens": Captured positrons by Lithium lens. Symbol "Accelerator": Captured positrons by Lithium lens and Accelerator.

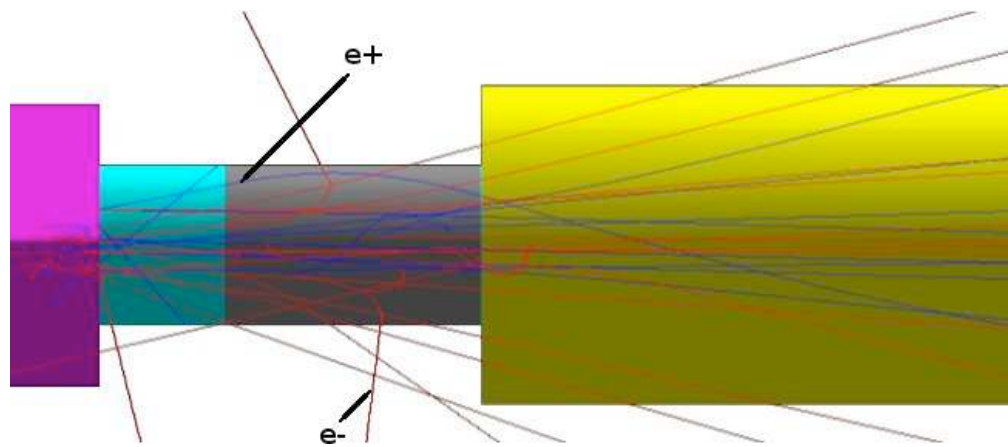


Figure 3.23: Trajectories of positrons and electrons in Lithium lens and $1m$ long accelerator.

Chapter 4

Heating and Cooling

This chapter will discuss heating and cooling for e-e+ pair converter. First we will talk about the beam structure of the incident electrons. Then some basic theory will be presented about heating and cooling, concerning the shock wave problem, energy deposition and thermal dissipation for helium gas cooling in the granular target. After that we will discuss the total energy deposition in the granular target and detailed calculation for heating and helium gas cooling according to the incident beam structure. The last section is about the PEDD. We will talk about the thermal shock wave, temperature rise and peak temperature in the granular target.

4.1 General acknowledgement

The heating is a key problem in the positron source target. There are two aspects about the heating: the total energy deposition and instantaneous energy deposition density. The total energy deposition may melt the target and the instantaneous energy deposition will lead to temperature gradient which may cause thermal stresses and shock wave. It will destruct the target eventually.

Energy deposition and temperature are associated with the e- beam structure. There are two proposed schemes for electron beam structure, LAL scheme and KEK scheme[42]. Fig. 4.1 shows the KEK scheme. A bunch is composed of electrons of $2 \cdot 10^{10}$ and its width is $10ps$. 100 bunches compose a minitrain of $0.6\mu s$, the separation between two bunches is $6.15ns$. 13 minitrains form a macropulse of $40ms$, the separation between two minitrains is $3.3ms$. There are 5 macropulses per second (5 Hz) and the separation between two macropulse is $200ms$. According

to this scheme, there are 2×10^{12} electrons in a minitrain, 2.6×10^{13} in a macropulse and 1.3×10^{14} in a second.

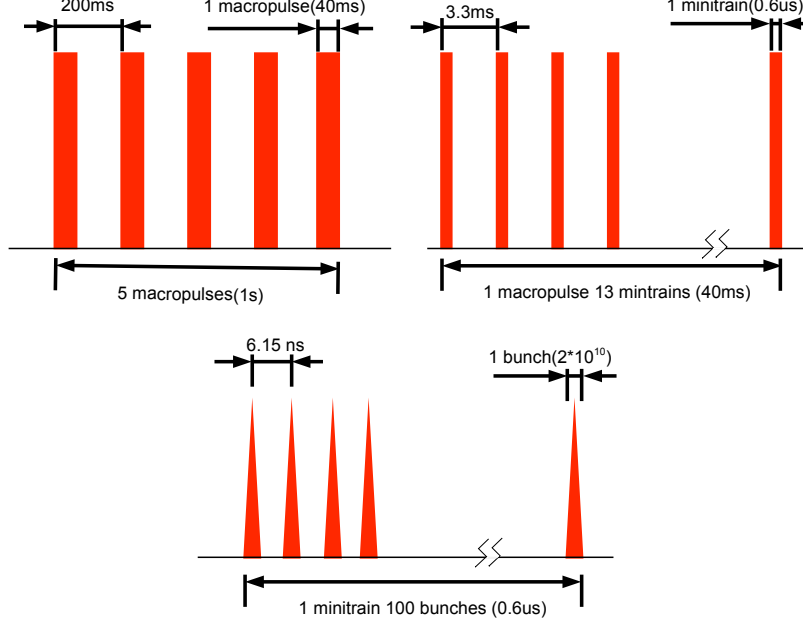


Figure 4.1: ILC beam structure. KEK scheme[42]

To cool the granular target, helium gas is considered. It flows in the space between the spheres and takes away the power. For helium gas cooling we just consider thermal convection while neglecting thermal conduction and thermal radiation, since they are negligible compared with thermal convection for high speed fluid.

The thermal convection coefficient is defined by[43]

$$\alpha = q/F * T_{\Delta} \quad (4.1)$$

where the unit of α is $(W * m^{-2} * K^{-1})$, q is energy flow J/s , F is surface area and T_{Δ} is temperature difference between fluid and solid.

Try to cool with helium, assuming a heat transfer coefficient of $\alpha = 10^5 W * m^{-2} * K^{-1}$. This is rather high, but reachable[44].

For the thermal convection, the temperature evolution is defined by[44]

$$T(t) = T(0) * e^{-t/t_0}. \quad (4.2)$$

For single energy deposition, it can be written by

$$T(t) = (T_0 + \Delta T) * e^{-t/t_0} \quad (4.3)$$

And for periodical minitrain energy deposition, in steady state it is

$$(T_0 + \Delta T) * e^{-\Delta t/t_0} = T_0 \quad (4.4)$$

where ΔT is temperature rise in one minitrain, T_0 is temperature before a minitrain and Δt is time interval between two minitrains.

t_0 is time constant when the temperature is $1/e$ of initial value. It is defined by the[44]

$$t_0 = \frac{C_v * m}{\alpha * F} \quad (4.5)$$

For a sphere it can be written as

$$t_0 = \frac{C_v * \rho * r}{3 * \alpha} \quad (4.6)$$

where the factors are defined as follows:

C_v : Specific heat ($J * kg^{-1} * K^{-1}$)

m : Solid mass (kg)

α : See Eq. (4.1)

F : Surface area (m^2)

ρ : Solid density ($kg * m^{-3}$)

r : Sphere radius (m)

From Eq.(4.6) it shows that small r and high α reduce t_0 , which can accelerate energy dissipation.

4.2 Total energy deposition

Figure 4.2 shows the total energy deposition in the compact and granular target. The $8mm$ thick compact target has a total yield of $13.2e+/e-$ just at the exit of the converter, the total energy deposition is $534MeV/e-$. For granular target the

thickness is discontinue. According to the disscusion in chapter 3, for the radius of $1mm$ case the two possible granular thickness are $10.2mm$ and $13.43mm$. The latter has a more higher energy deposition of $785MeV/e-$ which is bad for cooling. Here we focus on $10.2mm$ case, the total energy deposition is $446MeV/e-$. For the radius of $0.5mm$ the best approximation thickness is $11.6mm$, the total yield is $13.5e+/e-$ and the total energy deposition is $593MeV/e-$. The total energy deposition in the granular target only depends on the thickness because the averaged density of granular target is the same.

Table 4.1: Possibility of thickness for granular target, radius= $1mm$.

Layer	Thickness (mm)	Yield (e+/e-)	Total energy deposition (MeV/e-)	PEDD (GeV/cm ³ /e-)
1	3.62	4.97	50	0.5229
2	6.9	9.17	200	1.2551
3	10.19	12.45	446	1.8139
4	13.43	14.6	785	2.2706
5	16.7	15.66	1194	2.6327
6	19.96	15.5	1624	2.6766

Table 4.2: Possibility of thickness for granular target, radius= $0.5mm$.

Layer	Thickness (mm)	Yield (e+/e-)	Total energy deposition (MeV/e-)	PEDD (GeV/cm ³ /e-)
1	1.8165	2.7604	12.4869	0.2965
2	3.44949	5.0408	49.2887	0.6160
3	5.08248	7.0838	108.239	0.9514
4	6.71548	9.0594	194.981	1.3224
5	8.34847	10.8092	303.187	1.6061
6	9.98146	12.1586	436.254	1.9081
7	11.6145	13.4854	592.664	2.1464
8	13.2474	14.4714	766.349	2.4281
9	14.8804	15.0688	961.19	2.6723
10	16.5134	15.4524	1149.66	2.6891
11	18.1464	15.5858	1384.79	2.6793
12	19.7794	15.4134	1600.07	2.8707

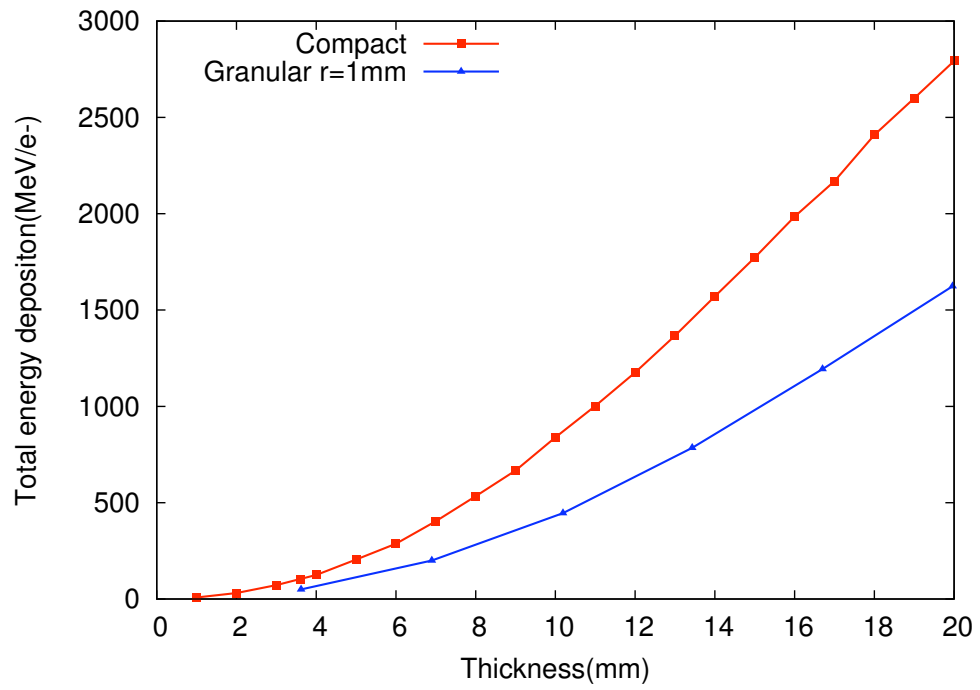


Figure 4.2: Total energy deposition in compact and granular targets. ILC-VMS case. Granular sphere radius: 1mm

Table 4.3 and 4.4 show the detailed description for two cases of granular target, sphere radius of $1mm$, 3 layers and sphere radius of $0.5mm$, 7 layers.

Table 4.3: Description for granular target, radius= $1mm$, layers= 3 . Each cell contains 8 spheres.

X of target(mm)	24
Y of target(mm)	21.1
Z of target(mm)	10.2
Z axis Cell width(mm)	3.26599
Number of X cell	6
Number of Y cell	6
Number of Z cell	3
Total Cells	=108
Total spheres	$108*8=864$
Volume per sphere(mm^3)	4.19
Mass per sphere(g)	0.081
Total energy deposition($MeV/e-$)	446
PEDD($GeV/cm^3/e-$)	1.8

Assuming a heat transfer convection coefficient of 10^5 and a mass flow of $30g/s$, the power deposited in the granular target and the temperature rise in helium are summarized in Table 4.5, 4.6. Two sizes of sphere radius are considered: $1mm$ and $0.5mm$. The power deposited and temperature rise are averaged over one second and over one macropulse. For our choice: granular target with sphere radius $1mm$ and 3 layers, the temperature rise over one second is $59.62K$ and over one macropulse it is $298.1K$. The temperature rise is high which reduces the target life time. Moreover, it requires very high speed helium gas, which is very hard. The conclusion is a stationary target is not workable. A moving target (rotating wheel or pendulum) should be considered.

4.3 PEDD

High intensity incidences pulses deposit a large amount of energy in the targets provoking temperature rises. The target material expands but due to the mass inertia, there will be a delay leading to pressure waves to cross the material which provokes stresses. These waves move with the sound velocity:

$$\nu = (E/\rho)^{1/2} \quad (4.7)$$

Table 4.4: Description for granular target, radius=0.5mm, layers=7

X of target(mm)	20
Y of target(mm)	17.5
Z of target(mm)	11.6
Z axis Cell width(mm)	1.63299
Number of X cell	10
Number of Y cell	10
Number of Z cell	7
Total Cells	700
Total spheres	700*8=5600
Volume per sphere(mm^3)	0.52
Mass per sphere(g)	0.01
Total energy deposition($MeV/e-$)	593
PEDD($GeV/cm^3/e-$)	2.14

Table 4.5: Power in the granular target and temperature rise in the Helium. Granular sphere radius: 1mm, 3 layers in z direction.

		Averaged over one second		Averaged over one macropulse (40ms)	
Layer	Thickness (mm)	Power (kW)	Temperature (K)	Power (kW)	Temperature (K)
1	3.62	1.0413	6.68	5.20	33.42
2	6.9	4.1652	26.73	20.82	133.68
3	10.19	9.2884	59.62	46.44	298.10
4	13.43	16.3484	104.93	81.74	524.69
5	16.7	24.8662	159.61	124.33	798.06
6	19.96	33.8214	217.09	169.10	1085.48

Table 4.6: Power in the granular target and temperature rise in the Helium. Granular sphere radius: 0.5mm, 7 layers in z direction.

		Averaged over one second		Averaged over one macropulse (40ms)	
Layer	Thickness (mm)	Power (kW)	Temperature (K)	Power (kW)	Temperature (K)
1	1.81	0.26	1.66	1.30	8.34
2	3.44	1.02	6.58	5.13	32.94
3	5.08	2.25	14.46	11.27	72.34
4	6.71	4.06	26.06	20.30	130.32
5	8.34	6.31	40.53	31.57	202.65
6	9.98	9.08	58.31	45.42	291.59
7	11.61	12.34	79.22	61.71	396.13
8	13.24	15.96	102.44	79.79	512.22
9	14.88	20.01	128.49	100.08	642.45
10	16.51	23.94	153.68	119.71	768.43
11	18.14	28.83	185.11	144.19	925.59
12	19.77	33.32	213.89	166.61	1069.49

where E is the Young modulus and ρ is the density. The sound speed for tungsten at room temperature is $\nu \sim 4.6 * 10^3 m/s$.

The time needed for the wave to travel from the outer surface of sphere to the center is $\tau_s = d/\nu$. If the pulse width $\tau_p > \tau_s$, small amount of energy is going into the target over τ_s and the shock wave is limited.

For granular target with sphere radius of $1mm$, the sphere size is less than the transverse dimension of incident beam which is $2.5mm$. Only small and essentially linear temperature gradients will be created in individual sphere. This means spheres can expand relatively free and will lead to negligible thermal stresses. The time for sound traveling across the sphere is $\tau_s = 0.22\mu s$ which is smaller compared with minitrain width $0.6\mu s$. The shock will be limited.

Figure 4.3 shows the PEDD in the granular target versus target thickness. For granular target the PEDD for the sphere radius of $1mm$ case is smaller than for sphere radius of $0.5mm$ case, for the same target thickness. Because the cell volume used to count EDD(Energy Deposition Density) is larger for $1mm$ case than $0.5mm$ case.

Figure 4.4 shows the energy deposition density in a granular target whose sphere radius is $1mm$ and the target thickness is $10.2mm$. (a) is x-z plane view, z is the incident direction and $y \sim 0$ is at center of incident y-dimension. (b) is x-y plane view and z is at the end of the target. The figure shows that the PEDD is about $1.8 GeV/cm^3/e-$. Detailed PEDD for various thickness are represented in Table 4.1 and 4.2.

For thermal dissipation, with Eq. (4.6) the time constant is defined as the temperature decreases to $1/e$ of initial value. For sphere radius of $1mm$ this value is $8.3ms$ and $4.1ms$ for sphere radius of $0.5mm$, which can only be reached with very high helium flux($\alpha = 10^5$).

Using the time constant we can calculate the lowest and highest temperature now. Table 4.8 and 4.7 show the PEDD per minitrain, temperature rise in one minitrain, lowest temperature and highest temperature in the hottest sphere in the granular target. Fig. 4.5 shows the temperature rise versus time in one macropulse in the hottest part of the granular target with sphere radius of $1mm$ and 3 layers. The lowest temperature is just before the first minitrain and the highest temperature is just after a minitrain when it arrives at a stable state. For our choice of VMS-ILC: granular with 3 layers and sphere radius of $1mm$, the temperature rise in hottest sphere per minitrain is $232K$. The highest temperature in the hottest sphere is $708K$. The stationary target is not workable.

If $\tau_p > \tau_s \sim r/\nu$ where r is sphere radius. The thermal stress provoked by

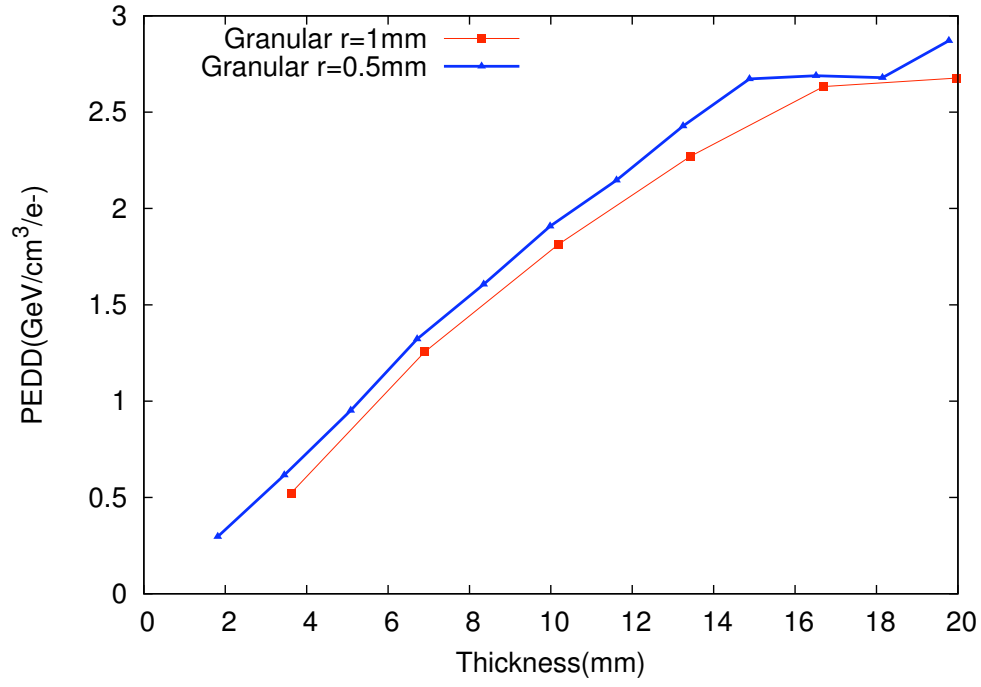


Figure 4.3: PEDD comparison between granular target. ILC-VMS case. Granular sphere radius: 1mm and 0.5mm. Cell volume of 1mm: $3\pi/4 \text{ mm}^3$. Cell volume of 0.5mm: $3\pi/32 \text{ mm}^3$

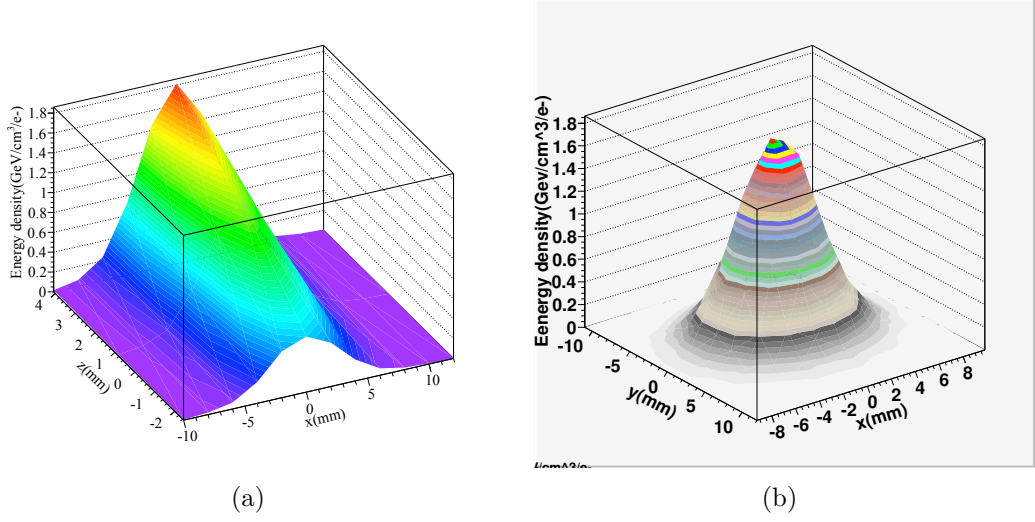


Figure 4.4: Energy deposition density in a granular target. ILC-VMS case. Target material: W. Sphere radius: 1mm . Granular layers: 3. Total target thickness: 10.19mm . (a): x-z plane view at center of y. (b): x-y plane view at end of the target.

incident beam can be given by[45]:

$$\sigma_{max} = E\eta\Delta T \frac{r}{\nu\tau_p} \quad (4.8)$$

where E is Young modulus. It is 411GPa for tungsten. η is thermal expansion coefficient which is $4.5 \times 10^{-6}\text{m/K/m}$ for tungsten at room temperature. ΔT is target temperature rise. τ_p is pulse duration. ν is the sound velocity which is $4.6 \times 10^3\text{m/s}$ for tungsten. For W granular target with sphere radius of 1mm , the temperature rise is 232K :

$$\sigma_{max} = 155\text{Mpa} \quad (4.9)$$

It is small due to the large width duration of minitrains and small temperature rise. The reduction factor of $r/(\nu\tau_p)$ is due to $\tau_p > \tau_s$, where τ_s is the time needed for the shock wave crossing the sphere.

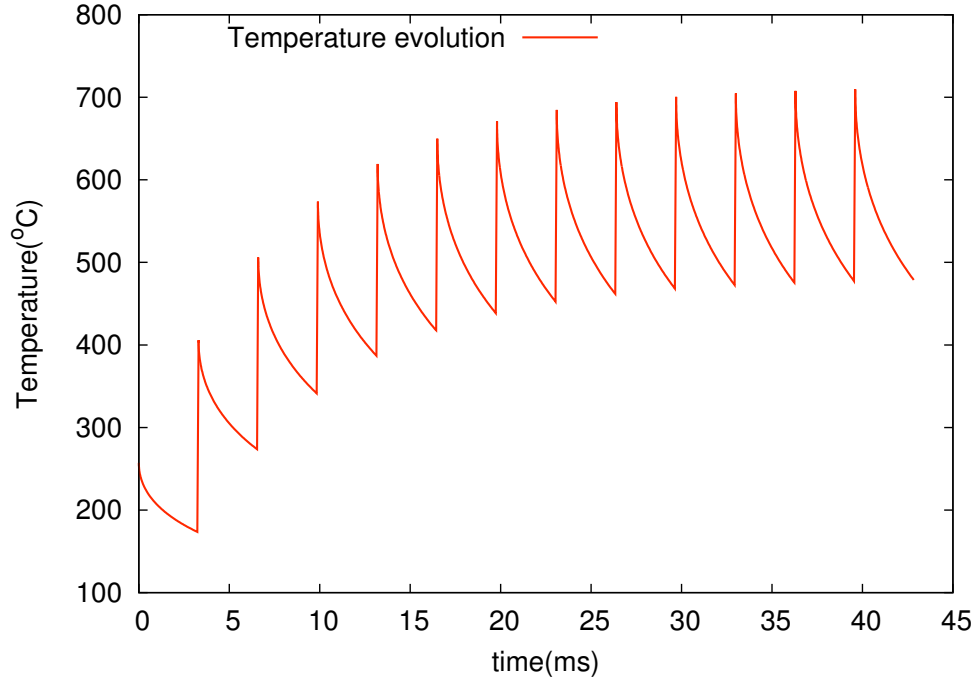


Figure 4.5: Temperature rise in function of time in one macropulse in the hottest part of granular target. VMS-ILC case. Granular thickness: 3 layers of cell in z direction. Sphere radius: 1mm.

Table 4.7: PEDD and temperature rise in the granular target. ILC-VMS case. Granular thickness: 3 layers of cell in z direction. Granular sphere radius: 1mm

Layer	Thickness (mm)	PEDD (J/g/minitrain)	ΔT (K)	Lowest T (K)	Highest T (K)
1	3.62	8.69	66.94	137.24	204.18
2	6.9	20.86	160.69	329.41	490.10
3	10.19	30.15	232.23	476.07	708.31
4	13.43	37.74	290.70	595.94	886.65
5	16.7	43.76	337.06	690.98	1028.05
6	19.96	44.49	342.68	702.50	1045.19

Table 4.8: PEDD and temperature rise in the granular target. ILC-VMS case. Granular thickness: 7 layers of cell in z direction. Granular sphere radius: 0.5mm

Layer	Thickness (mm)	PEDD (J/g/minitrain)	ΔT (K)	Lowest T (K)	Highest T (K)
1	1.81	4.92	37.96	30.74	68.70
2	3.44	10.24	78.86	63.88	142.74
3	5.08	15.81	121.80	98.66	220.47
4	6.71	21.98	169.30	137.13	306.44
5	8.34	26.69	205.62	166.55	372.18
6	9.98	31.71	244.29	197.87	442.17
7	11.61	35.68	274.80	222.59	497.39
8	13.24	40.36	310.87	251.80	562.67
9	14.88	44.42	342.13	277.12	619.26
10	16.51	44.70	344.28	278.87	623.15
11	18.14	44.53	343.03	277.85	620.88
12	19.77	47.72	367.53	297.70	665.24

Chapter 5

An Application On ILC

This chapter gives an application for ILC. A hybrid positrons source using crystal and granular target will be presented. The γ features at the exit of the crystal target are presented. Heating and cooling scheme for crystal target are discussed. Then we will talk about granular target with container structure. The energy deposition in the granular target and container are calculated and a pendulum structure are discussed. Positron features after the target are presented. The last section is about the positron beam propagation in the capture device. The capture efficiency and positron beam features after the capture device are presented.

5.1 Hybrid Source

The application in ILC is a hybrid target scheme which is composed of a crystal target and an amorphous granular converter, then an adiabatic matching device followed by a $1m$ long accelerator. $10GeV$ electron beam oriented to the main axis impinges on $1mm$ thick crystal target. Large numbers of soft photon are produced in crystal target. The photons are sent to the amorphous granular target and the charged particles are swept off. Helium gas is used for cooling the crystal target. The distance between crystal target and amorphous target is set to be $2m$ long to install a bending magnet which will sweep off the charged particles. According to the discussion in chapter 3 and 4, the granular target thickness is $10.2mm$ with sphere radius of $1mm$, which produces almost the same yield as a $8mm$ thick compact target. Pendulum structure using helium cooling is applied on granular target. A $50cm$ long AMD is installed after the granular target to capture the positron beam. The beginning of the magnetic field is $6Tesla$, and the exit is $0.5Tesla$.

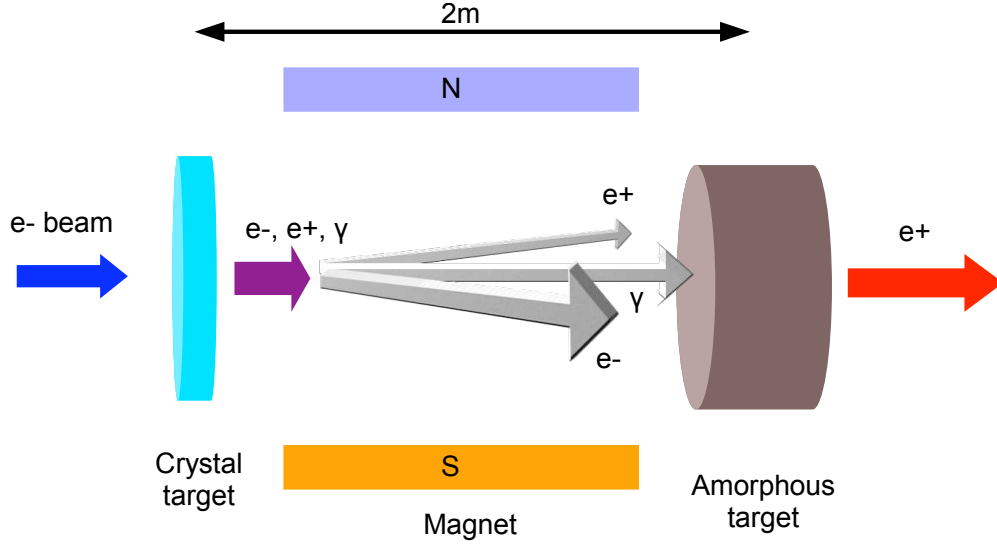


Figure 5.1: Hybrid scheme using crystal and granular target for ILC.

Comparing with conventional positron scheme, using crystal and granular target can increase photon yield and accelerate energy dissipation. The incident energy can be raised and the positron yield is high. Comparing with polarized positron schemes based on the undulator and compton back-scattering, the technology for hybrid source is easy to reach. The undulator is very large and complex, the cost is expensive. The technology for optical cavity used by compton back-scattering scheme is difficult and the positron yield is low.

5.2 Crystal Target

The crystal target material is tungsten; axis is $\langle 111 \rangle$ and the target thickness is 1mm . Fig. 5.2 shows the crystal target structure which is cooled by helium gas.

The crystal is mounted on a holder with Be-windows. The heating is evacuated from both sides of the crystal. This allows installing a support for the crystal which provides the stability in its orientation, but permits its unconstrained lateral thermal expansion, to reduce thermal stresses and fatigue. Five crystals are put on a transversally moving frame. This can reduce the average power deposition, where the PEDD per micropulse and macropulse will not change. The radiation damage is decreased by a factor of 5.

The incident electron energy is 10GeV with a rms of 2.5mm for lateral size. The γ yield at the end of crystal is $18.6\gamma/e^-$. Fig. 5.3a shows the energy spectrum of produced γ . The mean energy is 343MeV and rms is 766MeV . Fig. 5.3b shows distribution of transverse momentum P_x . Its rms value is $0.2\text{MeV}/c$. Fig. 5.3c shows the emittance of γ beam and Fig. 5.3d shows the angular distribution. It shows that the angle is very small, which means the large angle scattering in the crystal is not dominant.

The total energy deposition in the crystal target is $8\text{MeV}/e^-$. For KEK scheme this means a power of 166W . The crystal simulation programs can only deal with point injection. In order to study energy deposition density, here we use an amorphous target instead. Fig. 5.4 shows the energy deposition density in a 1mm amorphous W target. It has a peak value (PEDD) of $0.35\text{GeV}/\text{cm}^3/e^-$. For KEK scheme this means a PEDD of $5.82\text{J}/\text{g}/\text{minitrain}$ for a minitrain of $2 \cdot 10^{12}$ electrons. The above cooling scheme can solve the heating problem.

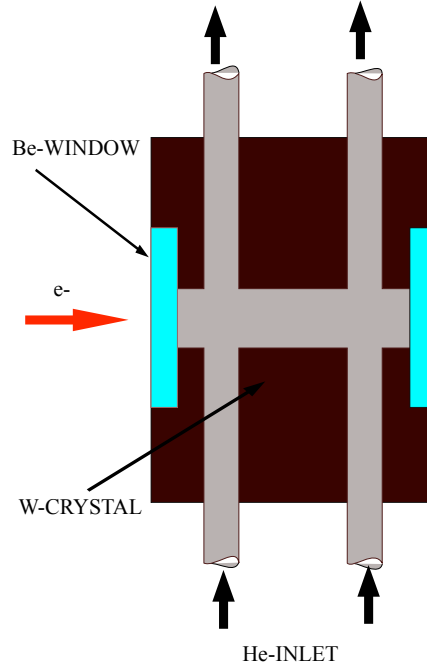


Figure 5.2: Crystal target with helium cooling.

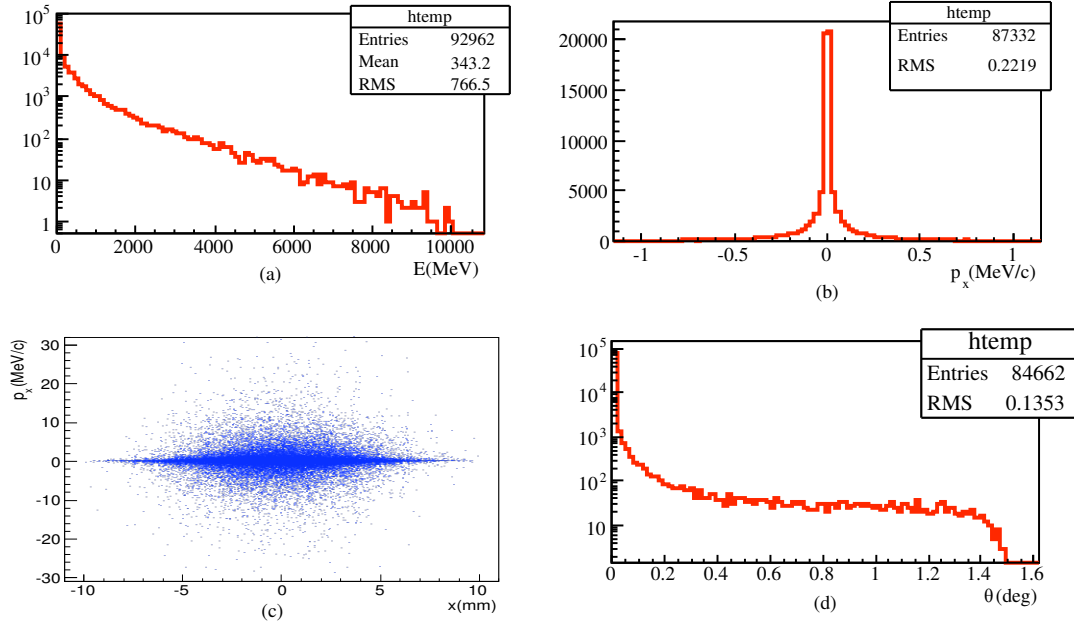


Figure 5.3: γ beam features at the end of crystal using G4Fot. Electron energy 10GeV . Crystal axis $\langle 111 \rangle$. Crystal thickness 1mm .

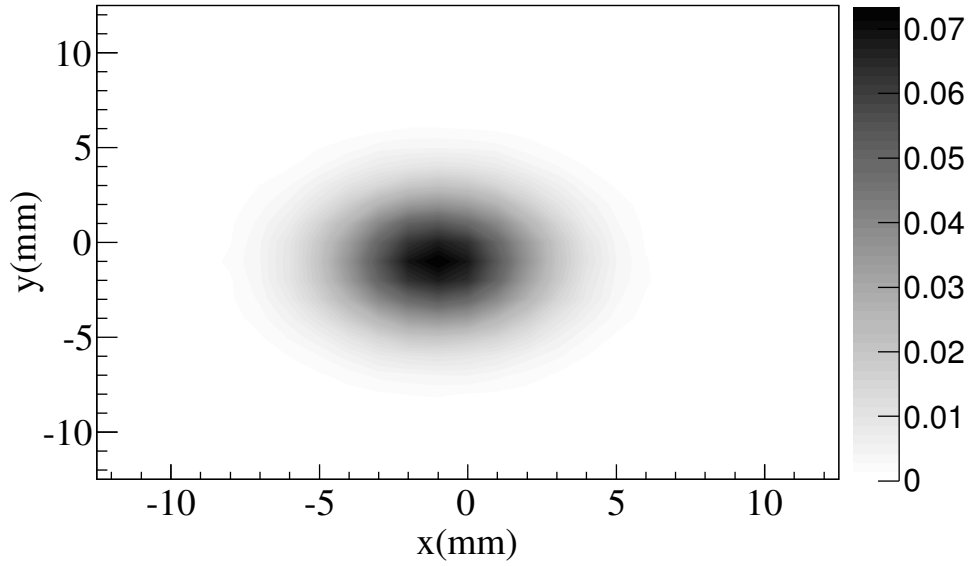


Figure 5.4: Deposited energy density in 1mm amorphous W target. Incident particle electron. Incident energy 10GeV . Energy density unit: $\text{GeV}/\text{cm}^3/e^-$

5.3 Pair Converter

Granular target can be cooled efficiently by helium gas, so we choose granular target. From Sec. 3.2.3, the the best choice of thickness for granular target is $10.19mm$ with the sphere radius of $1mm$. This can control the PEDD and get the highest positron yield. Because of using small spheres it needs to use a container to hold the spheres. Metal Be can be considered for upstream and downstream windows. Ti can be used for upper and lower windows which can give enough support for the target. Fig. 5.5 shows the amorphous structure. Be and Ti windows have a thickness of $1mm$.

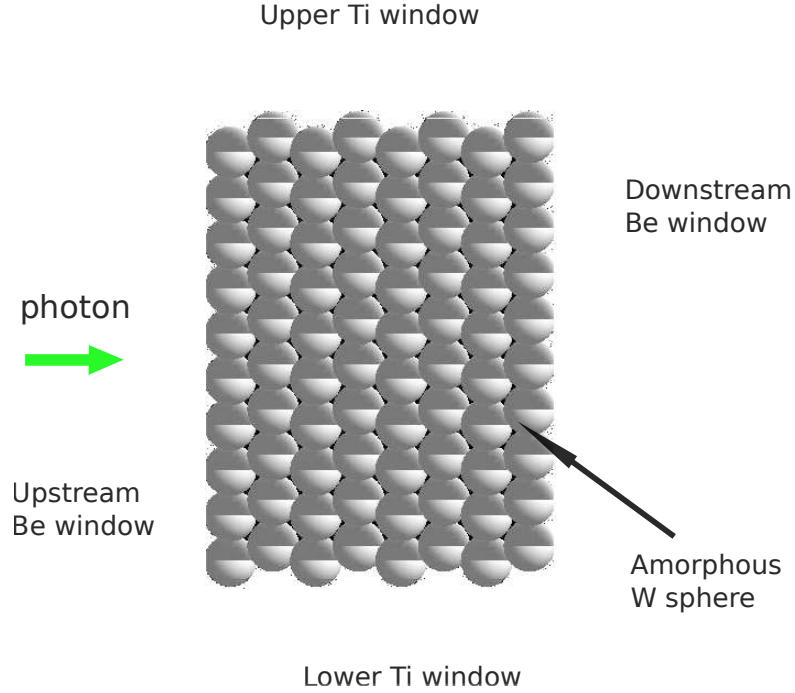


Figure 5.5: Amorphous target structure for ILC.

The positron yield at the exit of the amorphous target is $12.45e^+ / e^-$. Mean energy is $28MeV$ ($E < 200MeV$), FWHM is $18MeV$. For the lateral beam dimension the rms is $3.4mm$. Transverse momentum component p_x has a rms of $6.4MeV/c$. The beam profile is small size, large transverse momentum and large energy spread.

Because of multiple scattering in the granular target. The positron beam has a larger angle than γ beam. Fig. 5.6 shows the angle distribution for positron beam

at the exit of the amorphous target. The mean value is 0.35 rad and the rms is 0.37 rad.

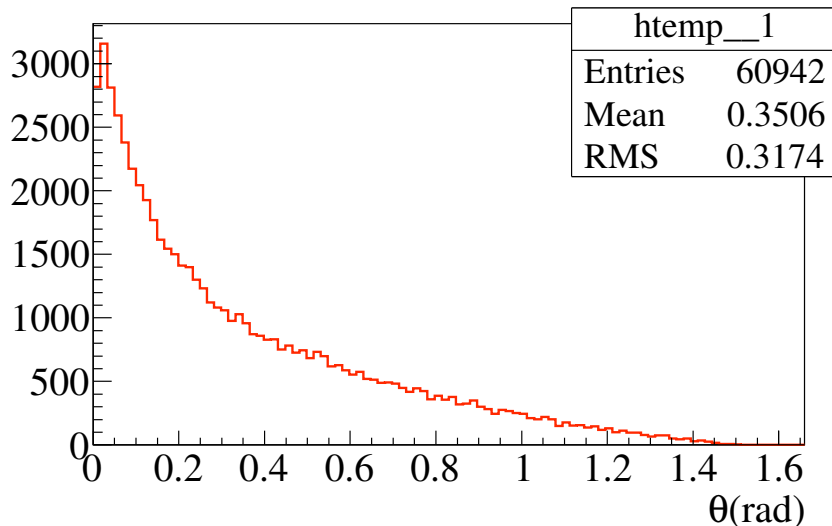


Figure 5.6: Positron beam angle distribution. Amorphous target layers 3, thickness 10.19mm. Sphere radius 1mm. Incident electron energy 10GeV. Incident lateral dimension r.m.s 2.5mm.

Table 5.1 shows the total energy and PEDD deposited in the granular target and four windows. Among four windows the downstream one has the highest total energy deposition and PEDD, 10.64MeV and 0.17GeV/cm³/e-. This is because of large number of particles coming out of the granular target. These particles have relatively low energy. When they cross through the Be window, they will deposit a lot of energy.

As Sec.4.2 mentioned, the stationary target is not workable because large amount of energy deposition in one macropulse will lead to serious heating problems. A rotating or pendulum scheme should be considered to dilute the energy deposition. To avoid rotating seals, wobbling and trolling targets have been devised at Durham ILC e+ Meeting in Oct. 2009. Here we consider a "Pendulum Scheme", as shown in Fig. 5.7. The movement of the pendulum is provided by a sinusoidal oscillation. The width of the target is 13cm, with moving velocity of 3m/s over $\pm 7deg$ providing 1cm space for each minitrain in one macropulse which contain 13 minitrains. The total swing is $\pm 23deg$ which allow for target go back to original state, inversion of direction of the movement during the "off beam" time of 160ms. In this scheme the displacement of the target structure

Table 5.1: Total energy and PEDD deposited in granular target and windows.

Section	Total E deposition (MeV/e-)	PEDD (GeV/cm ³ /e-)
Granular target(W)	456.49	1.88
Up window(Be)	0.13	0.0016
Down window(Be)	10.64	0.1758
Upper window(Ti)	0.13	0.0020
Lower window(Ti)	0.14	0.0022

from the outside into the vacuum is made via flexible, vacuum tight bellows. The injection of the cooling fluid can be ensured through a fixed structure. The range in angle must be sustained by the bellows oscillating at $2.5Hz$.

In this scheme, one macropulse is spread in $13cm$ width bar. So the energy deposition and temperature rise in one macropulse is decreased by a factor of 13. The energy deposition in the same spot in one macropulse is $142.7J$. The temperature rise of Helium in $0.2s$ is $68K$ with mass flow of $3.2 \cdot 10^{-3}kg/s$. The PEDD is yet $30J/g/minitrain$ and the peak temperature rise is $232K$. In one macropulse it will decrease to room temperature $T_0(K)$ and the highest temperature will be $(232 + T_0)K$. During the time between two macropulses hitting the same target, which is $200ms$, the target temperature will decrease close to room temperature.

More detail of rotating wheel for cooling granular target is under study. Fig. 5.8 shows the scheme. Since the deposited beam energy is concentrated within a diameter of about $1cm$ (see Fig. 4.4), with a linear velocity of the rim of the rotating wheel of about $3m/s$, the rim is displaced by $1cm$ over $3.3ms$, so the energy of each minitrain is separated from the adjacent, following minitrain. Only very little pile up occurs. The calculated maximum temperature rise in the target rim, resulting from the PEDD per minitrain, is not exceeding $232K$.

The total energy deposition and PEDD in Titanium upper and lower windows is negligible. For the downstream windows, the total energy deposition is $3J$. The PEDD is $29J/g/minitrain$ which will lead to sustainable temperature rise of about $15K/minitrain$. Fig. 5.9 represents the energy deposition density in the downstream Be window.

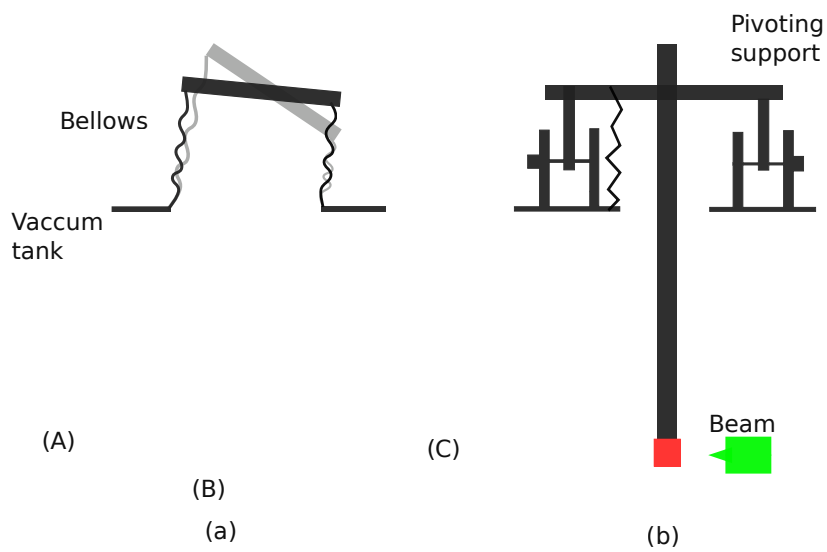


Figure 5.7: The pendulum for a granular target.

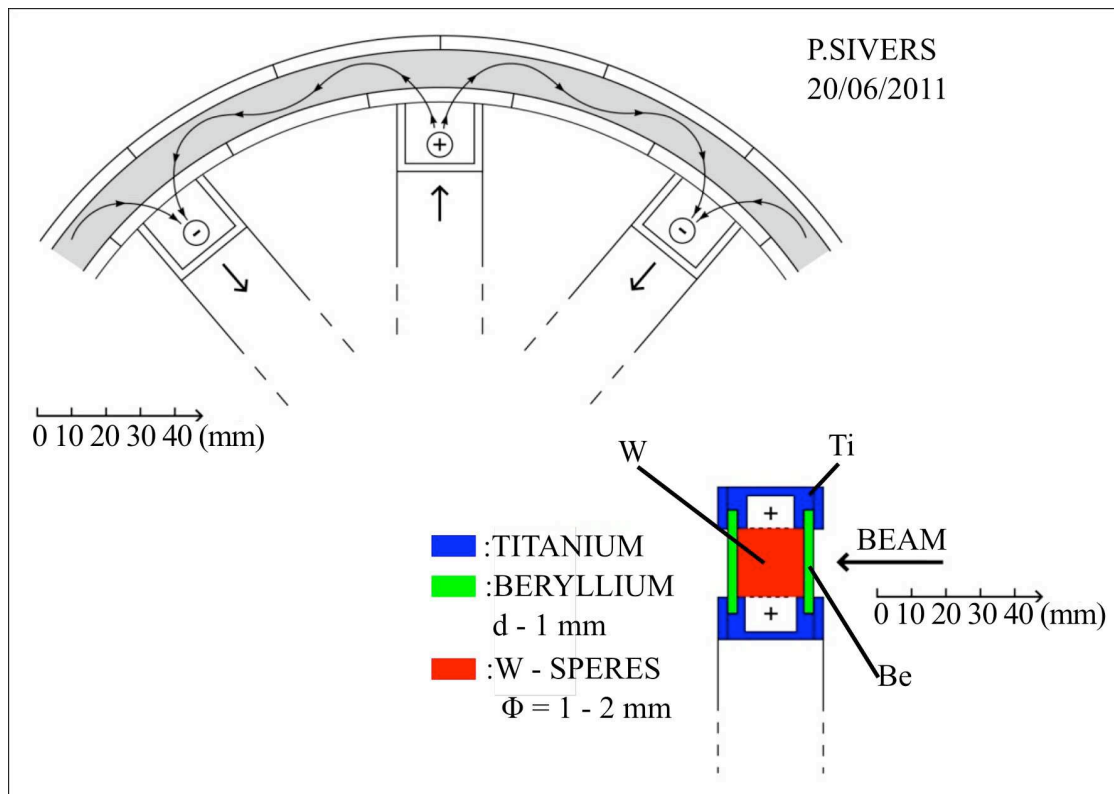


Figure 5.8: The rotating wheel for a granular target. by Peter SIEVERS.

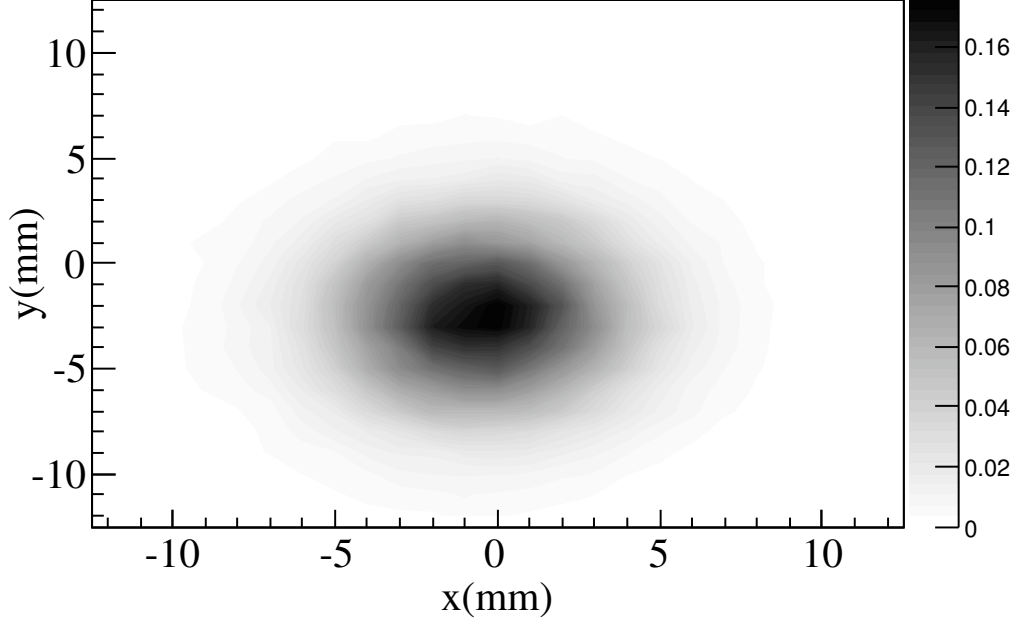


Figure 5.9: Energy deposited density in downstream Be window. VMS-ILC case. Energy density unit: $\text{GeV}/\text{cm}^3/e^-$.

5.4 Capture Device

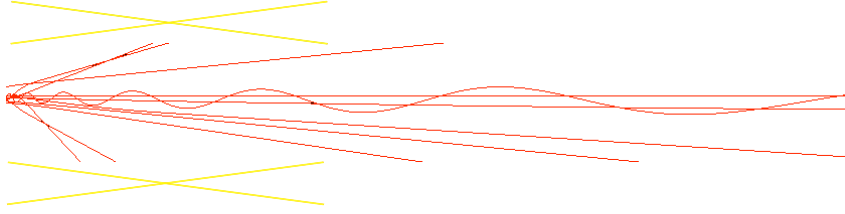
Adiabatic Matching Device has a large energy and geometry acceptance. Here we choose it as capture device in the application in ILC. Fig. 5.10 shows the capture device structure. It is an AMD followed by a 1m long accelerator. Both diameter of AMD and accelerator are 40mm. The length of the AMD is 50cm, B_0 is 6Tesla and B_s is 0.5Tesla. The accelerator has a constant magnetic field of $B_z = 0.5\text{Tesla}$ by using solenoid, the constant electric field is $E_z = 15\text{MV}/m$.

The yield at the exit of the AMD is $4.5e^+ / e^-$ and $2.3e^+ / e^-$ at the exit of the accelerator. The lateral dimension increases from 3.1mm to 8.1mm. Transverse momentum p_x decreases from $7.7\text{MeV}/c$ to $2.1\text{MeV}/c$. FWHM of energy decreases from 18MeV to 9MeV .

Figure 5.11 shows the angle distribution at the exit of the AMD and accelerator. Compared with Fig. 5.6, from the exit of the target to the exit of the accelerator,

the mean angle decreases from $0.35rad$ to $0.024rad$. The rms decreases from $0.31rad$ to $0.016rad$.

Target



AMD

Accelerator

Figure 5.10: Capture Device structure for ILC.

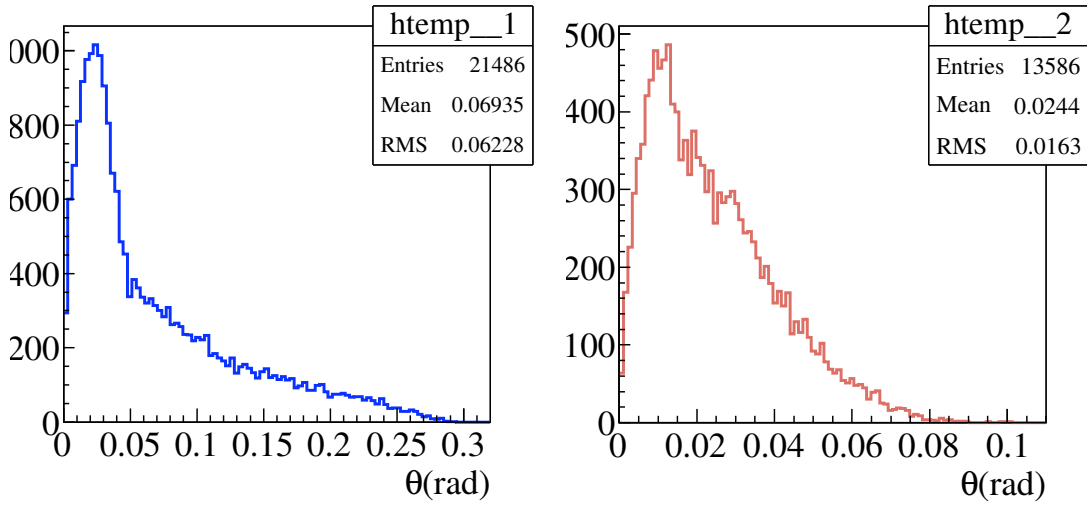


Figure 5.11: Angle distribution for positron beam. VMS-ILC case. (a) At the end of AMD. (b) At the end of accelerator.

Chapter 6

Control of Emittance

This chapter will discuss the emittance control of positron beam at the exit of the target and capture. To control the emittance and increase the particles energy, an accelerator structure is introduced to accelerate the positrons up to $300MeV$. Parmela is used in the simulation. The phase of accelerator, positron beam energy spectrum, longitudinal and transverse emittance are optimized.

6.1 Accelerator theory

Accelerators are designed to accelerate or collect particles. A beam of charged particles is expected by design to follow closely a prescribed path along a desired beam transport line or along a closed orbit in case of circular accelerators. The forces required to accelerate, focus, hold, bend and direct the charged particle beam come from electric and magnetic field supplied by components of accelerators.

6.1.1 Particle dynamics in electromagnetic fields

The force felt by a particle carrying a single basic unit of electrical charge in electromagnetic field is expressed by Lorentz force[46]:

$$\mathbf{F} = e\mathbf{E} + e(\boldsymbol{\nu} \times \mathbf{B}) \quad (6.1)$$

Here we use SI units system. \mathbf{E} and \mathbf{B} are electric field and magnetic field. $\boldsymbol{\nu}$ is the velocity of particle.

In circular accelerator usually natural coordinate frame is most frequently used, where y is vertical direction, x is horizontal direction and s is the direction of particle velocity(longitudinal).Then[46]

$$\mathbf{R} = r\hat{x} + y\hat{y} \quad (6.2)$$

where $r = \rho + x$. ρ is the radius of curvature of the trajectory. If there is no electric field, then:

$$\frac{d\mathbf{p}}{dt} = e(\boldsymbol{\nu} \times \mathbf{B}) \quad (6.3)$$

\mathbf{p} is momentum, for s we have

$$\frac{d}{dt} = \frac{ds}{dt} \frac{d}{ds} \quad (6.4)$$

and

$$ds = \rho d\theta = \nu_s \frac{\rho}{r} dt \quad (6.5)$$

Assuming $\nu_x \ll \nu_s, \nu_y \ll \nu_s$, and supposing \mathbf{B} has no component in s direction, the transverse linear motion equation becomes[46]:

$$\frac{d^2x}{ds^2} - \frac{\rho + x}{\rho^2} = -\frac{B_y}{B\rho} \left(1 + \frac{x}{\rho}\right)^2 \quad (6.6)$$

$$\frac{d^2y}{ds^2} = \frac{B_x}{B\rho} \left(1 + \frac{x}{\rho}\right)^2 \quad (6.7)$$

B_x and B_y can be written as:

$$B_x = B_x(0,0) + \frac{\partial B_x}{\partial y}y + \frac{\partial B_x}{\partial x}x \quad (6.8)$$

$$B_y = B_y(0,0) + \frac{\partial B_y}{\partial x}x + \frac{\partial B_y}{\partial y}y \quad (6.9)$$

Assuming no bending in vertical direction($B_x(0,0) = 0$) and no couple in x and y direction($\partial B_y/\partial y = \partial B_x/\partial x = 0$), we can get $\partial B_y/\partial x = \partial B_x/\partial y$. Finally the transverse motion equation can be expressed as[46]:

$$\frac{d^2x}{ds^2} + K_x(s)x = 0 \quad (6.10)$$

$$\frac{d^2y}{ds^2} + K_y(s)y = 0 \quad (6.11)$$

where

$$K_x = \frac{1}{\rho^2} + \frac{1}{B\rho} \frac{\partial B_y(s)}{\partial x} \quad (6.12)$$

$$K_y = -\frac{1}{B\rho} \frac{\partial B_y(s)}{\partial x} \quad (6.13)$$

Eq. (6.10) is Hill equation. K_x and K_y depend on the accelerator elements. Solution of Hill equation can be written as matrix form[46]:

$$\mathbf{X}_2 = \mathbf{M}\mathbf{X}_1 \quad (6.14)$$

where

$$\mathbf{X}_1 = \begin{pmatrix} x \\ x' \end{pmatrix}_1, \mathbf{X}_2 = \begin{pmatrix} x \\ x' \end{pmatrix}_2, \mathbf{M} = \begin{pmatrix} a & b \\ c & d \end{pmatrix} \quad (6.15)$$

where \mathbf{M} is Transform Matrix, determined by lattice elements:

$$\mathbf{M} = \mathbf{M}_n \cdot \mathbf{M}_{n-1} \cdots \mathbf{M}_2 \cdot \mathbf{M}_1 \quad (6.16)$$

Transverse stability require that \mathbf{X}_2 must be finite, from what we get the transverse stability condition[46]:

$$-1 \leq \frac{1}{2}Tr(\mathbf{M}) \leq 1 \quad (6.17)$$

For drift tube, $K = 0$, the Transform Matrix is:

$$\mathbf{M} = \begin{pmatrix} 1 & L \\ 0 & 1 \end{pmatrix} \quad (6.18)$$

For focusing magnet with a length of l , $K > 0$

$$\mathbf{M} = \begin{pmatrix} \cos(\sqrt{K}l) & \frac{1}{\sqrt{K}}\sin(\sqrt{K}l) \\ -\sqrt{K}\sin(\sqrt{K}l) & \cos(\sqrt{K}l) \end{pmatrix} \quad (6.19)$$

For defocusing magnet with a length of l , $K < 0$

$$\mathbf{M} = \begin{pmatrix} \cosh(\sqrt{|K|}l) & \frac{1}{\sqrt{|K|}}\sinh(\sqrt{|K|}l) \\ -\sqrt{|K|}\sinh(\sqrt{|K|}l) & \cosh(\sqrt{|K|}l) \end{pmatrix} \quad (6.20)$$

Usually quadrupole lattice is used to focus particle beam in accelerator. quadrupole is a type of strong focus element. It focus in one direction and defocus in the other direction at the same time. However, quadrupole lattice can be designed to focus in both transverse direction. The focus length of a quadrupole is[46]:

$$\frac{1}{f} = \frac{eB'l}{p} \quad (6.21)$$

where B' is magnetic gradient and $p/e = B\rho$ is called magnet rigidity. The transform matrix for quadrupole is:

$$\mathbf{M} = \begin{pmatrix} 1 & 0 \\ -\frac{1}{f} & 1 \end{pmatrix} \quad (6.22)$$

In circular accelerator, assuming C is circumference, $K(s + C) = K(s)$. The solution for Hill equation is[46]:

$$x(s) = A\sqrt{\beta(s)}\cos[\psi(s) + \delta] \quad (6.23)$$

where A is a constant number, here we define

$$\beta(s) = \frac{w^2(s)}{k} \quad (6.24)$$

$$\alpha(s) = -\frac{1}{2} \frac{d\beta(s)}{ds} = -\frac{1}{2} \frac{d}{ds} \left(\frac{w^2(s)}{k} \right) \quad (6.25)$$

$$\gamma(s) = \frac{1 + \alpha^2}{\beta} \quad (6.26)$$

where w is a periodical function with period C . α, β, γ are called Courant-Snyder or Twiss parameter. They can be written as[46]:

$$K\beta = \gamma + \alpha' \quad (6.27)$$

In accelerator we usually use RF cavity to accelerate particles. Let R be the radius of cavity and L is the length. Supposing in RF cavity it just has components E_z and E_θ , the Maxwell equation has the following form:

$$\frac{1}{r} \frac{\partial}{\partial r} (rB_\theta) = \frac{1}{c^2} \frac{\partial E_z}{\partial t} \quad (6.28)$$

$$\frac{\partial E_z}{\partial r} = \frac{\partial E_\theta}{\partial t} \quad (6.29)$$

The solution is:

$$E_z(r, t) = E(r)e^{i\omega t} \quad (6.30)$$

$$E(r) = E_0 J_0 \left(\frac{\omega}{c} r \right) \quad (6.31)$$

J_0 is zero order of Bessel function. If the cavity is ideal conductor, $E(R) = 0$. Then the lowest harmonic frequency:

$$\frac{\omega}{c} R = 2.405 \quad (6.32)$$

For circular accelerator, assuming $(E_s)_n$ is the energy of synchrotron particle at the n^{th} cavity with charge e , then

$$(E_s)_{n+1} = (E_s)_n + eV \sin(\phi_s) \quad (6.33)$$

For none ideal particle

$$E_{n+1} = E_n + eV \sin(\phi_n) \quad (6.34)$$

The energy difference is

$$\Delta E_{n+1} = \Delta E_n + eV \sin(\phi_n - \phi_s) \quad (6.35)$$

The boundary equation of particle motion in $\phi - \Delta E$ phase space can be solved as[46]:

$$\Delta E^2 + \frac{2v^2 E_s eV}{\eta \omega_{rf} \tau c^2} (\cos \phi + \phi \sin \phi_s) = \text{const.} \quad (6.36)$$

where τ is time between two cells of cavity and ω_{rf} is cavity frequency. η is Slippage factor.

6.1.2 RF cavity

According to the relativistic theory, particle velocity must be less than the light velocity. So the phase velocity of high frequency accelerator field must be less than the light velocity. So slow wave structure is needed in accelerating particles. Here we use disk-wave guide cavity. Fig. 6.1 shows the cavity structure.

The length of cavity can be estimated by Transit time factor. Which is rate of energy gained when particle is right at the center of cavity where the electric field is peak and energy gained when electric field is constant(maximum value)[47]

$$T = \frac{\int_{-L/2}^{L/2} E_z \cos(\omega z / \nu) dz}{\int_{-L/2}^{L/2} E_z dz} \quad (6.37)$$

The wall losses are related to the quality factor Q of the structure.

$$Q = \frac{\omega W}{P_w} \quad (6.38)$$

where W is the stored energy per unit length. P_w/ω is wall losses per unit length and per radian of field oscillation.

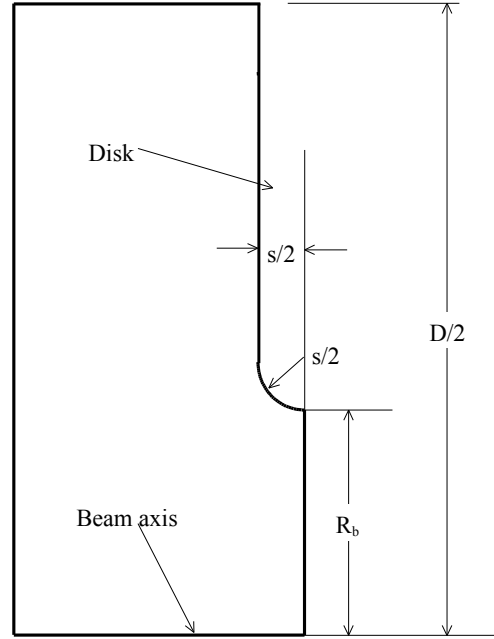


Figure 6.1: Disk-loaded waveguide[47].

Another important parameter of cavity is shunt impedance R_s , defined by:

$$P_{cy} = \frac{V_{cy}^2}{2R_s} \quad (6.39)$$

where P_{cy} is cavity losses and V_{cy} is effective voltage.

The axial electric field in a standing-wave rf cavity imparts energy to a particle according to the equation[47]:

$$\Delta W = q \int_{-L/2}^{L/2} E_z(z, t) dz = q \int_{-L/2}^{L/2} E_z(z) \cos(\omega t + \phi) dz \quad (6.40)$$

where L is the cavity length, q is the particle charge.

6.1.3 Phase stability

Figure 6.2 demonstrates the phase shift in the accelerator. Electromagnetic field transports from left to right with velocity c . Suppose a reference particle with velocity c at point A travels to A' after period T . The field is $\sin(\phi)$ and $\sin(2\pi + \phi)$. A non-light particle at point A will need more time than T to arrive at point A' because its velocity is less than c . The field it meets is $\sin(\phi)$ and $\sin(2\pi + \phi + \Delta\phi)$. So there is a phase difference of $\Delta\phi$. Lower energy particle will gain more energy and shift to reference phase. Higher energy particle will gain less energy and shift to reference phase. The beam particles with certain energy and phase difference will not be lost. This is the principle of phase stability discovered by V.I.Veksler and E.M.McMillan.

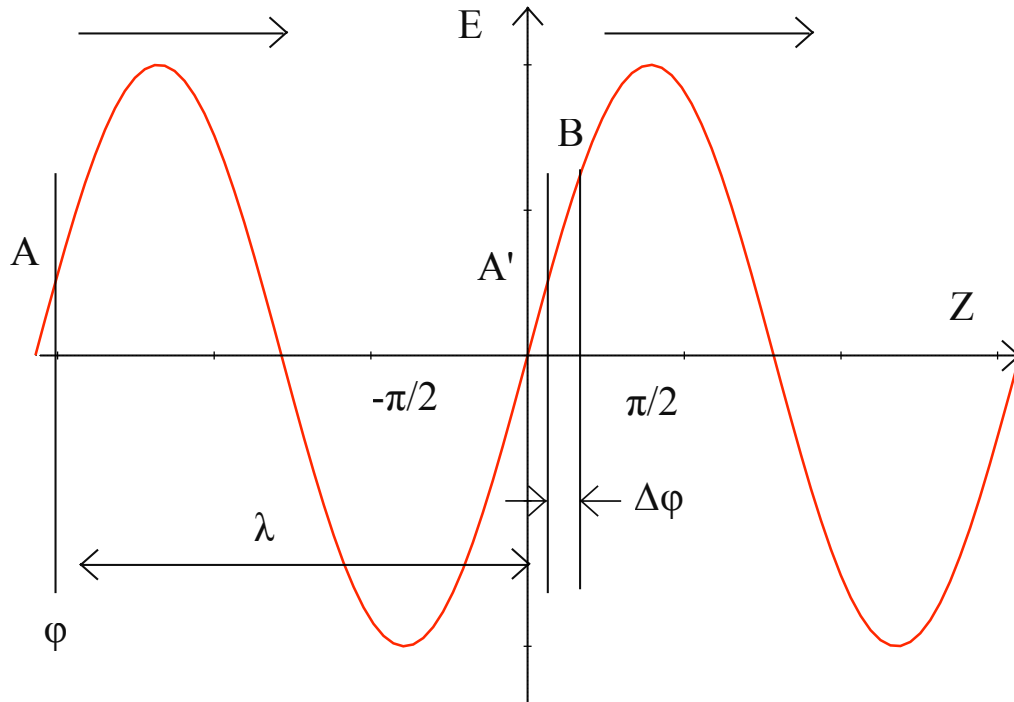


Figure 6.2: Phase shift demonstration.

6.1.4 Emittance

In the $x - x'$ and $y - y'$ phase planes, the r.m.s emittance is defined as[48]:

$$\varepsilon_{x,rms} = \frac{1}{N} \sqrt{\sum_{i=1}^N x_i^2 \sum_{i=1}^N x_i'^2 - \left(\sum_{i=1}^N x_i^2 x_i'^2 \right)^2} \quad (6.41)$$

$$\varepsilon_{y,rms} = \frac{1}{N} \sqrt{\sum_{i=1}^N y_i^2 \sum_{i=1}^N y_i'^2 - \left(\sum_{i=1}^N y_i^2 y_i'^2 \right)^2} \quad (6.42)$$

where N is the total number of particles, x_i and x_i' are the i th particle's space and divergence coordinates, and similarly for the $y - y'$ coordinates. For the longitudinal phase space, the definition is:

$$\varepsilon_{z,rms} = \frac{1}{N} \sqrt{\sum_{i=1}^N \phi_i^2 \sum_{i=1}^N E_i^2 - \left(\sum_{i=1}^N \phi_i^2 E_i^2 \right)^2} \quad (6.43)$$

where ϕ_i is the i th particle phase and E is the energy.

The emittance of positron beam at the exit of the capture system are shown in Table 6.1. It can be seen that the emittance is very large. In order to acquire positrons as much as possible, an accelerator system with solenoid magnetic field is needed to match the beam emittance.

Table 6.1: Emittance at the end of AMD

normalized rms x (cm-rad)	normalized rms y (cm-rad)	unnormalized rms z rms(cm)
4749.2	4735.6	23.4

6.2 Accelerator system

In this project Parmela is used to simulate the positron beam transportation in the accelerator system with energy up to $300MeV$ after the capture system. Parmela is an electron linear particle dynamic simulation program. It is the abbreviation of Phase and Radial Motion in Electron Linear Accelerator, Written by Los Alamos National Laboratory. It can trace particle motion in user defined accelerator system, cell, tank, quadrupole, drift, solenoid or coil(background magnetic), and other elements. It can simulate space charge. It is suitable for electron, positron and ions.

The incident electron beam bunch length is set to $10ps$. After the Adiabatic Matching Device, the bunch lengthening due to the spiralization in the longitudinal magnetic is serious, emittance is very large(See Table 6.1). To capture more positrons, $1.3GHz$ L-Band π mode standing wave cavity structure is used. There are 8 cells per cavity. The length of a cavity is $1.02m$. The aperture size is $4cm$. The average electric field of the cavity is $15MV/m$. Fig. 6.3 shows the 8-cell accelerating structure and Fig. 6.4 shows the electric field distribution in a cavity.

The accelerator system is composed of 30 cavities and the drift tube connect the two adjacent cavities, the total length of the accelerator system is $34.6m$. The accelerator system is immersed in solenoid which is used to control the positron beam. The magnetic field is $0.5Tesla$. Fig. 6.5 shows the accelerator system structure. Fig. 6.6 shows the electric field in the accelerator system and Fig. 6.7 shows the magnetic field.

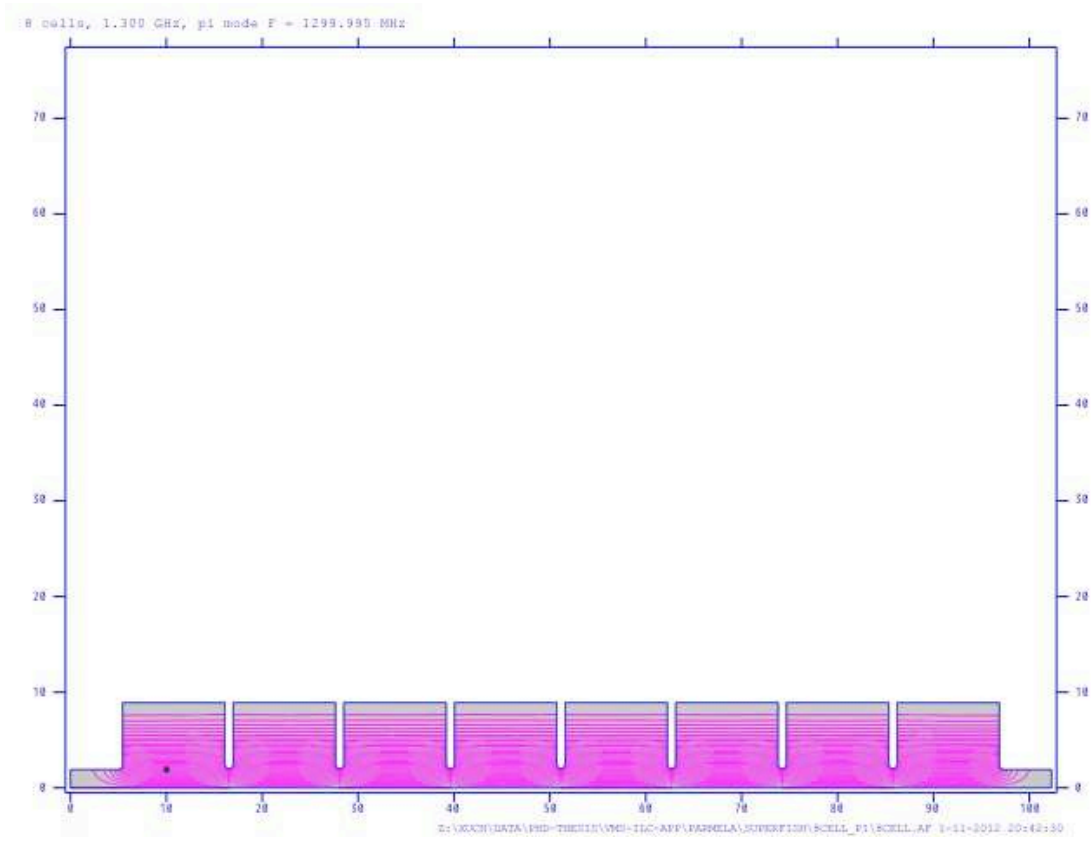


Figure 6.3: The 8-cell disk-loaded cavity structure. It is 1.3GHz π mode.

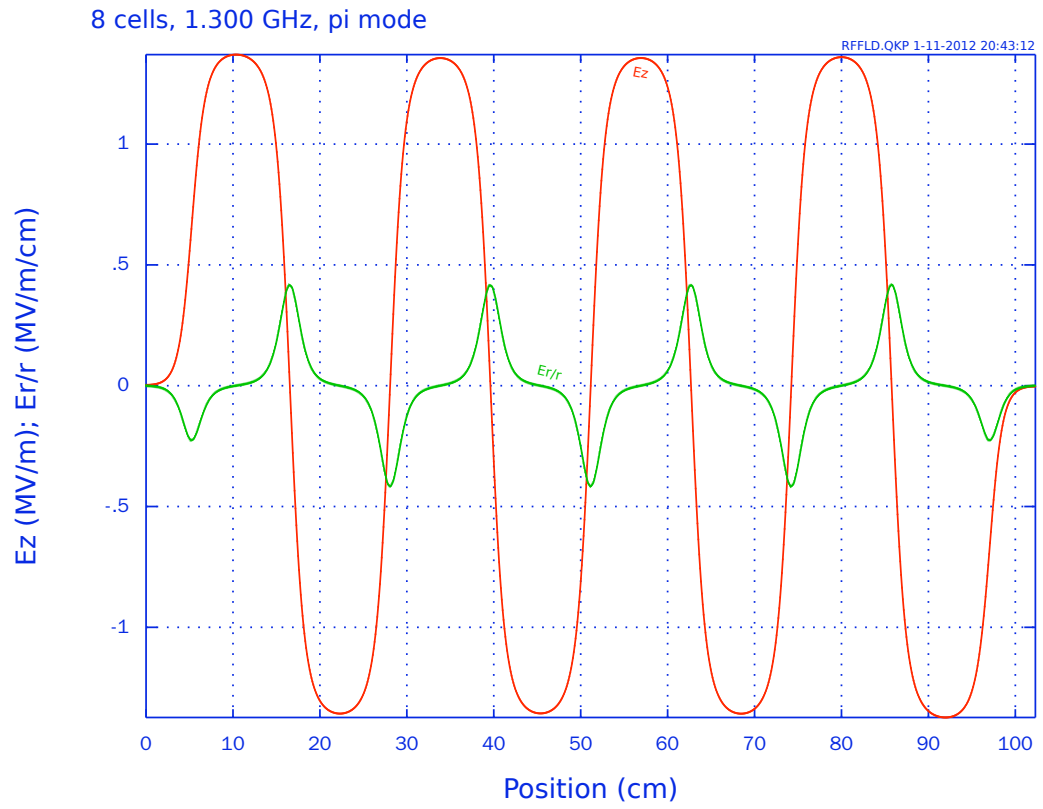


Figure 6.4: The electric field distribution in the 8-cell disk-loaded cavity. It is 1.3GHz π mode.

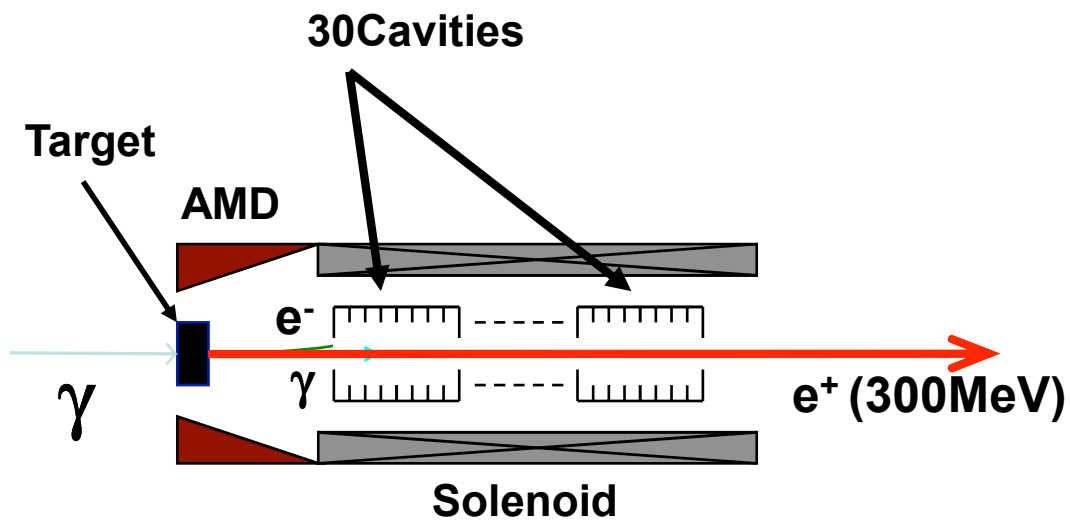


Figure 6.5: Structure of 8-cell cavity accelerator system

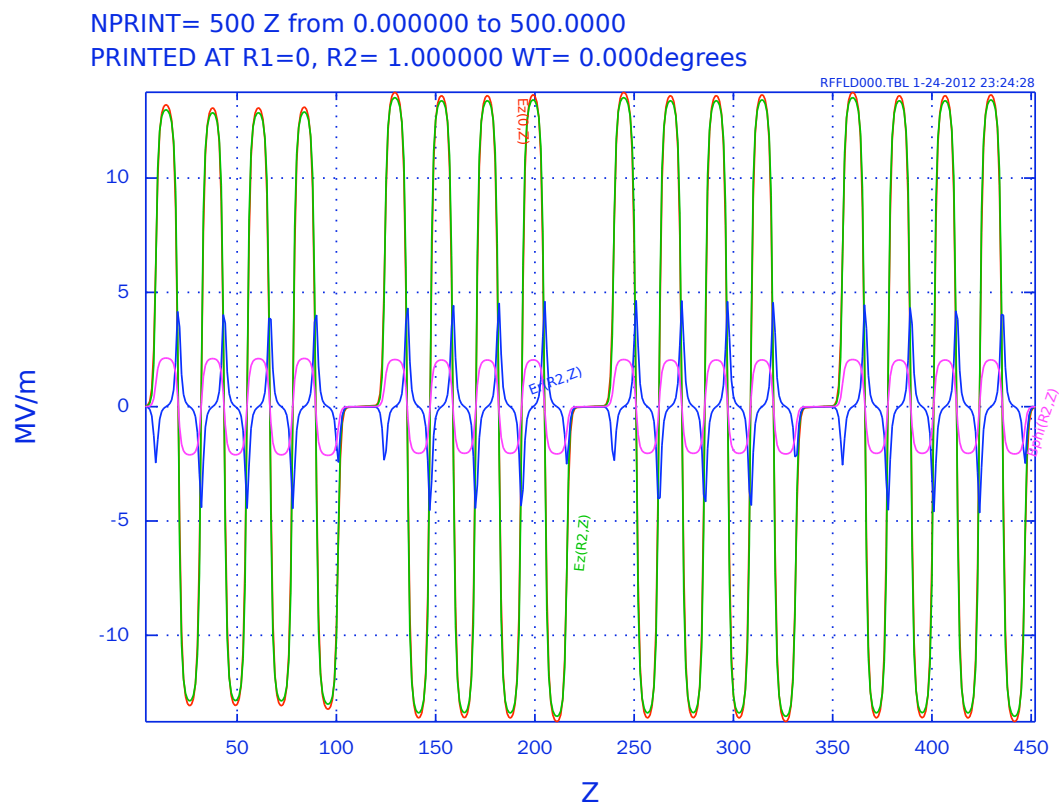


Figure 6.6: Electric field in the accelerator system

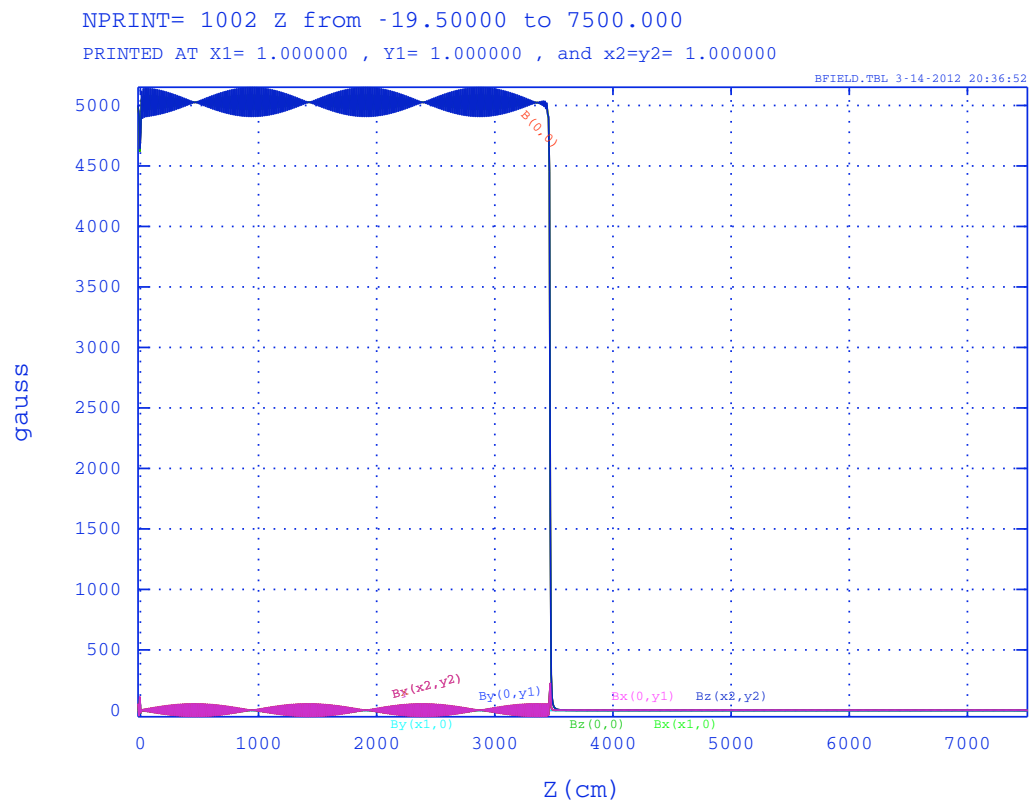


Figure 6.7: Magnetic field in the accelerator system

6.3 Configuration of Parmela

In Parmela simulation, all particles' energy and phase are represented with respect to the reference particle's energy and phase. The energy of positron beam at the exit of the AMD is mainly distributed between $4 - 50\text{MeV}$. Here the energy of reference particle is set to be 10.41MeV . In Geant4 time is used to represent particle's 4th dimension. In Parmela the phase is used. So we need to transfer time to phase according to the accelerator frequency. Fig. 3.12b shows the time distribution of positron beam at the exit of the AMD. The phase corresponding to the peak value is considered as phase of the reference particle and is set to be 0deg . Fig. 6.8 shows the particles' phase distribution.

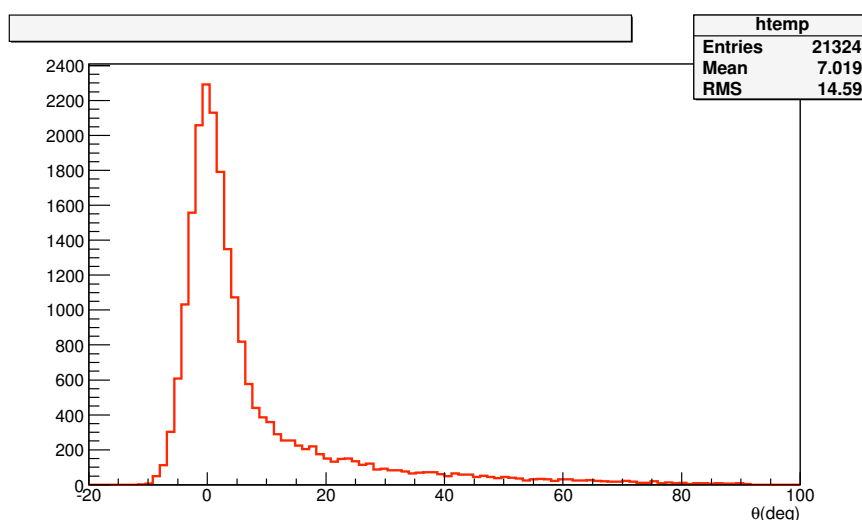


Figure 6.8: Phase of positron beam at the end of AMD.

A very important parameter in Parmela is the phase of the accelerator. In Parmela it use sine convention. For positive particle $0 \sim 180\text{deg}$ is accelerating range and $-180 \sim 0\text{deg}$ is decelerating range. Fig. 6.9 shows the energy-phase curve for positron beam at the exit of the AMD. We can see that the phase range is large, more-over most low energy particles have large phases. In order to minimize the particle loss we should choose maximum capture phase for accelerator according to phase stability principle. For reference phase between $-90 \sim 90\text{deg}$, low energy particle with large phase will gain more energy and shift to reference phase, high energy particle with small phase will gain less energy and shift to reference phase. The phase space will be narrow. Fig. 6.10 shows the particle yield in the 4 tank accelerator system versus the tank phase. Each tank has 16 cells. The incident positrons are 5000. It can be seen that the yield has a peak

value of phase ~ 0 or ~ 180 .

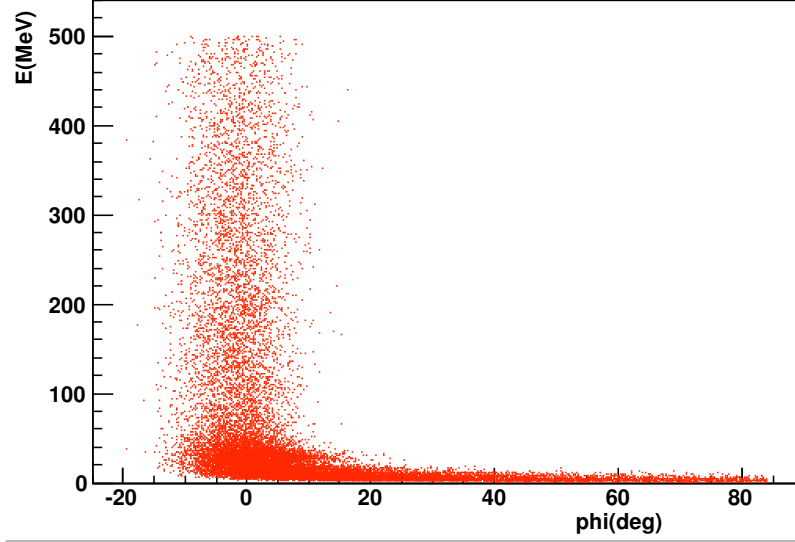


Figure 6.9: Phase vs energy of positron beam at the end of AMD.

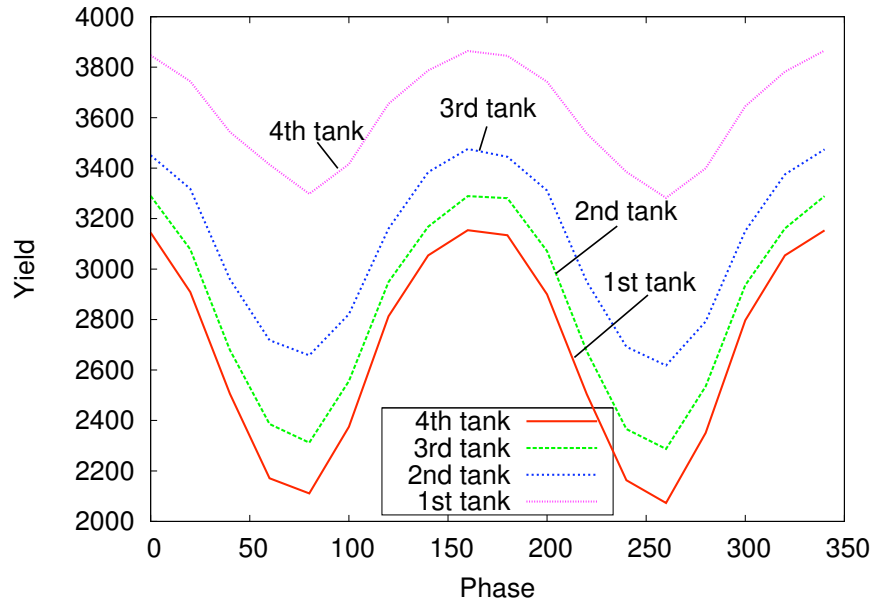


Figure 6.10: Yield vs Phase in four tank accelerator system. π mode. 16 cells. Incident positrons: 5000. Positrons comes from VMS-ILC end of 50cm AMD.

The total bunch length can be expressed in phase. The energy spread and bunch length have the following relationship[49]:

$$\frac{\Delta E}{E} = \frac{\Delta \phi^2}{8} \quad (6.44)$$

The bunch length $\Delta \phi$ needs to be shorter to get lower energy spread. Because the energy acceptance of the Damping ring is limited($\leq 1\%$, generally).

6.4 Simulation results

With optimized cavities phase, Fig. 6.12 shows the total yield and reference energy versus the length. It shows that the total yield decreases very quickly in the first four cavities, then decreases slowly. The total yield at energy $\sim 300MeV$ is about 0.8, which is small. An explanation is the transverse electric field of the cavity and large emittance of input beam result into large beam loss. Fig. 6.13 shows the $x - xp$ phase distribution at different points. It shows that the volume of transverse phase space decreases quickly at first, then arrives at a "stable" state. Fig. 6.14 shows the phase, $x - y$, $phi - E$ and energy distribution. Phase and energy are represented with respect to the reference particle's phase and energy. It shows that the phase distribution and energy distribution do not change significantly. Table 6.2 shows the rms emittance, α and β parameters at difference position. Fig(6.11) shows the x and y envelope evolutions. The conclusion is that the particle loss is serious and more optimization is needed. The particle loss is mainly coming from the transverse loss, the first reason is due to the large transverse emittance and the second is the transverse defocusing force.

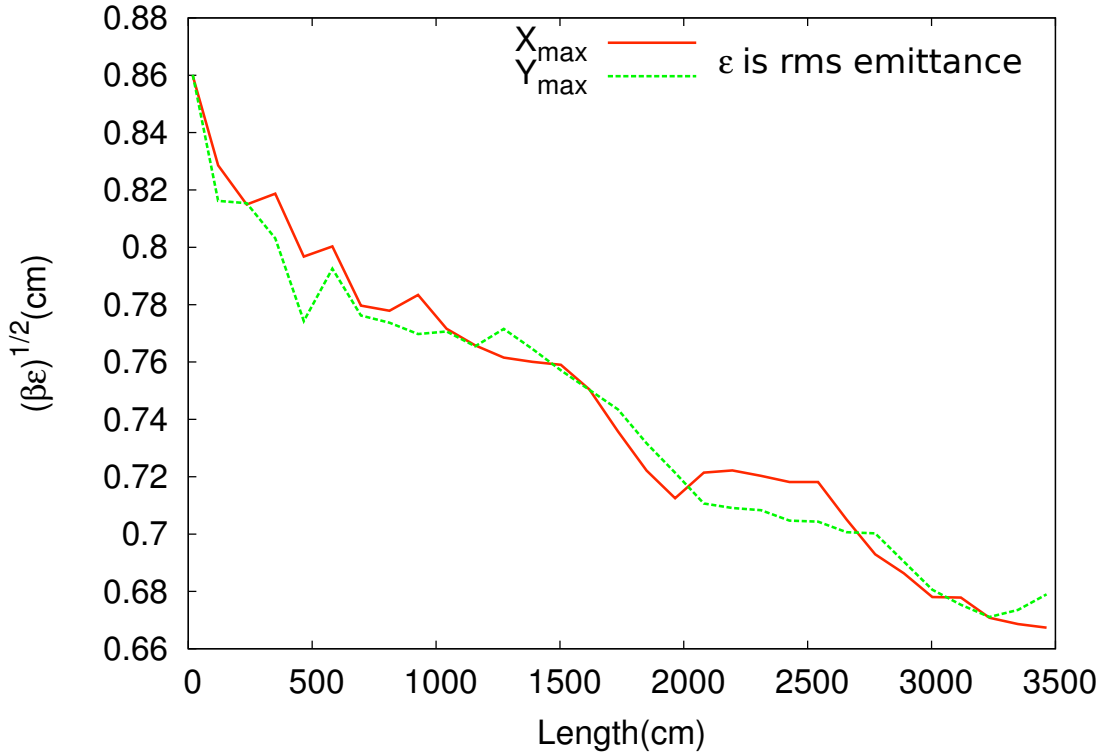


Figure 6.11: x and y envelope evolution in the 8-cell cavity accelerator system.

Table 6.2: Unnormalized emittance, α and β at different position in the 8-cell tank accelerator.

position (cm)	x emittance rms(cm-rad)	α unitless	β (cm/mrad)
18.000	0.0518314	-0.1123	14.2624
120.308	0.0204980	-0.1011	33.4936
235.615	0.0133838	-0.0912	49.6240
350.923	0.0099750	-0.1437	67.1929
466.231	0.0085285	-0.1040	74.4395
581.538	0.0067196	-0.0947	95.3158
696.846	0.0057833	-0.0998	105.1151
812.154	0.0051192	-0.1181	118.2021
927.462	0.0044896	-0.1088	136.6972
1042.769	0.0041803	-0.1070	142.4170
1158.077	0.0036778	-0.1269	159.4664
1273.385	0.0034156	-0.1348	169.8023
1388.692	0.0032107	-0.1344	179.9347
1504.000	0.0028241	-0.1322	204.0027
1619.308	0.0026936	-0.1210	209.0630
1734.615	0.0024274	-0.1140	223.0170
1849.923	0.0021895	-0.1304	238.1832
1965.231	0.0020891	-0.1275	242.9990
2080.539	0.0019487	-0.1458	267.0680
2195.846	0.0019406	-0.1453	268.7600
2311.154	0.0017939	-0.1540	289.2329
2426.462	0.0016386	-0.1566	314.7566
2541.769	0.0016162	-0.1446	319.1129
2657.077	0.0014301	-0.1355	347.5760
2772.385	0.0013817	-0.1132	347.5099
2887.692	0.0013361	-0.1150	352.5625
3003.000	0.0012789	-0.1162	359.4554
3118.308	0.0013097	-0.1334	350.8455
3233.615	0.0012020	-0.1556	374.3491
3348.923	0.0011817	-0.1832	378.3010
3464.231	0.0010868	-0.2094	409.8149

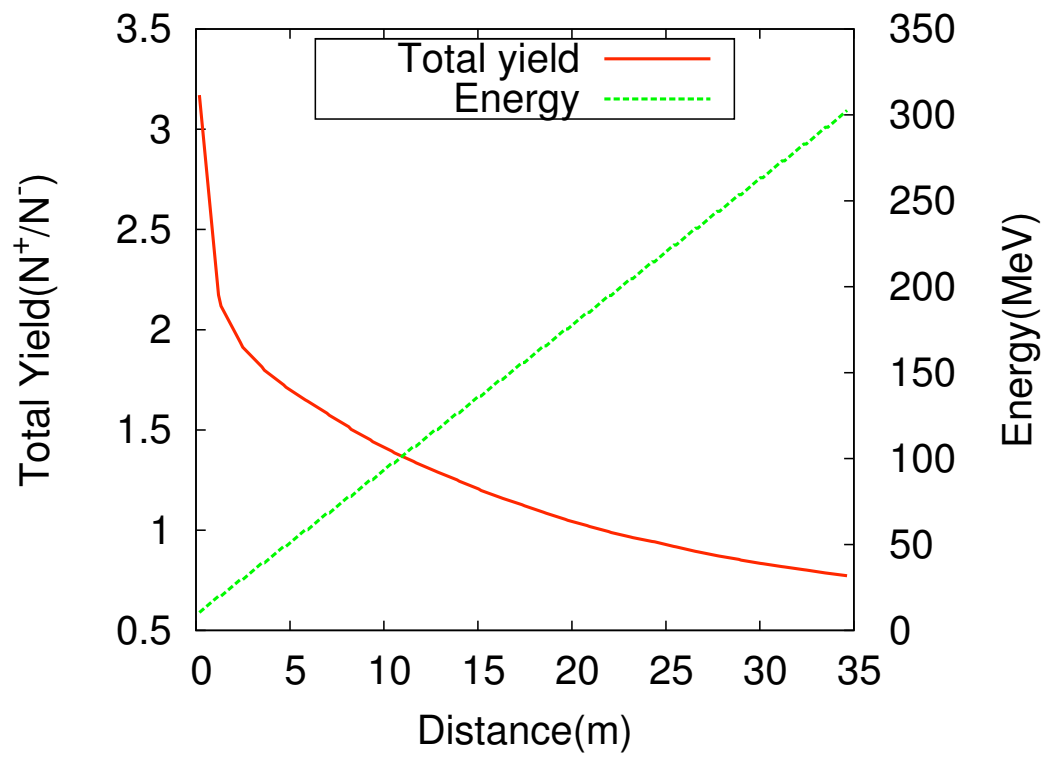


Figure 6.12: Total yield and energy of reference particle vs length in the 8-cell cavity accelerator system.

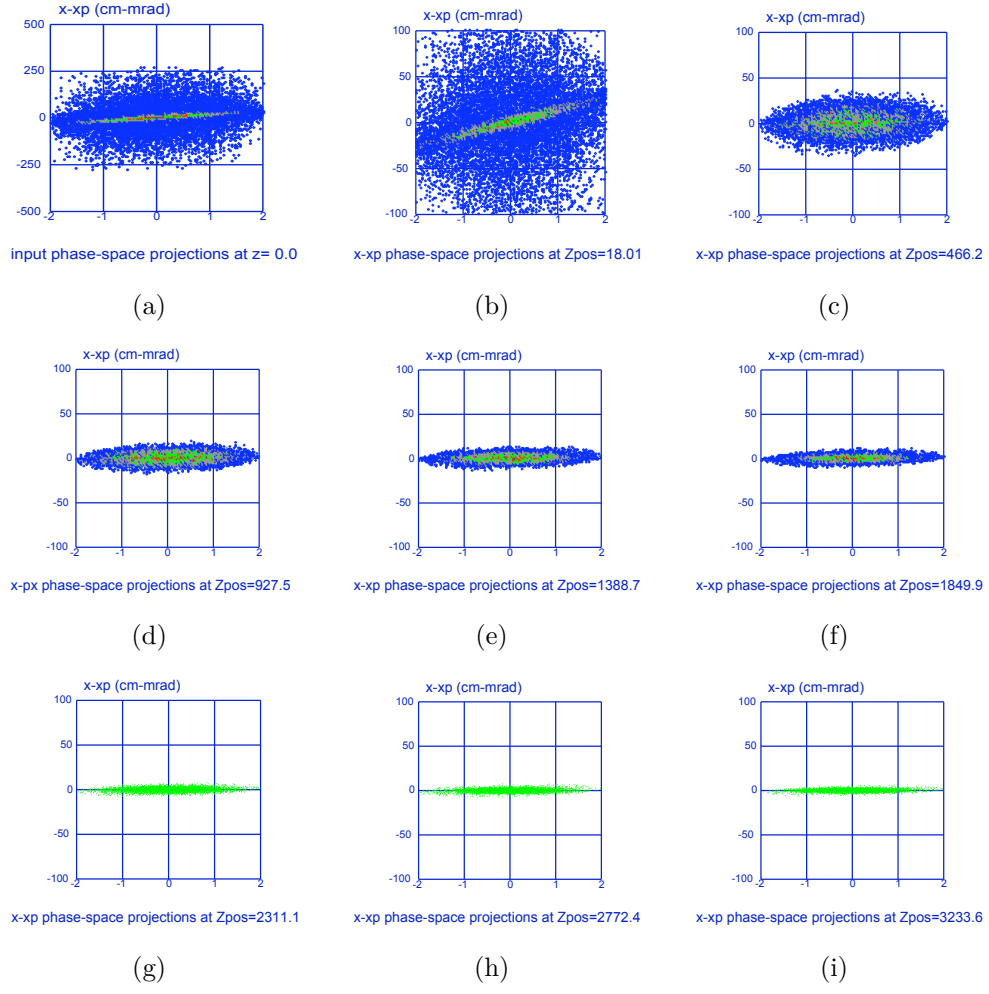
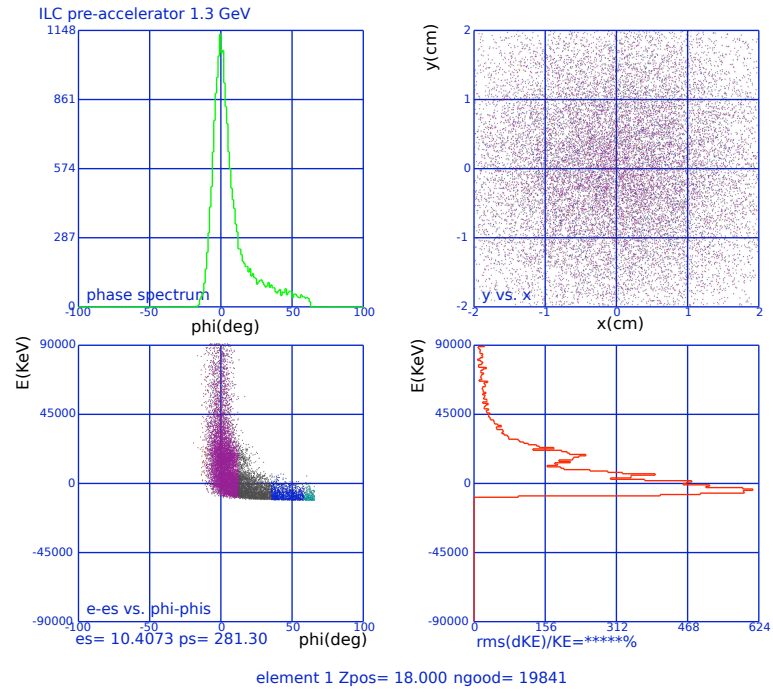
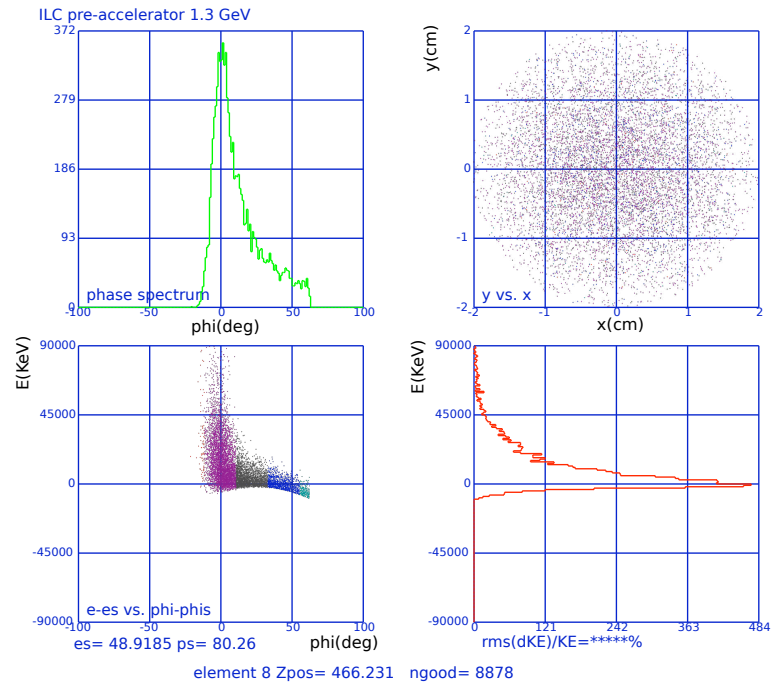


Figure 6.13: $x - xp$ in different points of the 8-cell cavity accelerator.

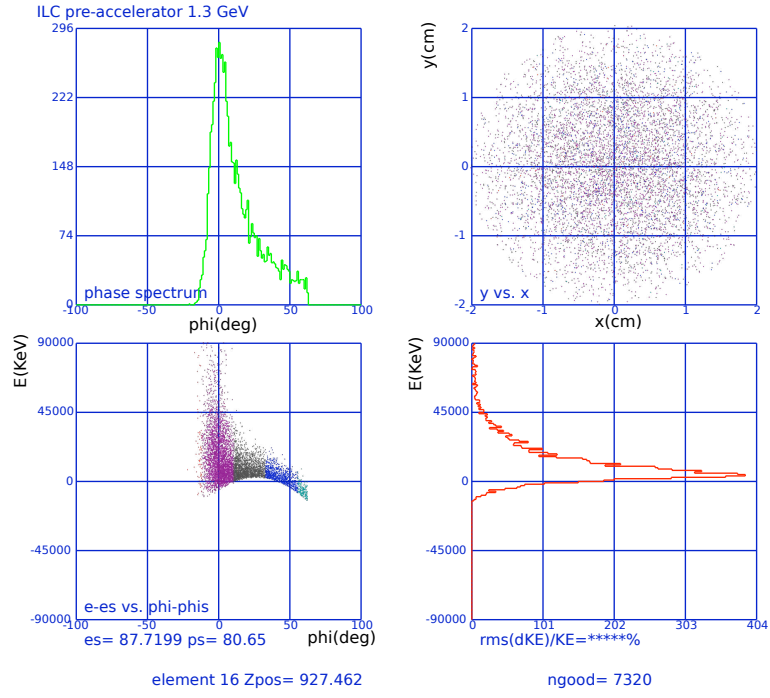


(a)

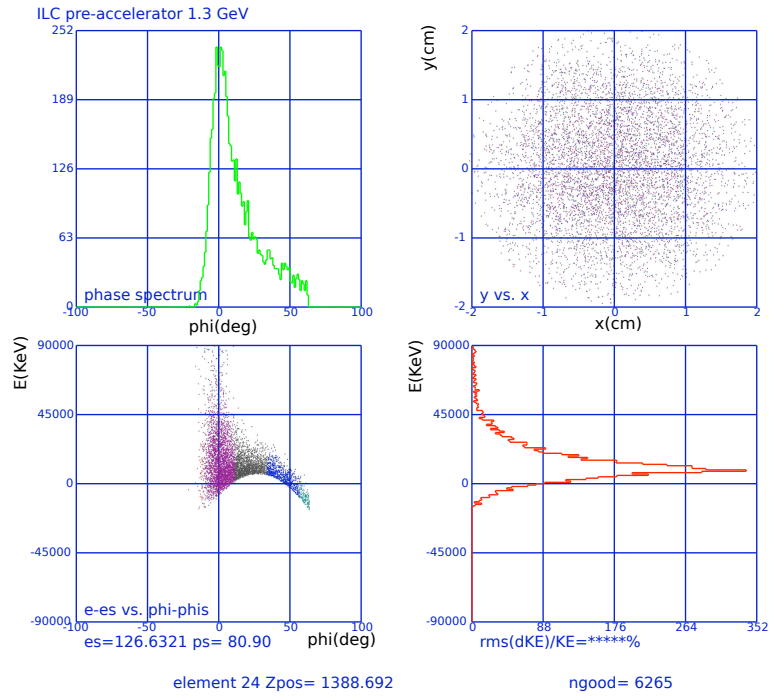


(b)

Figure 6.14

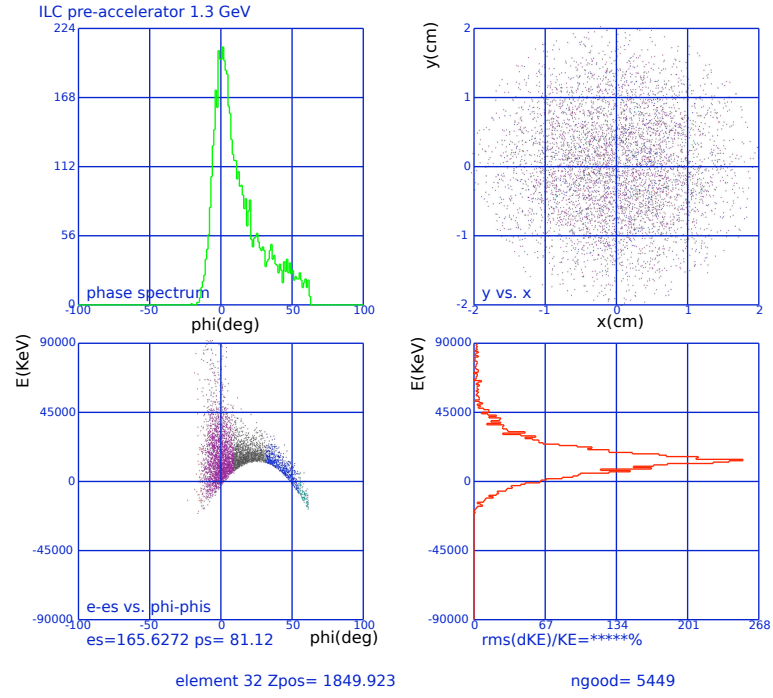


(c)

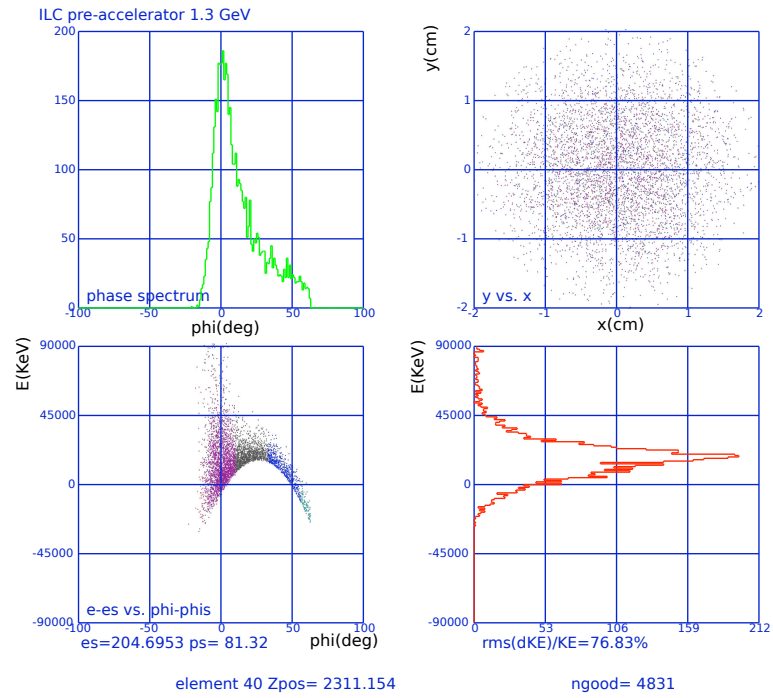


(d)

Figure 6.14



(e)



(f)

Figure 6.14

6.5 Matching system

The solenoid length is 34.6m. At the exit of the solenoid, the positron energy is $\sim 300\text{MeV}$. To transport positron beam into next accelerator system a quadrupoles matching system is needed. Suppose we have a periodical structure after the solenoid which is composed of a cavity and a triplet. Between the periodical structure and the solenoid we need a matching section. Here we use a triplet and a drift tube. Fig. 6.15 shows the match system position.

Figure 6.16 is the matched results by using TRACE3D. At the bottom of the figures, symbols 1 to 7 compose the matching section and symbols 8 to 31 compose three periodical structure. Emittance before the matching section and after three periodical section are plotted in the left and right side. The blue and red curves at the bottom is the x and y envelop. Words "30mm" means the maximum limits of the transverse dimension. In TRACE3D it uses total emittance which contains 100% of the particles.

The triplet magnetic in the periodical structure is 750gauss/cm . The magnetic field of the triplet and drift tube length in the matching section are adjusted and plotted in the middle of the figures, the magnetic fields from left to right are -885 , 853 and -843gauss/cm and the tube length is 1.588m

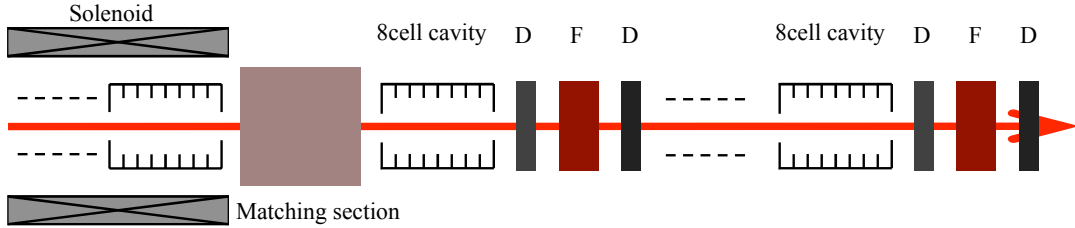


Figure 6.15: The matching system position.

The results from Parmela are shown in Fig. 6.17. Energy of positrons at beginning of the matching section is 300MeV and it is 340MeV after four periodical structure. For (b) we use rms emittance. The number of particles at beginning of the matching system is 3682, and 3402 at the exit of the four periodical structure.

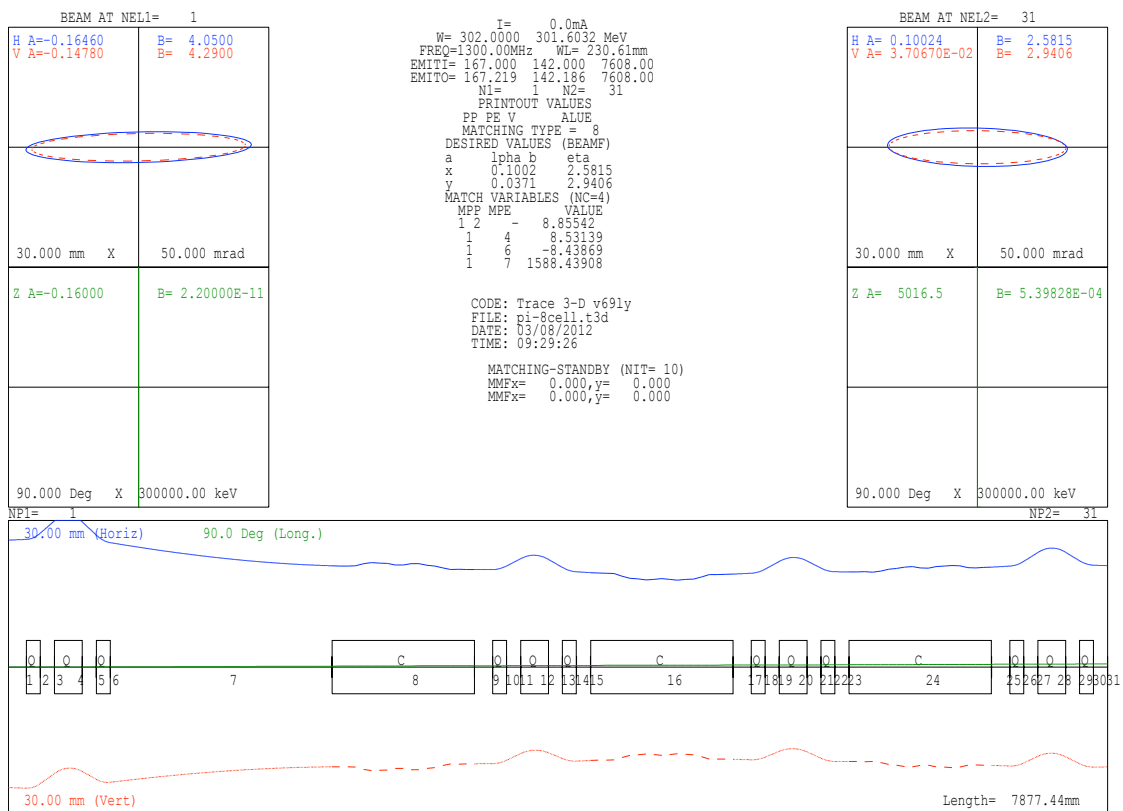
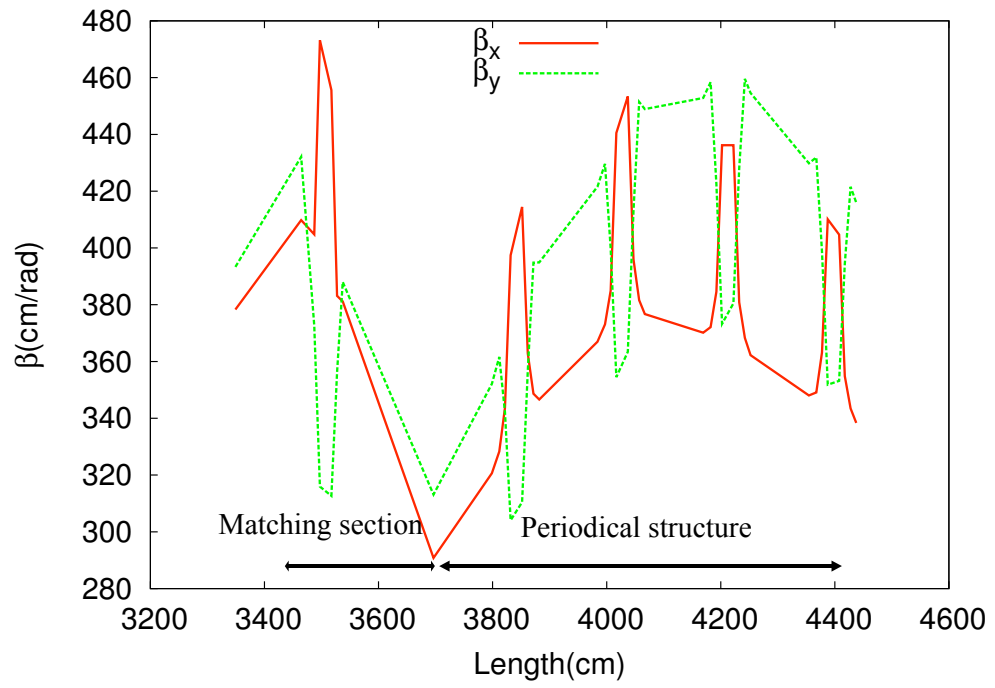
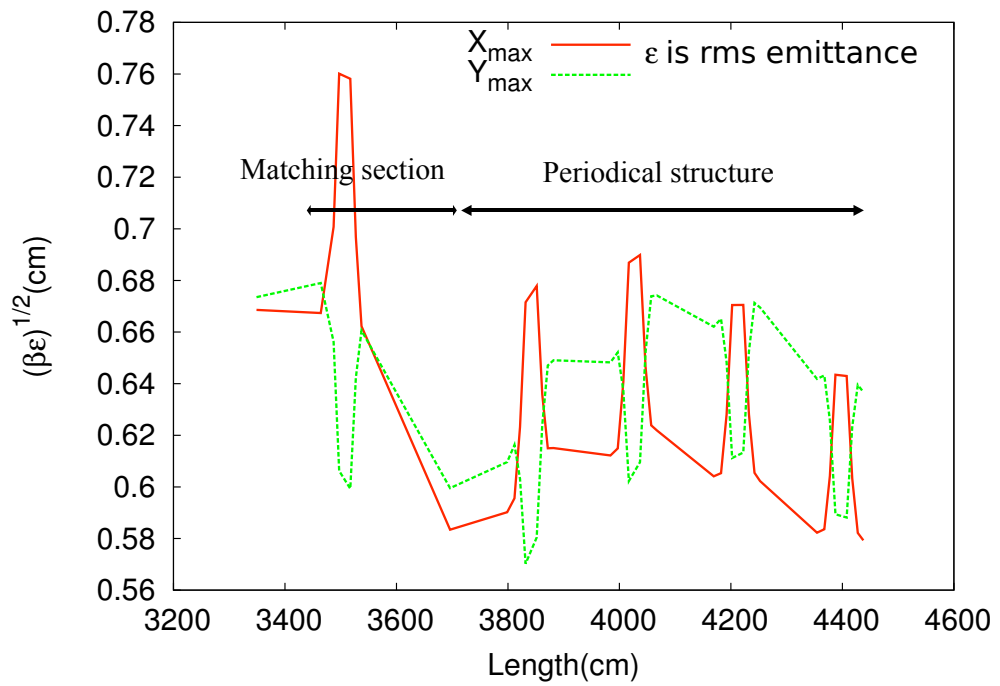


Figure 6.16: Matched quadrupoles and the periodical structure.



(a)



(b)

Figure 6.17

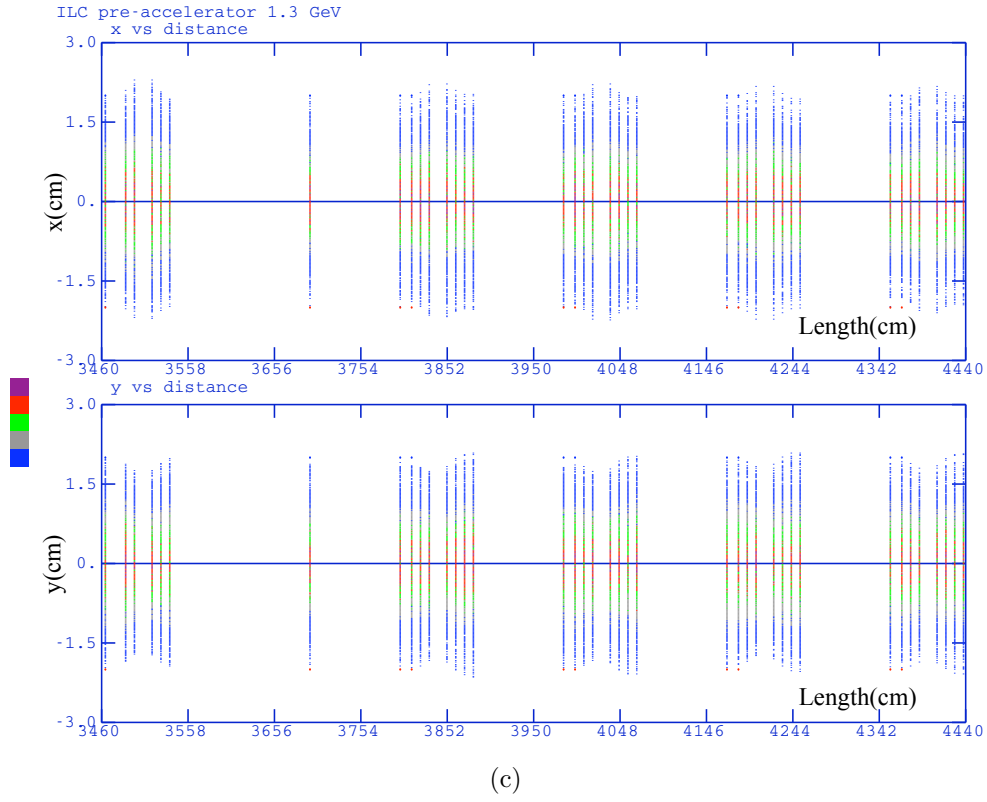


Figure 6.17: β function and envelopes in the matching section and 4 periodical structure. (a): β function. (b): envelopes in rms emittance. (c) envelopes of all particles.

Chapter 7

Conclusion

Next generation of e^+e^- colliders requires high intensity positron sources. According to ILC RDR the positron yield at the Interaction Point should be $1e^+/e^-$. It is a challenging problem. For conventional target scheme it is needed to increase the incident beam intensity and energy to increase also the positron beam intensity. But this will result in large amount of energy deposition in target which may melt down the target. One alternative solution is based on the channeling effect of GeV electron beams impinging on axially oriented crystals [2, 3]. In channeling conditions, the electrons emit a large number of photons which are more numerous than in an amorphous target of the same thickness. The photons then create a large amount of e^-e^+ pairs in pair converter.

In this thesis, we first recalled the main physical processes when an electron or a photon is incident on an amorphous target. With the resulting bremsstrahlung and pair production we have ionization processes leading to energy deposition. We recall also the crystal effects, mainly channeling of electrons along the main axes of a crystal, specifying also the channeling conditions. We put some emphasis on these processes as the positron source we are studying and proposing is based on a crystal-radiator and an amorphous converter. This kind of source has been studied experimentally by a French-Russian group at CERN (WA 103) and by Japanese colleagues at KEK, with some collaboration with French groups. These experiments have validated the simulations. In this report, we give the results of our simulations on this kind of source with an application to ILC.

A special device has been studied in our PhD work addressing the two main challenges for a positron source: a high yield, obtained with a high rate of photons produced in channeling conditions in a thin crystal and an optimization of the energy deposition and dissipation using a granular target instead of a compact

one at some distance from the crystal; the charged particles coming out from the crystal being deflected by a bending magnet to spare additional energy deposition in the amorphous converter. Such a solution is called hybrid source. It presents the advantage of relatively weak PEDD (Peak Energy Deposition Density)

Three kinds of matching devices put after the converter to optimize the positron phase space in order to fit with the accelerator acceptance, have been studied. The AMD (Adiabatic Matching Device), the QWT (Quarter wave Transformer) and the lithium lens. Their characteristics have been studied and compared.

The heating and cooling has been studied at different conditions and using the KEK scheme for ILC: this scheme modifies the incident beam time structure in order to get shorter pulses and enough time between the pulses to allow relaxing of the target heating. In these conditions, a solution has been studied for ILC. Simulations concerning the positron beam phase space, the energy deposition and the subsequent heating have been operated leading to a possible use of the hybrid source for ILC. This solution is answering the requirements of a high positron yield, a reasonable PEDD and a realistic cooling system.

The transport of the positron beam from the target to the Damping Ring is a delicate problem: we proposed an optical channel using a solenoid, after the matching system, and a quadrupole focusing system. The chosen accelerator just after the target is an L-Band structure allowing large enough geometrical acceptance.

The work being developed here led to a possible solution of an unpolarized positron source for ILC; the results can also be extended to CLIC, which presents a more easier situation.

Some of the studies presented here may also be of some usefulness for the BEPC positron source.

Appendix A

Simulation code

The simulation code used in this project is written in Geant4 and G4Fot Toolkit. It can simulate electromagnetic interaction between particle and medium, and channeling effect in crystals. It can simulate the transport of particle in electric and magnetic field. The code is hosted at Google code except G4Fot, the address is: <https://simpit.googlecode.com/svn/>

It is an flexible and high automatic program, only an input macro-script is need to address it. The code can do:

1. Construct geometry tree, and there is an built-in hexagonal geometry composed of sphere.
2. Simulate electromagnetic interaction between particle and medium, electric and magnetic field, polarization is considered. Simulate Channeling effect in Crystals.
3. Built-in energy deposition density sensitive detector.
4. Detector particle cross boundary of cubic and cylindric($Z = \pm L/2$ plane).
5. Simulate particle transport in electric and magnetic field. Built-in three Capture Devices: AMD, QWT and Lithium Lens.
6. Input particle format can be HEPEVT format[50], or built-in format, or random distribution.

According to HEPEVT format[51], the first line of each primary event should be an integer which represents the number of the following lines of primary particles. Each line in an event corresponds to a particle in the /HEPEVT/ common. Each line has

ISTHEP IDHEP JDAHEP(1) JDAHEP(2) PHEP(1) PHEP(2) PHEP(3) PHEP(5)
VHEP(1) VHEP(2)

ISTHEP(IHEP): Status code for entry IHEP, not used.

IDHEP(IHEP) : Particle identity, according to the PDG standard.

JDAHEP(1,IHEP) : Pointer to the position of the first daughter, not used.

JDAHEP(2,IHEP) : Pointer to the position of the last daughter, not used.

PHEP(1,IHEP) : Momentum in the x direction, in GeV/c .

PHEP(2,IHEP) : Momentum in the y direction, in GeV/c .

PHEP(3,IHEP) : Momentum in the z direction, in GeV/c .

PHEP(5,IHEP) : Mass, in GeV/c^2 . For space-like partons, it is allowed to use a negative mass, according to $PHEP(5,IHEP) = -\sqrt{-m^2}$.

VHEP(1,IHEP) : Production vertex x position, in mm.

VHEP(2,IHEP) : Production vertex y position, in mm.

For the Built-in input and output particle format, each line corresponds to a particle. Each line has

pdg eventID trackID x y px py pz Energy time Sx Sy Sz

pdg: Particle identity, according to the PDG standard.

eventID: Event identity, not used.

trackID: Track identity, not used.

x: Production vertex x position, in mm.

y: Production vertex y position, in mm.

px: Momentum in the x direction, in MeV/c .

py: Momentum in the y direction, in MeV/c .

pz: Momentum in the z direction, in MeV/c .

Energy: Energy, in GeV.

time: Energy, in picoseconds.

Sx: x polarization in stokes vector.

Sy: y polarization in stokes vector.

Sz: z polarization in stokes vector.

The following macro-script is an example. It construct a 10mm thick tungsten target, followed by a 1mm thick particle detector, then a 20cm thick AMD capture. The primary particles are shoot by built-in particle "gun". Particle energy is 100MeV. It calculate the deposited energy in tungsten target, count particles at the end of detector and AMD.

```
#####begin#####
/GP/Module/SetParameter / print.recursive.flag 1
/GP/Module/SetParameter / compact.flag 1

#target compact
/GP/Module/SetParameter / new.child target/
/GP/Module/SetParameter /target/ priority 0
/GP/Module/SetParameter /target/ compact.flag 1
/GP/Module/SetParameter /target/ center.z 0 mm
/GP/Module/SetParameter /target/ set.geometry

/GP/Module/SetParameter /target/geometry/ material G4_Galactic
/GP/Module/SetParameter /target/geometry/ solid.type G4Box
/GP/Module/SetParameter /target/geometry/ solid.width 20 mm
/GP/Module/SetParameter /target/geometry/ solid.height 20 mm
/GP/Module/SetParameter /target/geometry/ solid.length 10 mm

#target compact
#/control/execute ./mac/target_compact.mac
/GP/Module/SetParameter /target/ new.child compact/
/GP/Module/SetParameter /target/compact/ priority 0
/GP/Module/SetParameter /target/compact/ set.geometry
/GP/Module/SetParameter /target/compact/ set.event
/GP/Module/SetParameter /target/compact/ set.run

#/GP/Module/SetParameter /target/compact/geometry/ material G4_Galactic
/GP/Module/SetParameter /target/compact/geometry/ material G4_W
/GP/Module/SetParameter /target/compact/geometry/ solid.type G4Box
/GP/Module/SetParameter /target/compact/geometry/ solid.width 20 mm
/GP/Module/SetParameter /target/compact/geometry/ solid.height 20 mm
/GP/Module/SetParameter /target/compact/geometry/ solid.length 10 mm

/GP/Module/SetParameter /target/compact/geometry/ sd.active

/GP/Module/SetParameter /target/compact/geometry/ sd.type GPTargetSD
/GP/Module/SetParameter /target/compact/geometry/ sd.readout.cell.x 1 mm
/GP/Module/SetParameter /target/compact/geometry/ sd.readout.cell.y 1 mm
/GP/Module/SetParameter /target/compact/geometry/ sd.readout.cell.z 1 mm

##target count
#/control/execute ./mac/target_count.mac
```



```

/GP/Module/SetParameter / new.child target_count/
/GP/Module/SetParameter /target_count/ priority 10
/GP/Module/SetParameter /target_count/ set.geometry
/GP/Module/SetParameter /target_count/ set.event
/GP/Module/SetParameter /target_count/ set.run

/GP/Module/SetParameter /target_count/geometry/ material G4_Galactic
/GP/Module/SetParameter /target_count/geometry/ solid.type G4Tubs
/GP/Module/SetParameter /target_count/geometry/ solid.width 20 mm
/GP/Module/SetParameter /target_count/geometry/ solid.height 20 mm
/GP/Module/SetParameter /target_count/geometry/ solid.length 1 mm

/GP/Module/SetParameter /target_count/geometry/ sd.active
/GP/Module/SetParameter /target_count/geometry/ sd.type G4MultiFunctionalDetector
/GP/Module/SetParameter /target_count/geometry/ sd.scorer GPSurfaceParticleScorer
###target count

## capture
/GP/Module/SetParameter / new.child capture/
/GP/Module/SetParameter /capture/ priority 20
/GP/Module/SetParameter /capture/ set.geometry
/GP/Module/SetParameter /capture/ set.event
/GP/Module/SetParameter /capture/ set.run

/GP/Module/SetParameter /capture/geometry/ material G4_Galactic
/GP/Module/SetParameter /capture/geometry/ solid.type G4Tubs
/GP/Module/SetParameter /capture/geometry/ solid.width 40 mm
/GP/Module/SetParameter /capture/geometry/ solid.height 40 mm
/GP/Module/SetParameter /capture/geometry/ solid.length 20 cm

/GP/Module/SetParameter /capture/geometry/ limit.step.flag 1
/GP/Module/SetParameter /capture/geometry/ limit.step.max 2 mm

/GP/Module/SetParameter /capture/geometry/ set.field_manager capture
/GP/Module/SetParameter /capture/geometry/ field_manager.field.type 0

/GP/Module/SetParameter /capture/geometry/ sd.active
/GP/Module/SetParameter /capture/geometry/ sd.type G4MultiFunctionalDetector
/GP/Module/SetParameter /capture/geometry/ sd.scorer GPSurfaceParticleScorer
/GP/Module/SetParameter /capture/geometry/ sd.filter GPSurfaceParticleScorer e+
### capture

/GP/Module/Update
/GP/detector/update
/GP/detector/update

#primary
/GP/primary/SetParameter type particleGun
/GP/primary/SetParameter particleGun.fixed.flag 0
/GP/primary/SetParameter particleGun.particle.type e-
/GP/primary/SetParameter particleGun.energy.mean 100 MeV
/GP/primary/SetParameter particleGun.energy.rms -1.0 MeV
/GP/primary/SetParameter particleGun.position.z -5 mm
/GP/primary/SetParameter particleGun.position.tr.rms 1.0 mm
/GP/primary/SetParameter particleGun.angle.theta.mean 0.0
/GP/primary/SetParameter particleGun.angle.theta.rms 0.0
/GP/primary/SetParameter particleGun.time.rms 10 ps
/GP/primary/SetParameter particleGun.polarization 0 0 1

/run/setCut 1 mm
/run/beamOn 10000

```

```
exit
#####end#####
```


Acknowledgement

I would like to give my deepest thanks to all the people who have helped me during my thesis study.

Please let me first show my sincere gratitude to my supervisor in Institute of High Energy Physics, Professor Guoxi PEI, who deserves for this. He is an insightful advisor and a very kind and humor friend one can ever image to have. His wide knowledge, his logical way of thinking, his great ideas are always of great value for me. Professor Guoxi PEI introduced me into this field. In the past five years He give me lots of helps not only in the work but also in the life. Most gratitudes to him.

As a co-tutelle student between China and France, I am indebted thanks to my French advisor Professor Fabian ZOMER in Laboratoire de l'Accélérateur Linéaire. He is humor and kind supervisor. As my French supervisor he give me a lot of helps. Most respect and gratitudes to him.

The most gratitudes and highest respect belongs to Professor Robert CHEHAB who supervises me directly in France. He is such a responsible, nice and humor people that everyone I know like him. During the stay in France I work with him every day. Each steps, plans about the study and works is under his guidance and helps. I will give my most gratitudes to him. I will keep forever the memories we worked together in LAL, in CERN, and at Beijing, they are the biggest fortune in my life.

I wold also like to thank all the main contributors to my work: Oliver DADOUN, Professor Vladimir STRAKHOVENKO, Professor Xavier ARTRU and Professor Peter SIEVERS. Oliver is a funny and kind friend. He gave me lots of helps in my work and life and teach me lots of French. I would like to thank Professor Vladimir STRAKHOVENKO. My work is based on his simulation results concerning the crystal target. Same gratitudes should give to Professor Xavier ARTRU, I talked

with him at Lyon and Beijing, help me understand about crystal channeling effect. I will keep memories the tour we took in Beijing. The most gratitudes I also would like to give Professor Perter SIEVERS. He gave me a lot of help in granular target study, heating, cooling, etc.

I would also like to thank all the colleagues help me in my work. Yaliang ZHAO, Shilun PEI, Ouzheng XIAO. Thanks for their helps concerning microwave guide design, accelerator physics discussion. I would like to thank Miss Iryna CHAIKOVSKA, we worked in the same office at LAL. Thanks for her helps on my work.

I spent almost two years at LAL-Orsay. I would like thank the 2 director: Guy WORMSER and Achille STOCCHI they gave me a lot of helps about my work. In the two years in the Accelerator department of LAL. The leader Alessandro VAR-IOLA give me lots helps. Sincere gratitudes to him. These people deserve special respect and gratitudes: Professor Yunlong CHI, the vice leader of Accelerator Center in IHEP, Professor Fengli ZHAO, Leader of microwave group in Accelerator Center in IHEP, Professor Qiuqing WANG, Vice leader of IHEP, Professor Qing QIN, leader of Accelerator Center in IHEP. They gave me lots of help in my work in these years.

I would like to give best gratitudes to Professor Jie GAO who introduced me into IHEP and to accelerator physics. He helped a lot in my study and work.

During the stay in France, I got two fellowship from CAS-CSC and EIFFEL-France. I would like to thank CAS, Chinese Ambassador in France, The French Ministry of Foreign and European Affairs and EGIDE to help me finish the work in France.

As a Co-tutelle student between China and France which based on the framework of a collaboration between France and China(FCPPL). I would like to thank them to give me lots of helps.

I would also like to thank all the colleague in both laboratories in China and France. Xiaoping LI, Zusheng ZHOU. They gave me lots of helps in my projects. Professor Zhiqing ZHANG, who gave me lots of helps when I was in LAL. Thank all the Linac Operation group members in Accelerator Center in IHEP, they helped me a lot during my work at Linac. Thank all the colleagues: Kun LV, Xiangjian WANG, Xiang HE, Rong LIU, Li SHENG, Jingru ZHANG, Mi HOU, Jintong LIU, Jun ZHAI, Guozhong ZHOU, Yanfang ZHANG for their help in my work and life.

My thanks and appreciations also gave to my friends in France: Xifeng RUAN,

Limin MENG, Xiaomin YU, Jie YU, Wenbin QIAN, Dikai LI, Wenxin WANG, Xiaowei CHEN, Li YUAN and Liwen YAO, etc. Being a completely different country it is a hard thing. Because of you I can familiar with France life quickly. it is really my luck to spend my thesis period and life with you and I will keep my happy life in France with you. The same thanks and appreciations I would like to my friends in China: Fukun XU, Xiaobing WU, Jinfang CHEN, Xinpeng MA, Feng QIU, Yuwen AN, etc. Thanks all guys. I would like to thank my house-owner madame Annie CHABAUD. She is a very kind house-owner and give me a lot helps when I lived in her family. Thank you very much. I will keep memories the time she drove me out into forest, trip to Paris, etc.

Last but not least, I would like to thank all my family members, who are always there, supporting me no matter what I do and no matter how bad the situation is. I dedicate this dissertation to them.

Bibliography

- [1] S. A. (Stuart A.) Maloy, M. R. (Michael R.) James, R. W. (Robert W.) Rutherford, J. M. (James M.) Letbetter, R. J. (Robert J.) Romero, S. A. (Stanley A.) Bodenstein, Wayne A. Taylor, J. J. (James J.) Gallegos, R. M. (Robert M.) Gonzales, T. J. (Tobias J.) Romero, M. R. (Manual R.) Lopez, and Los Alamos National Laboratory. Stanford linear collider (slc) target analysis. Technical Report LA-UR-01-1913, Los Alamos National Laboratory, July 2001.
- [2] R Chehab, F Couchot, A R Nyaiesh, F Richard, and X Artru. Study of a positron source generated by photons from ultrarelativistic channeled particles. (LAL-RT-89-01):3 p, Mar 1989.
- [3] X. Artru, V.N. Baier, R. Chehab, and A. Jejcic. Positron source using channeling in a tungsten crystal. *Nuclear Instruments and Methods in Physics Research Section A: Accelerators, Spectrometers, Detectors and Associated Equipment*, 344(3):443 – 454, 1994.
- [4] X. Artru, V. N. Baier, T. V. Baier, R. Chehab, M. Chevallier, E. Hourani, A. Jejcic, V. Katkov, R. Kirsch, K. Maier, J. Major, J. Maillard, J-C. Poizat, J. Remillieux, G. Renou, J. Silva, and V. Strakhovenko. Axial channeling of relativistic electrons in crystals as a source for positron production. *Nuclear Instruments and Methods in Physics Research Section B: Beam Interactions with Materials and Atoms*, 119(1-2):246 – 252, 1996.
- [5] V.N. Baier, A.D. Bukin, T.V. Dimova, V.P. Druzhinin, M.S. Dubrovin, V.B. Golubev, S.I. Serednyakov, V.V. Shary, V.M. Strakhovenko, X. Artru, M. Chevallier, R. Kirsch, J-C. Poizat, J. Remillieux, R. Chehab, A. Jejcic, J. Silva, J. Major, A.P. Potylitsin, and I.E. Vnukov. Set-up optimization for an experimental test of a positron source using channeling. *Nuclear Instru-*

ments and Methods in Physics Research Section B: Beam Interactions with Materials and Atoms, 145(1-2):221 – 229, 1998.

- [6] R Chehab, R Cizeron, C Sylvia, V Baier, K Beloborodov, A Bukin, S Burdin, T Dimova, A Drozdetsky, V Druzhinin, M Dubrovin, V Golubev, S Serednyakov, V Shary, V Strakhovenko, X Artru, M Chevallier, D Dauvergne, R Kirsch, Ph Lautesse, J.-C Poizat, J Remillieux, A Jejcic, P Keppler, J Major, L Gatignon, G Bocek, V Kulibaba, N Maslov, A Bogdanov, A Potylitsin, and I Vnukov. Experimental study of a crystal positron source. *Physics Letters B*, 525(1-2):41 – 48, 2002.
- [7] X. Artru, V. Baier, K. Beloborodov, A. Bogdanov, A. Bukin, S. Burdin, R. Chehab, M. Chevallier, R. Cizeron, D. Dauvergne, T. Dimova, V. Druzhinin, M. Dubrovin, L. Gatignon, V. Golubev, A. Jejcic, P. Keppler, R. Kirsch, V. Kulibaba, Ph. Lautesse, J. Major, J.-C. Poizat, A. Potylitsin, J. Remillieux, S. Serednyakov, V. Shary, V. Strakhovenko, and C. Sylvia. Summary of experimental studies, at cern, on a positron source using crystal effects. *Nuclear Instruments and Methods in Physics Research Section B: Beam Interactions with Materials and Atoms*, 240(3):762 – 776, 2005.
- [8] T. Suwada, K. Furukawa, T. Kamitani, M. Satoh, T. Sugimura, K. Umemori, H. Okuno, R. Hamatsu, K. Yoshida, A.P. Potylitsyn, I.S. Tropin, and R. Chehab. Experimental study of positron production from a 2.55-mm-thick silicon crystal target using 8-gev electron beams with high-bunch charges. *Nuclear Instruments and Methods in Physics Research Section B: Beam Interactions with Materials and Atoms*, 252(1):142 – 147, 2006. Relativistic Channeling and Coherent Phenomena in Strong Fields.
- [9] T. Suwada, M. Satoh, K. Furukawa, T. Kamitani, T. Sugimura, K. Umemori, H. Okuno, Y. Endou, T. Haruna, R. Hamatsu, T. Sumiyoshi, K. Yoshida, A. P. Potylitsyn, I. S. Tropin, and R. Chehab. First application of a tungsten single-crystal positron source at the kek b factory. *Phys. Rev. ST Accel. Beams*, 10(7):073501, Jul 2007.
- [10] X. Artru, R. Chehab, M. Chevallier, and V. Strakhovenko. Advantages of axially aligned crystals used in positron production at future linear colliders. *Phys. Rev. ST Accel. Beams*, 6(9):091003, Sep 2003.
- [11] X. Artru, R. Chehab, M. Chevallier, V.M. Strakhovenko, A. Variola, and A. Vivoli. Polarized and unpolarized positron sources for electron-positron

- colliders. *Nuclear Instruments and Methods in Physics Research Section B: Beam Interactions with Materials and Atoms*, 266(17):3868 – 3875, 2008. Radiation from Relativistic Electrons in Periodic Structures - RREPS'07.
- [12] P Pugnât and P Sievers. A he-gas cooled, stationary granular target. *Journal of Physics G: Nuclear and Particle Physics*, 29(8):1797, 2003.
 - [13] V.N. Baier, V.M. Katkov, and V.M. Strakhovenko. Electromagnetic showers in crystals at gev energies. *Nuclear Instruments and Methods in Physics Research Section B: Beam Interactions with Materials and Atoms*, 103(2):147 – 155, 1995.
 - [14] O.Dadoun. A crystal photon radiator code as event generator for geant4. Technical report, LALOrsay, France, July 2010.
 - [15] B.B. Rossi. *High-energy particles*. Prentice-Hall physics series. Prentice-Hall, 1965.
 - [16] E. Fermi, J. Orear, and A.H. Rosenfeld. *Nuclear Physics: A Course Given by Enrico Fermi at the University of Chicago*. Midway reprints. University of Chicago Press, 1974.
 - [17] H. Bethe and W. Heitler. On the stopping of fast particles and on the creation of positive electrons. *Proceedings of the Royal Society of London. Series A, Containing Papers of a Mathematical and Physical Character*, 146(856):pp. 83–112, 1934.
 - [18] S.H. Kim and C.L. Doose. Development of a model superconducting helical undulator for the ilc positron source. In *Particle Accelerator Conference, 2007. PAC. IEEE*, pages 1136 –1138, june 2007.
 - [19] Brian M. Kincaid. A short period helical wiggler as an improved source of synchrotron radiation. *Journal of Applied Physics*, 48(7):2684 –2691, jul 1977.
 - [20] S. Araki. *Conceptual design of a polarised positron source based on laser compton scattering - a proposal submitted to snowmass 2005 -*. KEK Preprint. High Energy Accelerator Research Organization (KEK), 2005.
 - [21] Xiaoping Li. *Studies on the Inverse Compton Scattering based ILC Positron Source*. PhD thesis, Graduate University of the Chinese Academy of Sciences, 2009.

- [22] M.A. and Kumakhov. On the theory of electromagnetic radiation of charged particles in a crystal. *Physics Letters A*, 57(1):17 – 18, 1976.
- [23] X. Artru and M. Chevallier. Channeling radiation: Theory, semi-classical simulations. *Radiation Effects and Defects in Solids*, null(1):415–432, 1994.
- [24] International linear collider reference design report, 8 2007.
- [25] Hirotaka Shimizu, Sakae Araki, Yoshisato Funahashi, Yosuke Honda, Toshiyuki Okugi, Tsunehiko Omori, Nobuhiro Terunuma, Junji Urakawa, Masao Kuriki, Shuhei Miyoshi, Tohru Takahashi, Yasuaki Ushio, Tachishige Hirose, Kazuyuki Sakaue, Masakazu Washio, Pei Guoxi, and textscLi XiaoP-ing. Photon generation by laser-compton scattering using an optical resonant cavity at the kek-atf electron ring. *Journal of the Physical Society of Japan*, 78(7):074501, 2009.
- [26] A. P. Potylitsin. Production of polarized positrons through interaction of longitudinally polarized electrons with thin targets. *Nuclear Instruments and Methods in Physics Research Section A: Accelerators, Spectrometers, Detectors and Associated Equipment*, 398(2-3):395 – 398, 1997.
- [27] W. Heitler. *The quantum theory of radiation*. International series of monographs on physics. Dover Publications, 1954.
- [28] R Chehab. Unpolarized positron sources from amorphous and crystal targets for linear colliders. Technical Report LAL-RT-94-09, Paris 11. Lab. Accél. Linéaire, Orsay, Sep 1994.
- [29] A. Belkacem, N. Cue, and J.C. Kimball. Theory of crystal-assisted radiation and pair creation for imperfect alignment. *Physics Letters A*, 111(1–2):86 – 90, 1985.
- [30] E. Segrè. *Nuclei and particles: an introduction to nuclear and subnuclear physics*. W.A. Benjamin, 1964.
- [31] X Artru, R Kirsch, R Chehab, B Johnson, P Keppler, J V Major, Louis Rinolfi, and A Jejcic. Radiation-damage study of a monocrystalline tungsten positron converter. Jun 1998.
- [32] S. Agostinelli, J. Allison, K. Amako, J. Apostolakis, H. Araujo, P. Arce, M. Asai, D. Axen, S. Banerjee, G. Barrand, F. Behner, L. Bellagamba, J. Boudreau, L. Broglia, A. Brunengo, H. Burkhardt, S. Chauvie, J. Chuma,

- R. Chytracsek, G. Cooperman, G. Cosmo, P. Degtyarenko, A. Dell'Acqua, G. Depaola, D. Dietrich, R. Enami, A. Feliciello, C. Ferguson, H. Fesefeldt, G. Folger, F. Foppiano, A. Forti, S. Garelli, S. Giani, R. Giannitrapani, D. Gibin, J.J. Gómez Cadenas, I. González, G. Gracia Abril, G. Greeniaus, W. Greiner, V. Grichine, A. Grossheim, S. Guatelli, P. Gumplinger, R. Hamatsu, K. Hashimoto, H. Hasui, A. Heikkinen, A. Howard, V. Ivanchenko, A. Johnson, F.W. Jones, J. Kallenbach, N. Kanaya, M. Kawabata, Y. Kawabata, M. Kawaguti, S. Kelner, P. Kent, A. Kimura, T. Kodama, R. Kokoulin, M. Kossov, H. Kurashige, E. Lamanna, T. Lampén, V. Lara, V. Lefebvre, F. Lei, M. Liendl, W. Lockman, F. Longo, S. Magni, M. Maire, E. Medernach, K. Minamimoto, P. Mora de Freitas, Y. Morita, K. Murakami, M. Nagamatu, R. Nartallo, P. Nieminen, T. Nishimura, K. Ohtsubo, M. Okamura, S. O'Neale, Y. Oohata, K. Paech, J. Perl, A. Pfeiffer, M.G. Pia, F. Ranjard, A. Rybin, S. Sadilov, E. Di Salvo, G. Santin, T. Sasaki, N. Savvas, Y. Sawada, S. Scherer, S. Sei, V. Sirotenko, D. Smith, N. Starkov, H. Stoecker, J. Sulkimo, M. Takahata, S. Tanaka, E. Tcherniaev, E. Safai Tehrani, M. Tropeano, P. Truscott, H. Uno, L. Urban, P. Urban, M. Verderi, A. Walkden, W. Wander, H. Weber, J.P. Wellisch, T. Wenaus, D.C. Williams, D. Wright, T. Yamada, H. Yoshida, and D. Zschesche. Geant4—a simulation toolkit. *Nuclear Instruments and Methods in Physics Research Section A: Accelerators, Spectrometers, Detectors and Associated Equipment*, 506(3):250 – 303, 2003.
- [33] O. Dadoun, R. Chehab, B. Mouton, A. Variola, and A. Vivoli. EGS-GEANT4 ("Polarised version") benchmark. In *POSIPOL 2007 Workshop*, Orsay, France, 2007. Oral presentation - Transparents LAL 07-198.
- [34] V. N. Baier, V. M. Katkov, and V. M. Strakhovenko. Radiation yield of high-energy electrons in thick crystals. *physica status solidi (b)*, 133(2):583–592, 1986.
- [35] X. Artru, V. Baier, K. Beloborodov, G. Bocek, A. Bogdanov, A. Bozhenok, A. Bukin, S. Burdin, R. Chehab, M. Chevallier, R. Cizeron, D. Dauvergne, T. Dimova, A. Drozdetsky, V. Druzhinin, M. Dubrovin, L. Gatignon, V. Golubev, A. Jejcic, P. Keppler, R. Kirsch, V. Kulibaba, Ph. Lautesse, J. Major, N. Maslov, J.-C. Poizat, A. Potylitsin, J. Remillieux, S. Serebnyakov, V. Shary, V. Strakhovenko, C. Sylvia, and I. Vnukov. Experiment with a crystal-assisted positron source using 6 and 10 gev electrons. *Nuclear Instruments and Methods in Physics Research Section B: Beam Interactions*

- with Materials and Atoms*, 201(1):243 – 252, 2003. <ce:title>Radiation from Relativistic Electrons in Periodic Structures (RREPS '01)</ce:title>.
- [36] T. Suwada, S. Anami, R. Chehab, A. Enomoto, K. Furukawa, K. Kaki-hara, T. Kamitani, Y. Ogawa, S. Ohsawa, T. Oogoe, H. Okuno, T. Fujita, K. Umemori, K. Yoshida, R. Hamatsu, K. Sasahara, V. Ababiy, A. P. Potyl-itsyn, and I. E. Vnukov. Measurement of positron production efficiency from a tungsten monocrystalline target using 4- and 8-gev electrons. *Phys. Rev. E*, 67:016502, Jan 2003.
 - [37] Greg A L. Close-packed spheres, with umbrella light camera. http://en.wikipedia.org/wiki/File:Close-packed_spheres,_with_umbrella_light_%26_camera.jpg, Feb 2011.
 - [38] F. Bulos, H. DeStaebler, S. Ecklund, R. Helm, H. Hoag, H. Le Boutet, H. L. Lynch, R. Miller, and K. C. Moffeit. Design of a high yield position source. *Nuclear Science, IEEE Transactions on*, 32(5):1832 –1834, oct. 1985.
 - [39] T.P. Wangler. *RF linear accelerators*. Wiley series in beam physics and accelerator technology. Wiley, 1998.
 - [40] J. and Haissinski. Focusing devices for a positron beam at the linear acceler-ator of orsay. *Nuclear Instruments and Methods*, 51(2):181 – 196, 1967.
 - [41] B.F. Bayanov, J.N. Petrov, G.I. Sil’vestrov, J.A. Maclachlan, and G.L. Nicholls. A lithium lens for axially symmetric focusing of high energy particle beams. *Nuclear Instruments and Methods in Physics Research*, 190(1):9 – 14, 1981.
 - [42] T Omori. The 300 hz generation option of ilc positron source. Technical report, Université Claude Bernard, IPNL, Building DIRAC, La Doua Cam-pus, Lyon Université Claude Bernard, 4 rue Enrico Fermi 69622 Villeurbanne France, Jun 2009.
 - [43] W Kalbreier, W C Middelkoop, and P Sievers. Heating and cooling of external targets at the sps. oai:cds.cern.ch:1266237. Technical Report CERN-Lab-II-BT-Int-73-2, CERN, Geneva, Jun 1973.
 - [44] P Sievers. A stationary target for the cern-neutrino-factory. oai:cds.cern.ch:490195. Technical Report CERN-LHC-2001-001-MTA. CERN-NEUTRINO-FACTORY-NOTE-65. CERN-NUFACT-NOTE-65.

CERN-OPEN-2001-032, CERN, Geneva, Mar 2001. Revised version number 1 submitted on 2001-08-03 11:44:22.

- [45] P Sievers. Elastic stress waves in matter due to rapid heating by intense high-energy deposition. Technical report, CERN, Geneva, Jun 1974.
- [46] D.A. Edwards and J. Syphers. *An Introduction to the Physics of High Energy Accelerators*. Wiley Series in Beam Physics and Accelerator Technology. John Wiley & Sons, 2008.
- [47] L.M. Young. Parmela. Technical Report LA-UR-96-1835, Los Alamos, 1996.
- [48] S.Y. Lee. *Accelerator physics*. World Scientific, 2004.
- [49] R Chehab. Positron source. Technical report, Paris 11. Lab. Accél. Linéaire, Orsay, Jul 1992.
- [50] Stephen Mrenna. Pythia 6.4, physics and manual. <http://home.fnal.gov/~mrenna/lutp0613man2/lutp0613man2.html>, Mar 2006.
- [51] Stephen Mrenna. The hepevt standard. http://cepa.fnal.gov/psm/simulation/mcgen/lund/pythia_manual/pythia6.3/pythia6301/node39.html, Jul 2005.